UNIVERSITY OF CALIFORNIA, SAN DIEGO

INTEGRATED ATOMIC FORCE MICROSCOPY TECHNIQUES FOR ANALYSIS OF BIOMATERIALS: STUDY OF MEMBRANE PROTEINS

A dissertation submitted in partial satisfaction of the

requirements for the degree Doctor of Philosophy

in

Materials Science and Engineering

by

Laura S. Connelly

Committee in charge:

Professor Sungho Jin, Chair
Professor Ratnesh Lal, Co-Chair
Professor Vlado Lubarda
Professor Eduardo Macagno
Professor William Mobley

2014

The Dissertation of Laura S. Connelly is approved, and it is acceptable in quality and form for publication on microfilm and electronically:

_____

_____

_____

_____
Co-Chair

_____
Chair

University of California, San Diego

2014

DEDICATION

For the Fam,

Mom, Dad, John, & Tim

EPIGRAPH

Whenever you have an opportunity to learn something,
learn it.

Jane Connelly aka Grandma Jane

TABLE OF CONTENTS

LIST OF FIGURES AND TABLES

ACKNOWLEDGEMENTS

The work presented in this dissertation was a product of collaborations with many talented scientists. I would like to first thank my co-advisor Prof. Sungho Jin for bringing me to UCSD, welcoming me to his lab, and being an endless supply of innovative and inspiring ideas. I would also like to thank Prof. Eduardo Macagno for incorporating me into his research and spending the time to work with me in the lab for my first year and a half at UCSD. I thank him for some of the best research advice I received throughout my graduate work: *two hours in the library saves two months in the lab*. I cannot give enough thanks here to my advisor and committee chair Prof. Ratnesh Lal for supporting me throughout the majority of my dissertation research and providing the next best piece of research advice I received: *just do it*. Prof. Lal's grants, collaborations, and research team have been the foundation of this dissertation. I would like to thank the members of my committee Dr. William Mobley and Dr. Vlado Lubarda, for their feedback, support, and dedication.

I would like to acknowledge the members of the Lal Lab for Nano-bio-imaging and Devices for their collaboration, support, and making graduate school a more enjoyable place. I would like to especially thank Dr. Fernando Terna Arce for teaching me the techniques and tricks of AFM, editing my papers, and being a constant resource. I would like to thank Brian Meckes, Alan Gilman, Jeanie Kwok, for all the coffee and fro-yo, jokes, and science! I would like to thank Karla Khalifa and Christine Fransden for not only being first rate researchers partners but also amazing friends. I would like to

thank my collaborators at the NIH Dr. Hyunbum Jang and Dr. Ruth Nussinov who were not only significant contributors to Chapters 1-4 but also were invaluable in developing my scientific writing. I would sincerely like to thank Dr. Meni Wanunu and the members of the Nanoscale Biophysics Lab at Northeastern University for welcoming me to their lab for two months and helping me produce the work in Chapters 5 and 6. I especially want to thank Joseph Larkin, who spent many nights and weekends on the TEM to help me produce samples. I would like to thank my collaboration Dr. Christian Griesinger and his research group at the Max Planck Institute for Biophysical Chemistry, in Göttingen, Germany.

I would like to thank my close and dear friend Dr. Erna Van Niekerk for her friendship, sage advice, positivity, and the many miles run on the boardwalk. I would like to thank Dr. Allison Gillies and Caitlin Buckspan for being such strong friends, scientists, and inspirations. I would like to thank my Cornell materials science family, Jordan Raphel, Aitor Maiz, Daniel Ruebusch, and Tyson Moyer being there every hour, every day, every problem set and making me laugh the whole time. I would like to thank Dr. Uli Wiesner for supporting my undergraduate research that brought me to UCSD. I would like to thank Dr. Erik Herz for recognizing my potential and encouraging me to work with him on his research with Dr. Wiesner.

Most importantly I would like to thank my wonderful and supportive family. Thank you so much for always encouraging me to do my best and enjoy what I'm doing. Thank you, Mom and Dad, for giving me the confidence to pursue my education to this highest level and never thinking twice about it. Thank you to John and Tim for setting the bar so high!

I would also like to thank my fellowship providers, UCSD-Powell Fellowship, National Science Foundation Graduate Student Research Fellowship, National Defense Science and Engineering Graduate Fellowship, and the Achievement Rewards for Collegiate Scientists- San Diego Chapter (ARCS). I would also like to thank Doug Dawson and the Ellen Browning Scripps Foundation for funding my ARCS scholarship. This research is supported by NIH grants R01 DA025296-01, R01 AG028709-01, and R01 DA024871-10A1.

Chapter 1, in part, a reprint of the material as it appears in Physical Chemistry Chemical Physics, 2013, Jang H, Connelly L, Arce FT, Ramachandran S, Lal R, Kagan BL, Nussinov R. The dissertation author is a shared author with Dr. Hyunbum Jang of this paper.

Chapter 2, in full, is a reprint of the material as it appears in the Journal of Physical Chemistry B, 2012, Connelly L, Jang H, Arce FT, Capone R, Kotler SA, Ramachandran S, Kagan BL, Nussinov R, Lal R. The dissertation author was the primary investigator and author of this paper.

Chapter 3, in full, is a reprint of the material as it appears in Biochemistry, 2012, Connelly L, Jang H, Arce FT, Ramachandran S, Kagan BL, Nussinov R, Lal R. The dissertation author was the primary investigator and author of this paper.

Chapter 4, Section 4.4, which in part, is a reprint of the material as it appears in Physical Chemistry Chemical Physics, 2013, Jang H, Connelly L, Arce FT, Ramachandran S, Lal R, Kagan BL, Nussinov R. The dissertation author was a shared investigator and author with Dr. Hyunbum Jang of this paper.

Chapter 5, in part, is currently being prepared for submission for publication of the material, Connelly L, Meckes B, Larkin J, Gilman A, Arce FT, Wanunu M, Lal R. The dissertation author was the primary investigator and author of this material.

Chapter 6, in part, is currently being prepared for submission for publication of the material, Connelly, L., Meckes, B., Larkin, J., Gilman, A., Wanunu, M.,, Lal, R. No authors have competing interests.

VITA

2008	Bachelor of Science, Materials Science and Engineering Cornell University
2009	Master of Science, Materials Science and Engineering University of California, San Diego
2008-2014	Graduate Student Researcher, Materials Science and Engineering Graduate Program
2014	Doctor of Philosophy, Materials Science and Engineering University of California, San Diego

Journal Articles

H. Jang, **L. Connelly**, F. Teran Arce, S. Ramachandran, R. Lal, B. Kagan, R. Nussinov, "Alzheimer's disease: Which type of amyloid-preventing agents to employ?" *Phys Chem. Chem. Phys.* **15**, 8868-8877 (2013).

H. Jang, **L. Connelly**, F. Teran Arce, S. Ramachandran, B. Kagan, R. Lal, R. Nussinov, "Mechanisms for the Insertion of Toxic, Fibril-like **β-**Amyloid Oligomers into the Membrane," *J. Chem. Theory Comp.,* **9**, [1] 822-833 (2013).

L. Connelly, H. Jang, F. Teran Arce, S. Ramachandran, B. L. Kagan, R. Nussinov, R. Lal, "Effects of Point Substitutions on the Structure of Toxic Alzheimer's**β-**Amyloid Channels: Atomic Force Microscopy and Molecular Dynamics Simulations," J. *Biochem*., **51**, [14] 3031-3038 (2012).

R. Capone, H. Jang, S. Kotler, **L. Connelly**, F. Teran Arce, S. Ramachandran, B. Kagan, R. Nussinov, R. Lal, "All-D-Enantiomer of β-Amyloid Peptide Forms Ion Channels in Lipid Bilayers," J. *Chem. Theory Comput.*, **8,** [3] 1143-1152 (2012).

L. Connelly, H. Jang, F. Teran Arce, R. Capone, S. Kotler, B. Kagan, R. Nussinov, R. Lal, "Atomic Force Microscopy and MD Simulations Reveal Pore-Like Structures of All-D-Enantiomer of Alzheimer's **β-**Amyloid Peptide: Relevance to the Ion Channel Mechanism of AD Pathology," *J. Phys. Chem. B* **11** [5] 1728-1735 (2012).

C. J. Frandsen, K. S. Brammer, K. Noh, **L. S. Connelly**, S. Oh, L. Chen, S. Jin, "Zirconium Oxide Nanotube Surface Prompts Increased Osteoblast Functionality and Mineralization," *Mat. Sci. Eng.C* **31,** [8] 1716-1722 (2011).

K. S. Brammer, H. Kim, K. Noh, M. Loya, C. J. Frandsen, L. Chen, **L. S. Connelly**, S. Jin, "Highly Bioactive 8 nm Hydrothermal TiO_2 Nanotubes Elicit Enhanced Bone Cell Response," *Adv. Eng. Mat.* **13** [3] B88-B94 (2011).

K. S. Brammer, C. Choi, S. Oh, C. J. Cobb, **L. S. Connelly**, M. Loya, S. D. Kong, S. Jin, "Antibiofouling, Sustained Antibiotic Release by Si Nanowire Templates," *Nano Lett.* **9** [10] 3570-3574 (2009).

E. Herz, T. Marchincin, **L. Connelly**, D. Bonner, A. Burns, S. Switalski, U. Wiesner, "Relative Quantum Yield Measurements of Coumarin Encapsulated in Core-Shell Silica Nanoparticles," *J. Fluorescence* **20** 67-72 (2010).

Selected Abstracts

L. Connelly, R. Capone, H. Jang, S. Kotler, F. Teran Arce, S. Ramachandran, B. Kagan, R. Nussinov, R. Lal, "Amyloid Beta Ion Channels Mediate Alzheimer's Toxicity and Site-Specific Substitution in the Pore Region Controls its Activity: Unraveling Therapeutic Targets by Atomic Force Microscopy, Electrophysiology, MD Simulation, and Protein Engineering," **Oral Platform**, Society for Neuroscience, New Orleans, LA, October 2012.

L. S. Connelly, F. Teran Arce, H. Jang, R. Capone, S. Kotler, B. Kagan, R. Nussinov, R. Lal, "Alzheimer's β-Amyloid All-D-Enantiomers and Native All-L-Enantiomers Exhibit Similar Pore Structures in Lipid Bilayers: Atomic Force Microscopy," Poster Presentation, 56th Annual Biophysical Society Meeting, San Diego, Ca, February 2012.

H. Jang, R. Capone, S. A. Kotler, F. Teran Arce, **L. Connelly**, S. Ramachandran, B. L. Kagan, R. Lal, R. Nussinov, "Modeling Alzheimer's Ion Channel Structures in Lipid Bilayers Formed by D- and L-Enantiomers of Beta-Amyloid (1-42) Peptide," Poster Presentation, 56th Annual Biophysical Society Meeting, San Diego, Ca, February 2012.

R. Capone, H. Jang, S. A. Kotler, **L. Connelly**, M. Williams, S. Ramachandran, R. L. Kagan, R. Nussinov, R. Lal, "All D-Amino Acids Amyloid β Forms Ion Channels in Lipid Bilayers and is Toxic to Cells," 56th Annual Biophysical Society Meeting, San Diego, Ca, February 2012.

L.Connelly, F. Teran Arce, H. Jang, R. Capone, S. Kotler, S. Ramachandran, B. Kagan, R. Nussinov, R. Lal, "Pore Structures in Lipid Bilayers Formed by an All-D-Enantiomer of Alzheimer's β-Amyloid Are Similar to Those Formed by the Native L-Peptide," Poster Presentation, MRS Fall Meeting & Expo, Boston, Ma, November 2011.

L. S. Connelly, K. Brammer, R. Lal, S. Jin, "Cellular Uptake, Cytotoxicity, and Morphological Changes of Mesenchymal Stem Cells by Magnetic Nanorods,"

Poster Presentation, 2011 UCSD Student Research Expo, La Jolla, Ca, April 2011.

L. S. Connelly, R. Capone, S. A. Kotler, R. Nussinov, R. Lal, "Probing Structural Features of Alzheimer's β-Amyloid Ion Channels in Membranes Using Aβ Mutants," *Poster Presentation*, ARCS 2011 Scientist of the Year Dinner, La Jolla, Ca, March 2011.

R. Capone, S. A. Kotler, H. Jang, **L. S. Connelly**, R. Nussinov, R. Lal, "Probing Structural Features of Alzheimer's β-Amyloid Ion Channels in Membranes Using Aβ Mutants," *Oral Platform*, 55th Annual Biophysical Society Meeting, Baltimore MD, March 2011.

ABSTRACT OF THE DISSERTATION

INTEGRATED ATOMIC FORCE MICROSCOPY TECHNIQUES FOR ANALYSIS OF BIOMATERIALS: STUDY OF MEMBRANE PROTEINS

by

Laura S. Connelly

Doctor of Philosophy in Materials Science and Engineering

University of California, San Diego, 2014

Professor Sungho Jin, Chair

Professor Ratnesh Lal, Co-Chair

Atomic Force Microscopy (AFM) is the prominent techniques for structural studies of biological materials in physiological relevant fluidic environments. AFM has been used to resolve the three-dimensional (3D) surface structure of cells, membranes,

and proteins structures. Ion channels, formed by membrane proteins, are the key structures that control the activity of all living systems. This dissertation focuses on the structural evaluation of membrane proteins through atomic force microscopy. In Part I, AFM is utilized to study one of the most prominent medical issues facing our society, Alzheimer's Disease (AD). AD is a misfolded protein disease characterized by the accumulation of β-amyloid (Aβ) peptide as senile plaques, progressive neurodegeneration, and memory loss. Recent evidence suggests that AD pathology is linked to the destabilization of cellular ionic homeostasis mediated by toxic channel structures composed of Aβ peptides. Selectively engineered sequences of Aβ were examined by AFM to elucidate the substructures and thus activity Aβ channels. Key residues were evaluated with the intent better understand the exact nature by which these pores conduct electrical and molecular signals, which could aid in identifying potential therapeutic targets for the prevention/treatment of AD. Additionally, AFM was used to analyze brain derived Aβ and newly developed pharmacological agents to study membranes and Aβ. Part II, presents a novel technology that incorporates electrophysiology into the AFM interface, enabling simultaneous imaging and complementary conductance measurements. The activity of ion channels is studied by various techniques, including patch clamp, free standing lipid bilayers, droplet interface bilayers, and supported lipid bilayers. However, direct correlation with channel structures has remained a challenge. The integrated atomic force microscopy system presented offers a solution to this challenge. The functionality of the system is demonstrated with an Sf9 membrane plaque containing Cx26.

CHAPTER 1

Introduction

1.1 Atomic Force Microscopy

1.1.1 History and Basic Principles

Atomic Force Microscopy (AFM) was first introduced by Binnig et. al. in 1986 as a development of the scanning tunneling microscope (STM), a previously presented technique with Rohrer.[1] Both the AFM and STM are forms of scanning probe microscopy (SPM). SPM produces a property map of a material's surface and is based on a physical interaction between a probe, or tip, and the surface. In AFM, a very sharp (usually nanometer sized) tip is mounted on a cantilever of known stiffness and raster scanned across the surface of the material. As the topography of the sample changes, the scanning cantilever is proportionally deflected due to the interaction of the tip with the atoms at the surface of the material, creating a relief map. This original principle of operation, as presented by Binnig et. al.[1] is displayed in Fig. 1.1 A. The deflection of the cantilever is monitored with atomic resolution by aiming a laser onto the back of the

cantilever and reflecting it first onto a mirror and then to a photodiode. The sample prep sits on a piezoelectric scanner, which moves the sample in relation to the tip, creating the x-y scanning action. The deflection information from the photodiode is processed and translated through a feedback loop to the scanner. The scanner moves the sample in the z-direction to maintain a constant deflection. A complete schematic of AFM operation is shown in Fig.1.1B[2]. AFM imaging may be done either in air, liquid, or vacuum.

1.1.2 Contributing Forces

The deflection of the cantilever by the surface is determined by the sum of the attractive and repulsive forces between the two. The dominating attractive forces are Van der Waals and, in air, capillary forces from a hydration meniscus. The dominating repulsive force originates from overlapping of electron orbitals of the tip and surface.[3] When imaging is done in liquid, the meniscus force is eliminated, however forces such as electrostatic interactions, hydration force, solvation forces, and adhesion forces persist.[4] The greater the cantilever deflection, the greater the interaction force between the tip and the sample.[5] When this interaction force is minimized, images of the surface may be obtained with minimal damage to its structure. By examining an extension/retraction force curve for the cantilever at a single position, a deflection threshold, or setpoint, may be minimized thus minimizing the interaction force. A representative force curve is shown in Fig. 1.2.[6] As the cantilever approaches the surface it is pulled to the surface by the meniscus force creating a slight downward deflection of the cantilever. The

cantilever continues to approach the surface, passes the zero deflection point, and is deflected until the threshold is reached. The corresponding laser deflection on the photodiode is shown for each point. The cantilever is then retracted along the same path in the z direction. The deflection follows the same linear path until the zero deflection point. Upon retraction the deflection dips lower than the zero point because the tip sticks to the surface. The point at which the tip snaps from the surface and deflection returns to zero is indicative of the adhesion force. Force from this curve is calculated from Hook's law, F=-kx, where F is applied force, k is the spring constant of the cantilever, and x is the deflection.[1], [2]

1.1.3 Imaging Modes

The two main modes of operation for AFM are contact mode and tapping mode. In contact mode, the tip maintains constant interaction with the sample surface and the feedback loop maintains a constant deflection. In tapping mode, the cantilever is oscillated at a resonant frequency causing the tip to only tap the surface. The tapping minimizes the total amount of physical interaction between the tip and sample surface and is therefore ideal for softer samples, such as bilayers or cells. In tapping mode a constant amplitude is maintained and the feedback adjusts for the amount of damping throughout the scanned area.[5]

Force volume (FV) mode is an additional imaging option in AFM. In this mode the sample surface is still raster scanned, however only for a set number of data points.

The cantilever measures a force curve for each data point in the scan in a force map of the sample's surface. To produce a force curve for each data point significantly increases the total scan time of an image and, therefore, force maps exhibit much lower resolution. Physical properties such as deflection, stiffness, elastic modulus, and adhesion force can be extracted from a force curve. As a result FV mode is used characterize the physical properties of a sample by creating a spatial map of the desired property.

1.1.4 Advantages

AFM, as an imaging technique, has many advantages over optical microscopy techniques. The greatest advantage of AFM is its special resolution, which is based on a physical interaction and is not limited by the wavelength of light. It is because of this principle of operation that molecular[7] and even atomic resolution[8] has been achieved (Fig. 1.3). Many other, non-optical, imaging techniques such as electron microscopy, x-ray imaging, and magnetic resonance imaging require fixing, coating, or other treatments that can alter the structure of composition of a sample. AFM may be used for the imaging of specimens without any of these preparations and, therefore, is ideal for the imaging of biological speciments.[5], [9], [10] AFM operation, as previously mentioned, can be performed in either air or fluid. The open interface of the system also allows for customizable imaging environments such as controlled temperature, humidity, and pressure. Beyond surface topography imaging, the cantilever and tip can be utilized as a nanotool to manipulate a surface or individual molecules.[2], [5] By applying controlled

forces to a sample area, layers of the surface can be sequentially stripped away or force dissected (Fig. 1.4A).[11]–[13] AFM tips can be functionalized and used as a sensor[14] (Fig. 1.4 B), tensile test puller[2], [15], [16] (Fig. 1.4 C), or nanopen[17] (Fig. 1.4 D). Novel tips can be fabricated and incorporated into the AFM interface for innovative measurements or sample modifications. For example, conducting tips can inject or measure current[18] and nanopipette tips can inject analytes[19] (Fig. 1.4 E, F). The open interface of AFM provides an accepting environment for incorporation of complementary techniques and measurements such as ionic conductance, TIRF, fluorescence, microfluidics or other innovative techniques.[5]

Despite the many advantages of AFM, like any technology there exist challenges. The most outstanding challenge of AFM is the operation time needed to obtain a high-resolution image. Additionally, samples imaged with AFM are limited in resolution by the quality and sharpness of the tip. Broken, dulled, or atypical tips may result in images with extraneous features. The taper of the tip further limits the accuracy of images obtained of features with high aspect ratios. The use of AFM, especially when obtaining high-resolution images of soft, sticky, or delicate samples like biological structures, often requires a high level of skill and experience with the system. While AFM gives a user extensive control, the knowledge and ability to manipulate the settings to obtain high quality images and data is considered an art.

1.1.5 Resolution

While the resolution of AFM is not limited by the wavelength of light, the resolution limitations of AFM arise from several other sources. Instrumental resolution includes the spatial resolution capabilities of the piezo scanner, laser, and photo diode. The sensitivity of the piezoelectric scanner in the AFM system are capable of lateral resolutions of 0.1 nm and vertical resolutions 0.01nm.[5] Target resolution is a product of the tip properties, imaging environment, and the specimen itself. Generally, the smaller and sharper the tip is, the better the spatial resolution. Hard crystalline specimens have been imaged to the highest resolution at the atomic level (Fig. 1.3 B).[8] AFM has been used to resolve features <1 nm apart in hard noncrystalline materials.[20] Biological specimens have the lowest resolution due to their soft and dynamic nature. However, sophisticated sample preparations have enabled small biological structures, such as ion channels, to be resolved.[21], [22] Individual head groups of lipid membranes have been resolved when prepared as a Langmuir-Blodgett film (Fig. 1.3 A).[7] The sample preparation is crucial to the quality of images of biological specimens. Temperature, fluid environment, and mobility of the sample are all environmental factors that may further limit the resolution of AFM. Temporal resolution of AFM imaging is sample material dependent.[23] The lateral diffusion constant of the material is negligible for solid-state samples but influential in biological specimens. Cells or membranes that are anchored and packed at a high density limit their lateral diffusion and thus improve the temporal

resolution of the image. Other factors affecting temporal resolution include the speed of the feedback electronics and scan size.[5], [7], [23] Fast scanning options have been a major technical objective in AFM developments, with the greatest improvements coming from the fabrication of smaller cantilevers with higher resonant frequencies.[9] Manufacturers of new commercial AFM models claim atomic point defect resolutions at speeds of seconds compared to minutes (Bruker Corporation and Asylum Research).

1.2 Alzheimer's Disease

1.2.1 History and Societal Impact

Alzheimer's Disease (AD) is a progressive neurodegenerative disease characterized by a loss of memory, thinking, and brain functions. AD is one of the largest health related problem in our society today. It is the 6th leading cause of death in the US, taking the lives of 5.4 million Americans every year (www.alz.org), latest facts and figures 2012).[24] It is believed that as other medical advancements have led to an increase in the average lifetime, age related diseases such as AD are becoming increasingly more prominent. Therefore, this stark numbers are only expected to increase in the generations to come. Despite widespread research on AD the pathogenic mechanism of the disease remains unclear. AD is the only cause of death in the list of 10

ten without a way to prevent, cure or slow progression. The existing therapeutics for AD only temporarily ameliorates the symptoms but do not address the pathology. [24]

Alois Alzheimer in 1906 was the first to show that deceased patients, that had symptoms characteristic of what is now known as AD, showed a build up of protein plaques in their brain tissue.[25], [26] These protein plaques exist as extracellular deposits and intracellular bundles of neurofibrillary tangles (NFTs). The NFTs are mainly composed of the tau protein. Patients showing NFTs without the extracellular deposits have been found to exhibit different symptoms than those expressing the deposits.[25] Therefore, these extracellular deposits, mainly composed of amyloid-β (Aβ) protein, are considered the main pathological feature of AD.

Proteins are macromolecules synthesized by living systems to carry out the necessary functions to maintain life. Proteins are composed of a sequence of amino acids which, when linked together, determine their structure and subsequent function. Following the synthesis of an amino acid sequence, the protein undergoes a series of folding events before reaching its final conformation. This series may include interactions and corrections by enzymes and other species. If problems arise in this processing the result may be a misfolded protein.[27], [28] Many misfolded proteins are associated with conformational disorders (Fig1.5).[29] Amyloids, are a category of misfolded proteins that are found in aggregate deposits, exhibit a cross β-sheet structure, are resistant to proteolytic degradation, and bind congo red.[25], [30], [31] In addition to AD, amyloid plaques are a pathologic hallmark in victims of Parkinson's disease, Huntington's, Amyotrophic lateral sclerosis (ALS, or Lou Gehrig's disease), and Type II diabetes.[29],

[30] Progress in AD research, or on any of these disorders, will likely benefit the entire field of amyloidoses.

1.2.2 β-Amyloid Toxicity Hypothesis

Understanding the evolution and function of Aβ is believed to be key to preventing and treating AD. The amyloid cascade hypothesis (ACH) is the dominating postulate for the pathological progression of AD.[29], [32], [33] The hypothesis states there is an overall connection between the production of Aβ, neuronal dysfunction and death, and dementia. As displayed in Fig. 1.6 the production of Aβ leads to a hierarchy of aggregated states from monomers to fibrils. An increase in quantity of Aβ leads to neuronal stress, resulting in a disruption to cellular homeostasis and, eventually, neuronal degeneration.[21], [29], [32]–[36]

A central tenant of the ACH is that Aβ toxicity is linked to the disruption of the cell's homeostasis, mainly by a gain of Ca^{2+}, which triggers Aβ-induced neuronal apoptosis.[37]–[39] Gradually, focus has shifted from Aβ fibrils and plaques to oligomeric species as the cytotoxic intermediate in Aβ aggregation in brain cells.[33], [40], [41] Oligomer toxicity is supported by several observations: (i) amyloid monomers and fibrils show little cytotoxicity in contrast to intermediate aggregates,[42] (ii) transgenic mouse models show disease-like phenotypes far earlier than the appearance of fibrils in protein deposition diseases including Alzheimer's, Huntington's, and Parkinson's disease,[43], [44] and (iii) non-fibrillar soluble oligomers promote neuronal

dysfunction death.[31], [41], [45] However, it still remains unclear how these oligomers are kinetically assembled, which types of secondary oligomer conformations are involved in the disease, and through which mechanism of cytotoxicity these oligomers work on/in membranes.

1.2.3 β-Amyloid Ion Channels

The prevailing mechanism of neuronal stress in the ACH and the mechanism of focus in this dissertation is the formation of ion channels (Fig. 1.6, Fig. 1.7). Arispe et al.[34], [35], [46]–[48] first reported the groundbreaking discovery, where Aβ induced unregulated ionic flux across model membranes in planar lipid bilayer (PLB) experiments. They concluded that the ionic flux was the result of non-gated ion channels. This initiated the Aβ ion channel hypothesis (Fig. 1.7), which has subsequently been extended for other amyloids. Due to the unfavorable chemistry and there is a high thermodynamic cost of complete preformed channels sliding into the membrane, it has been suggested[49, p. 201] that Aβ oligomers can irreversibly insert into a membrane and spontaneously form an ion channel, leading to cell death (Fig. 1.7). The Aβ channels exhibited cation selectivity, Tris (tromethamine) and zinc inhibitions, and multiple and large single channel conductances. The heterogeneity of single channel conductances suggested that the channels are formed by multiple molecular species in the membrane.

Atomic force microscopy (AFM) has successfully demonstrated a remarkable ability to capture the images of channels formed by Aβ peptides. In 2001, Lin et al.[21]

presented AFM images that showed channel-like structures of $A\beta_{1-42}$ peptides when reconstituted in a planar lipid bilayer. They further showed that the channels exhibited multiple single channel conductances, calcium uptake, neuritic degeneration, and blockage by zinc. Besides AFM, using electron microscopy (EM), Lashuel et al.[50] reported pore-like structures of Aβ Arctic mutant (E22G) and A53T and A30P mutants of α-synuclein associated with Parkinson's disease. Based on these observations, it became increasingly clear that channel formation is a general feature for amyloids. Quist et al.[22] presented a series of AFM images of ion channels for a series of disease-related amyloid species, including $A\beta_{1-40}$, a-synuclein, ABri, ADan, SAA, and amylin. AFM resolution could determine that the amyloid channels have outer diameter of 8–12 nm and inner diameter ~2 nm. More interestingly, the AFM images revealed that the amyloid channels were assembled by several subunits, yielding various channel shapes from rectangular with four subunits to octahedral with eight subunits (Fig. 1.8), accounting for the multilevel conductance observed in PLB electrical recording.

An increasing body of evidence has implicated amyloid channel formations. TIRF images have displayed Ca^{2+} transients after the addition of wildtype Aβ1-42 to oocytes.[51] The flux of Ca^{2+} ions, observed only after the addition of Aβ, is in agreement with the ion channel hypothesis. The conceptual designs of Aβ channels showed a perfect annular shape with β-stands parallel to the membrane normal, or with an inclination angle between the β-strands and the membrane normal.[52]–[56] The annular channels gradually evolved in the lipid bilayer during the simulations and the relaxed channel structures exhibited heterogeneous shapes. In the AFM images, $A\beta_{1-42}$ barrels of 3-6 subunits were observed, in agreement with MD simulations (Fig. 1.8).[52]

The computational studies reported that the misfolded amyloid channels consist of loosely and dynamically associated subunits in the fluidic lipid bilayer. This is in contrast to the stable, function-optimized and evolution-preserved conventional gated ion channels, which fold into their native state. A central tenant of the amyloid channel hypothesis states that Aβ peptides directly form toxic ion channels in cell membranes leading to death of neurons in AD.

1.3 Overview of the Dissertation

As an impressive and powerful technology, the real value of AFM is in the application to meaningful scientific research. The application of AFM in this dissertation is presented in two sections: *Part I- the Structure and Activity of β-Amyloid Channels and Part II-Technology Development of Integrated Atomic Force Microscope*.

Part I focuses on utilizing the existing capabilities of AFM to study one of the most prominent medical issues facing our society, Alzheimer's Disease. In Chapter 2 and Chapter 3, I present structural results from AFM to elucidate substructures of Aβ channels. Key residues are examined with the intent to find potential therapeutic targets to prevent channel pathology. In Chapter 4, I present AFM explorations in the utilizing brain derived Aβ as well as newly developed pharmacological agents to study membranes and Aβ. Chapter 4 also presents future perspectives for therapeutic design addressing treatment and prevention of Aβ channel pathology.

In Part II I focus on development of new technology to incorporate into AFM for improved study of ion channels such as Aβ channels. Chapter 5 presents the fabrication of a novel nanopore support that fits in the AFM interface to allow for imaging and complimentary conductance measurements. Chapter 6 applies the imaging and conductance system presented in Chapter 5 to a model channel system demonstrating the benefit and proof of principle of the integrated system.

1.4 Acknowledgements

I would like to acknowledge my co-authors for this chapter, which, in part, is a reprint of the material as it appears in Physical Chemistry Chemical Physics, 2013, Jang H, Connelly L, Arce FT, Ramachandran S, Lal R, Kagan BL, Nussinov R. The dissertation author was a significant and essential investigator and author with Dr. Hyunbum Jang of this paper.

1.5 References

[1] G. Binnig, C. F. Quate, and C. Gerber, "Atomic Force Microscope," *Phys. Rev. Lett.*, vol. 56, no. 9, pp. 930–933, Mar. 1986.

[2] P. Hinterdorfer and Y. F. Dufrêne, "Detection and localization of single molecular recognition events using atomic force microscopy," *Nat. Methods*, vol. 3, no. 5, pp. 347–355, May 2006.

[3] F. O. Goodman and N. Garcia, "Roles of the attractive and repulsive forces in atomic-force microscopy," *Phys. Rev. B*, vol. 43, no. 6, pp. 4728–4731, Feb. 1991.

[4] Á. Mechler, J. Kokavecz, P. Heszler, and R. Lal, "Surface energy maps of nanostructures: Atomic force microscopy and numerical simulation study," *Appl. Phys. Lett.*, vol. 82, no. 21, pp. 3740–3742, May 2003.

[5] R. Lal, S. Ramachandran, and M. F. Arnsdorf, "Multidimensional Atomic Force Microscopy: A Versatile Novel Technology for Nanopharmacology Research," *AAPS J.*, vol. 12, no. 4, pp. 716–728, Oct. 2010.

[6] A. L. Weisenhorn, P. Maivald, H.-J. Butt, and P. K. Hansma, "Measuring adhesion, attraction, and repulsion between surfaces in liquids with an atomic-force microscope," *Phys. Rev. B*, vol. 45, no. 19, pp. 11226–11232, May 1992.

[7] M. Egger, F. Ohnesorge, A. L. Weisenhorn, S. P. Heyn, B. Drake, C. B. Prater, S. A. C. Gould, P. K. Hansma, and H. E. Gaub, "Wet lipid-protein membranes imaged at submolecular resolution by atomic force microscopy," *J. Struct. Biol.*, vol. 103, no. 1, pp. 89–94, Mar. 1990.

[8] F. J. Giessibl, "Atomic Resolution of the Silicon (111)-(7x7) Surface by Atomic Force Microscopy," *Science*, vol. 267, no. 5194, pp. 68–71, Jan. 1995.

[9] H. G. Hansma, "Surface Biology of Dna by Atomic Force Microscopy," *Annu. Rev. Phys. Chem.*, vol. 52, no. 1, pp. 71–92, 2001.

[10] P. Parot, Y. F. Dufrêne, P. Hinterdorfer, C. Le Grimellec, D. Navajas, J.-L. Pellequer, and S. Scheuring, "Past, present and future of atomic force microscopy in life sciences and medicine," *J. Mol. Recognit.*, vol. 20, no. 6, pp. 418–431, 2007.

[11] H. G. Hansma, J. Vesenka, C. Siegerist, G. Kelderman, H. Morrett, R. L. Sinsheimer, V. Elings, C. Bustamante, and P. K. Hansma, "Reproducible Imaging and Dissection of Plasmid DNA Under Liquid with the Atomic Force Microscope," *Science*, vol. 256, no. 5060, pp. 1180–1184, May 1992.

[12] J. H. Hoh, R. Lal, S. A. John, J. P. Revel, and M. F. Arnsdorf, "Atomic force microscopy and dissection of gap junctions," *Science*, vol. 253, no. 5026, pp. 1405–1408, Sep. 1991.

[13] E. Henderson, "Imaging and nanodissection of individual supercoiled plasmids by atomic force microscopy," *Nucleic Acids Res.*, vol. 20, no. 3, pp. 445–447, Feb. 1992.

[14] M. Ludwig, W. Dettmann, and H. E. Gaub, “Atomic force microscope imaging contrast based on molecular recognition,” *Biophys. J.*, vol. 72, no. 1, pp. 445–448, Jan. 1997.

[15] C. Bustamante, J. C. Macosko, and G. J. L. Wuite, “Grabbing the cat by the tail: manipulating molecules one by one,” *Nat. Rev. Mol. Cell Biol.*, vol. 1, no. 2, pp. 130–136, Nov. 2000.

[16] M. Rief, F. Oesterhelt, B. Heymann, and H. E. Gaub, “Single Molecule Force Spectroscopy on Polysaccharides by Atomic Force Microscopy,” *Science*, vol. 275, no. 5304, pp. 1295–1297, Feb. 1997.

[17] K. Salaita, Y. Wang, and C. A. Mirkin, “Applications of dip-pen nanolithography,” *Nat. Nanotechnol.*, vol. 2, no. 3, pp. 145–155, Mar. 2007.

[18] M. Porti, M. Nafría, X. Aymerich, A. Olbrich, and B. Ebersberger, “Electrical characterization of stressed and broken down SiO2 films at a nanometer scale using a conductive atomic force microscope,” *J. Appl. Phys.*, vol. 91, no. 4, pp. 2071–2079, Feb. 2002.

[19] K. T. Rodolfa, A. Bruckbauer, D. Zhou, Y. E. Korchev, and D. Klenerman, “Two-Component Graded Deposition of Biomolecules with a Double-Barreled Nanopipette,” *Angew. Chem.*, vol. 117, no. 42, pp. 7014–7019, 2005.

[20] F. Ohnesorge and G. Binnig, “True Atomic Resolution by Atomic Force Microscopy Through Repulsive and Attractive Forces,” *Science*, vol. 260, no. 5113, pp. 1451–1456, Jun. 1993.

[21] H. Lin, R. Bhatia, and R. Lal, “Amyloid beta protein forms ion channels: implications for Alzheimer’s disease pathophysiology,” *FASEB J*, vol. 15, pp. 2433–44, Nov. 2001.

[22] A. Quist, “Amyloid ion channels: A common structural link for protein-misfolding disease,” *Proc. Natl. Acad. Sci.*, vol. 102, pp. 10427–10432, 2005.

[23] J. L. Hutter and J. Bechhoefer, “Calibration of atomic-force microscope tips,” *Rev. Sci. Instrum.*, vol. 64, no. 7, pp. 1868–1873, Jul. 1993.

[24] “Latest Facts & Figures Report | Alzheimer’s Association.” [Online]. Available: http://www.alz.org/alzheimers_disease_facts_and_figures.asp#quickFacts. [Accessed: 12-Aug-2013].

[25] P. A. Temussi, L. Masino, and A. Pastore, “From Alzheimer to Huntington: why is a structural understanding so difficult?,” *EMBO J*, vol. 22, pp. 355–61, Feb. 2003.

[26] Kraepelin, E., “Kraepelin,E. (1910) Psychiatrie: Ein Lehrbuch fuÈr Studierende und Artze. Barth, Leipzig, Germany, pp. 593±632.,” *Psychiatrie*, pp. 593–632, 1910.

[27] C. M. Dobson, “Protein folding and misfolding,” *Nature*, vol. 426, pp. 884–90, Dec. 2003.

[28] D. J. Selkoe, “Folding proteins in fatal ways,” *Nature*, vol. 426, pp. 900–4, Dec. 2003.

[29] C. Soto, “Unfolding the role of protein misfolding in neurodegenerative diseases,” *Nat. Rev. Neurosci.*, vol. 4, no. 1, pp. 49–60, Jan. 2003.

[30] F. Chiti and C. M. Dobson, “Protein misfolding, functional amyloid, and human disease,” *Annu. Rev. Biochem.*, vol. 75, pp. 333–366, 2006.

[31] D. M. Walsh and D. J. Selkoe, “A beta oligomers - a decade of discovery,” *J. Neurochem.*, vol. 101, no. 5, pp. 1172–1184, Jun. 2007.

[32] J. Hardy and D. J. Selkoe, “The amyloid hypothesis of Alzheimer’s disease: progress and problems on the road to therapeutics,” *Science*, vol. 297, pp. 353–6, Jul. 2002.

[33] E. Karran, M. Mercken, and B. De Strooper, “The amyloid cascade hypothesis for Alzheimer’s disease: an appraisal for the development of therapeutics,” *Nat. Rev. Drug Discov.*, vol. 10, no. 9, pp. 698–712, Sep. 2011.

[34] N. Arispe, H. B. Pollard, and E. Rojas, “Giant multilevel cation channels formed by Alzheimer disease amyloid beta-protein [A beta P-(1-40)] in bilayer membranes,” *Proc Natl Acad Sci U A*, vol. 90, pp. 10573–7, Nov. 1993.

[35] N. Arispe, E. Rojas, and H. B. Pollard, “Alzheimer disease amyloid beta protein forms calcium channels in bilayer membranes: blockade by tromethamine and aluminum,” *Proc Natl Acad Sci U A*, vol. 90, pp. 567–71, Jan. 1993.

[36] W. M. Wojtowicz, M. Farzan, J. L. Joyal, K. Carter, G. J. Babcock, D. I. Israel, J. Sodroski, and T. Mirzabekov, “Stimulation of Enveloped Virus Infection by β-Amyloid Fibrils,” *J. Biol. Chem.*, vol. 277, no. 38, pp. 35019–35024, Sep. 2002.

[37] M. P. Mattson, B. Cheng, D. Davis, K. Bryant, I. Lieberburg, and R. E. Rydel, “beta-Amyloid peptides destabilize calcium homeostasis and render human cortical neurons vulnerable to excitotoxicity,” *J. Neurosci.*, vol. 12, no. 2, pp. 376–389, Feb. 1992.

[38] D. T. Loo, A. Copani, C. J. Pike, E. R. Whittemore, A. J. Walencewicz, and C. W. Cotman, "Apoptosis is induced by beta-amyloid in cultured central nervous system neurons," *Proc. Natl. Acad. Sci.*, vol. 90, no. 17, pp. 7951–7955, Sep. 1993.

[39] G. Smale, N. R. Nichols, D. R. Brady, C. E. Finch, and W. E. Horton Jr., "Evidence for Apoptotic Cell Death in Alzheimer's Disease," *Exp. Neurol.*, vol. 133, no. 2, pp. 225–230, Jun. 1995.

[40] M. Bucciantini, E. Giannoni, F. Chiti, F. Baroni, L. Formigli, J. Zurdo, N. Taddei, G. Ramponi, C. M. Dobson, and M. Stefani, "Inherent toxicity of aggregates implies a common mechanism for protein misfolding diseases," *Nature*, vol. 416, no. 6880, pp. 507–511, Apr. 2002.

[41] D. M. Walsh, I. Klyubin, J. V. Fadeeva, W. K. Cullen, R. Anwyl, M. S. Wolfe, M. J. Rowan, and D. J. Selkoe, "Naturally secreted oligomers of amyloid beta protein potently inhibit hippocampal long-term potentiation in vivo," *Nature*, vol. 416, pp. 535–9, Apr. 2002.

[42] C. J. Pike, D. Burdick, A. J. Walencewicz, C. G. Glabe, and C. W. Cotman, "Neurodegeneration induced by beta-amyloid peptides in vitro: the role of peptide assembly state," *J. Neurosci.*, vol. 13, no. 4, pp. 1676–1687, Apr. 1993.

[43] S. Lesné, M. T. Koh, L. Kotilinek, R. Kayed, C. G. Glabe, A. Yang, M. Gallagher, and K. H. Ashe, "A specific amyloid-beta protein assembly in the brain impairs memory," *Nature*, vol. 440, no. 7082, pp. 352–357, Mar. 2006.

[44] M. S. Goldberg and P. T. Lansbury Jr, "Is there a cause-and-effect relationship between α-synuclein fibrillization and Parkinson's disease?," *Nat. Cell Biol.*, vol. 2, no. 7, pp. E115–E119, Jul. 2000.

[45] P. J. Ebenezer, A. M. Weidner, I. LeVine, W. R. Markesbery, M. P. Murphy, L. Zhang, K. Dasuri, S. O. Fernandez-Kim, A. J. Bruce-Keller, E. Gavilán, and J. N. Keller, "Neuron Specific Toxicity of Oligomeric Amyloid-β: Role for JUN-Kinase and Oxidative Stress," *J. Alzheimers Dis.*, vol. 22, no. 3, pp. 839–848, Jan. 2010.

[46] H. B. Pollard, E. Rojas, and N. Arispe, "A new hypothesis for the mechanism of amyloid toxicity, based on the calcium channel activity of amyloid beta protein (A beta P) in phospholipid bilayer membranes," *Ann N Acad Sci*, vol. 695, pp. 165–8, Sep. 1993.

[47] N. Arispe, H. B. Pollard, and E. Rojas, "beta-Amyloid Ca(2+)-channel hypothesis for neuronal death in Alzheimer disease," *Mol. Cell. Biochem.*, vol. 140, no. 2, pp. 119–125, Nov. 1994.

[48] N. Arispe, H. B. Pollard, and E. Rojas, "Zn2+ interaction with Alzheimer amyloid beta protein calcium channels," *Proc. Natl. Acad. Sci. U. S. A.*, vol. 93, no. 4, pp. 1710–1715, Feb. 1996.

[49] H. Jang, L. Connelly, F. Teran Arce, S. Ramachandran, B. L. Kagan, R. Lal, and R. Nussinov, "Mechanisms for the Insertion of Toxic, Fibril-like β-Amyloid Oligomers into the Membrane," *J. Chem. Theory Comput.*, vol. 9, no. 1, pp. 822–833, Jan. 2013.

[50] H. A. Lashuel, D. Hartley, B. M. Petre, T. Walz, and P. T. Lansbury Jr, "Neurodegenerative disease: amyloid pores from pathogenic mutations," *Nature*, vol. 418, no. 6895, p. 291, Jul. 2002.

[51] A. Demuro, M. Smith, and I. Parker, "Single-channel Ca(2+) imaging implicates Abeta1-42 amyloid pores in Alzheimer's disease pathology," *J Cell Biol*, vol. 195, pp. 515–24, Oct. 2011.

[52] H. Jang, L. Connelly, F. T. Arce, S. Ramachandran, R. Lal, B. L. Kagan, and R. Nussinov, "Alzheimer's disease: which type of amyloid-preventing drug agents to employ?," *Phys. Chem. Chem. Phys.*, vol. 15, no. 23, pp. 8868–8877, May 2013.

[53] H. Jang, F. T. Arce, S. Ramachandran, R. Capone, R. Lal, and R. Nussinov, "β-Barrel Topology of Alzheimer's β-Amyloid Ion Channels," *J. Mol. Biol.*, vol. 404, pp. 917–934, 2010.

[54] H. Jang, F. T. Arce, R. Capone, S. Ramachandran, R. Lal, and R. Nussinov, "Misfolded Amyloid Ion Channels Present Mobile β-Sheet Subunits in Contrast to Conventional Ion Channels," *Biophys. J.*, vol. 97, pp. 3029–3037, 2009.

[55] H. Jang, J. Zheng, R. Lal, and R. Nussinov, "New structures help the modeling of toxic amyloidß ion channels," *Trends Biochem. Sci.*, vol. 33, pp. 91–100, 2008.

[56] H. Jang, J. Zheng, and R. Nussinov, "Models of β-Amyloid Ion Channels in the Membrane Suggest That Channel Formation in the Bilayer Is a Dynamic Process," *Biophys. J.*, vol. 93, pp. 1938–1949, 2007.

[57] L. Connelly, H. Jang, F. T. Arce, R. Capone, S. A. Kotler, S. Ramachandran, B. L. Kagan, R. Nussinov, and R. Lal, "Atomic force microscopy and MD simulations reveal pore-like structures of all-D-enantiomer of Alzheimer's β-amyloid peptide: relevance to the ion channel mechanism of AD pathology," *J. Phys. Chem. B*, vol. 116, no. 5, pp. 1728–1735, Feb. 2012.

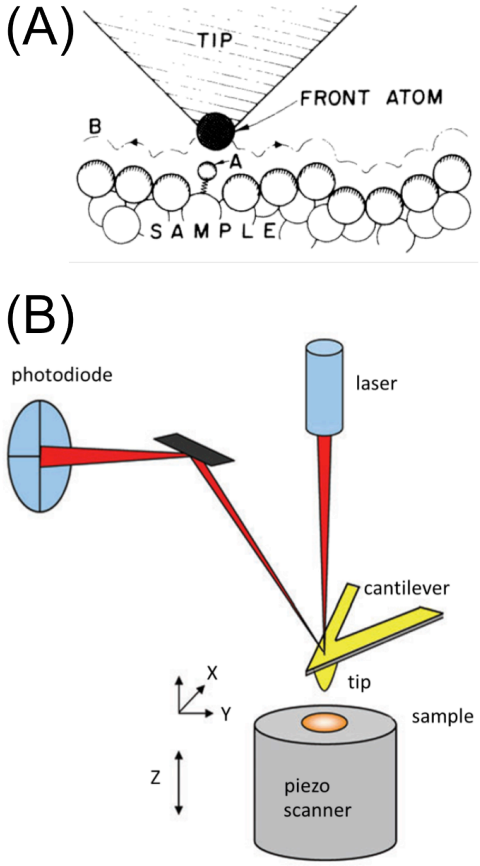

FIGURE 1.1 (A) Schematic of the principle of operation of atomic force microscopy. The front atoms of the tip interact with the surface atoms of the sample as it scans across the surface.[1] (B) Schematic of the basic parts of an atomic force microscope. A sample is mounted on a piezoelectric scanner. As the tip scans the surface of the sample, topographic changes induce a deflection of a cantilever. A laser is reflected off the back of the cantilever to a mirror and onto a photodiode. The changes of the laser deflection on the photodiode create a 3D topographical image.[2]

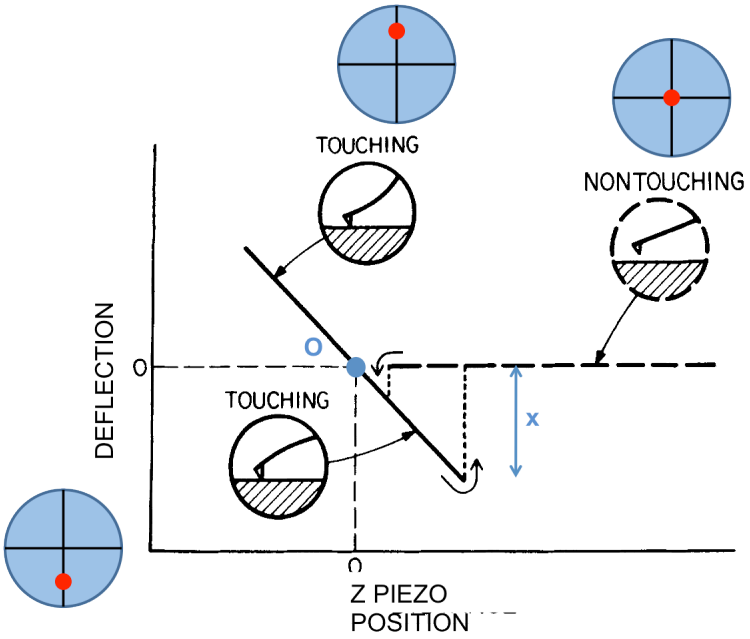

FIGURE 1.2 A schematic of a representative extension/retraction force curve in atomic force microscopy. The deflection of the cantilever is plotted in relation to the z piezo position. Also shown are sequential diagrams of the location of the laser on the photodiode during the approach and retraction (red dots in blue circles). When the tip comes close to the surface it is pulled downward by a meniscus force and the cantilever is deflected down. As the cantilever continues to approach the surface, the repulsive interaction forces cause an upward deflection. The cantilever is deflected until a set threshold is reached on the photodiode. The cantilever then retracts from the surface following the same deflection path. The retraction deflection path varies from the approach as the tip is pulled from the surface. The adhesion force holds the tip to the surface until it reaches a height sufficient to snap it off the surface.[6]

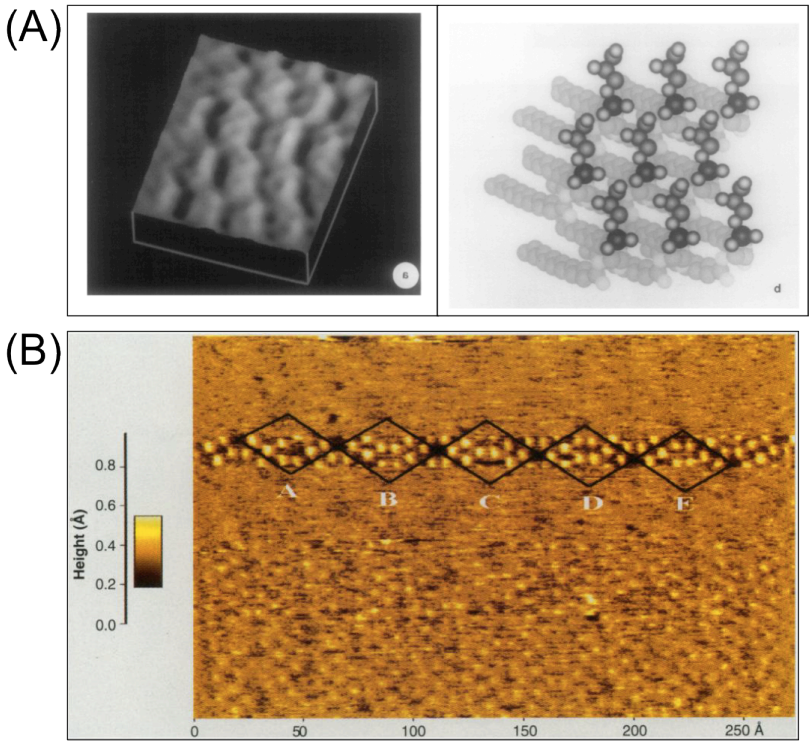

FIGURE 1.3 (A)[7] (left) High resolution AFM image of a1-α-DMPG membrane in buffer at RT on mica. The individual head groups of the lipid membrane are resolved and match the schematic to the right. Image size = 24 x 30 Å, height 0.5 Å (Right) schematic drawing of the membrane as extracted from 3-D crystal data. (B) AFM image displays atomic resolution of Si(111)-(7x7). Individual unit cells are displayed.[8]

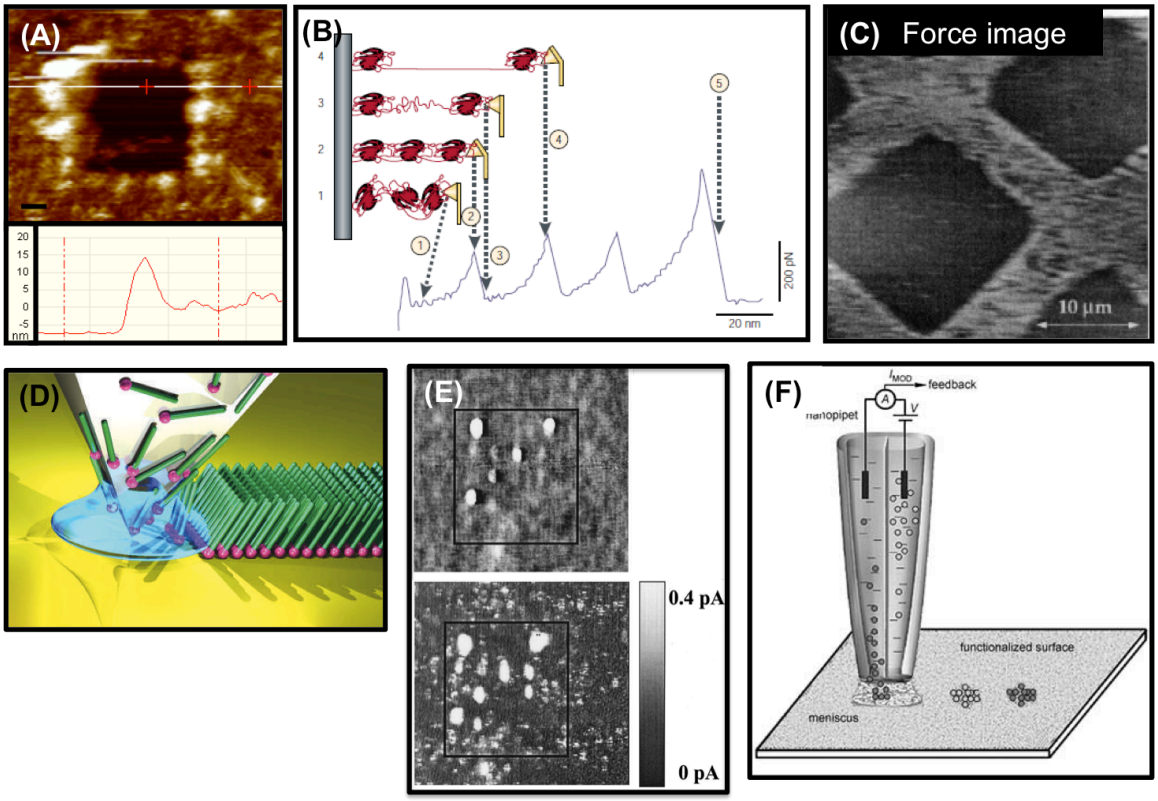

FIGURE 1.4 (A) AFM image of a force dissected area of a DOPC bilayer on mica. A strong interaction force applied to the central square area, dissects away the lipid bilayer. The height profile, shown below the images, obtained after dissection is used to measure the height of the single bilayer. The red crosses and vertical red lines mark the height measurements. (B) Schematic of AFM being used as a tensile test puller. The functionalized AFM tip "grabs" a protein attached to the surface and extends it. The force curve obtained but the unraveling of the protein reveals properties of individual domains of the protein.[15] (C) AFM FV image shows the pattern a biotin functionalized tip revealed of avidin patterned surface.[14] (D) A schematic of dip-pen nanolithography shows how an AFM tip dipped in an analytes, when in contact with a surface can "write" a pattern. The analyte diffuses from the tip and adheres to the surface.[17] (E) The top image shows an AFM height image of an SiO_2 thin film and the bottom images shows a corresponding current map of the same area. Stressed locations of the surface show a contrast in height and current to their surrounding area.[18] (F) the schematic displays how a double barrel pipette AFM tip, may be used to deposit solution or material to specific locations on a surface. Here deposition is achieved controlling the voltage between the two chambers.[19]

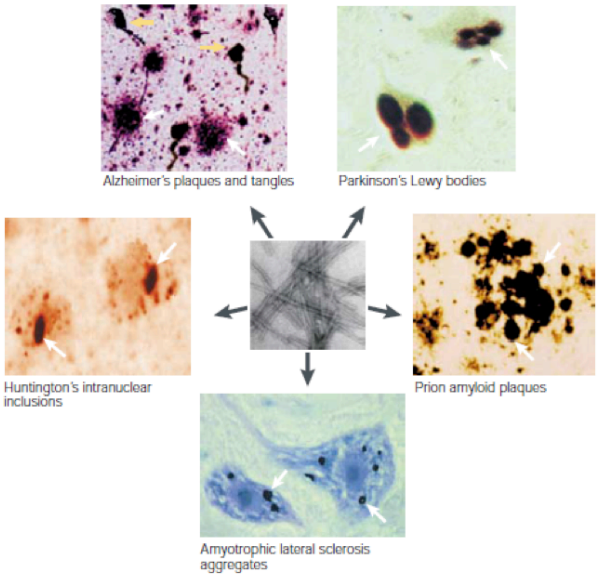

FIGURE 1.5 An electron microscope image of amyloid fibers (center imaged) is shown as a representation of the many types of amyloid plaques with their corresponding diseases. The white arrows in each image points to the plaque formation. In the Alzheimer's Disease image (top left) yellow arrows point to the NFTs.[29]

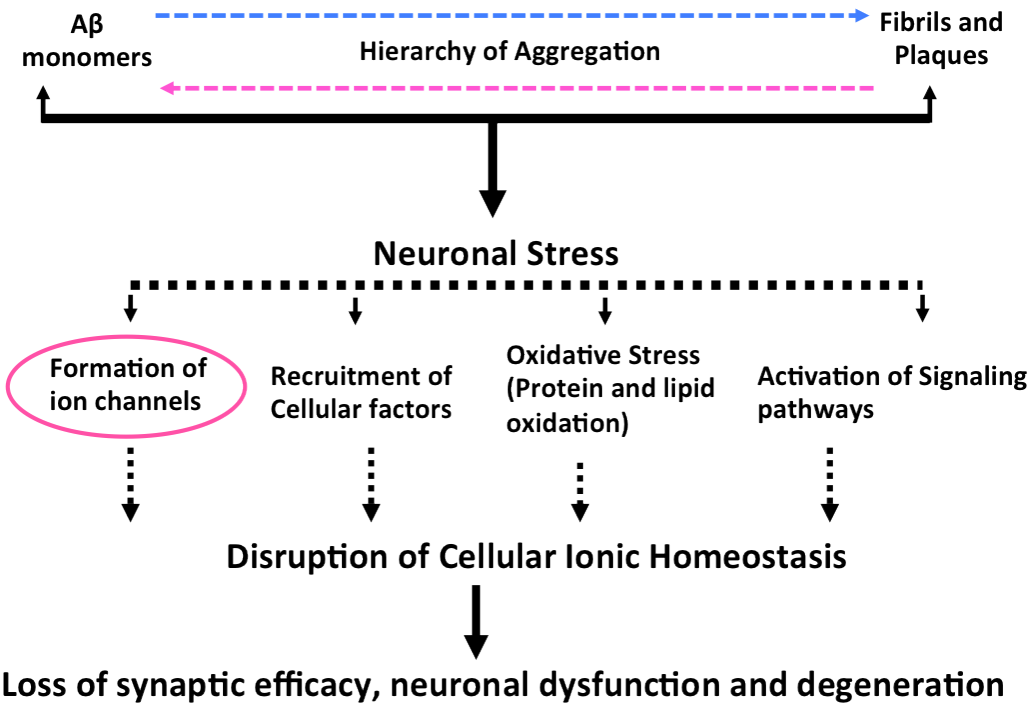

FIGURE 1.6 The amyloid cascade hypothesis (ACH) flow diagram. The hypothesis starts with the production of Aβ, which exists in a hierarchy of aggregated states from monomers to fibrils. An increase in quantity of Aβ leads to neuronal stress. The stress may arise from the formation of ion channels, recruitment of cellular factors, oxidative stress, activation of signaling pathways, or another mechanism. The focus of this dissertation and the prevailing mechanism is the formation of ion channels. Neuronal stress is exhibited as a disruption in cellular ionic homeostasis, mainly as a gain in Ca^{2+}. The final result is a loss of synaptic efficacy, neuronal dysfunction and degeneration, the characteristic symptoms of AD.

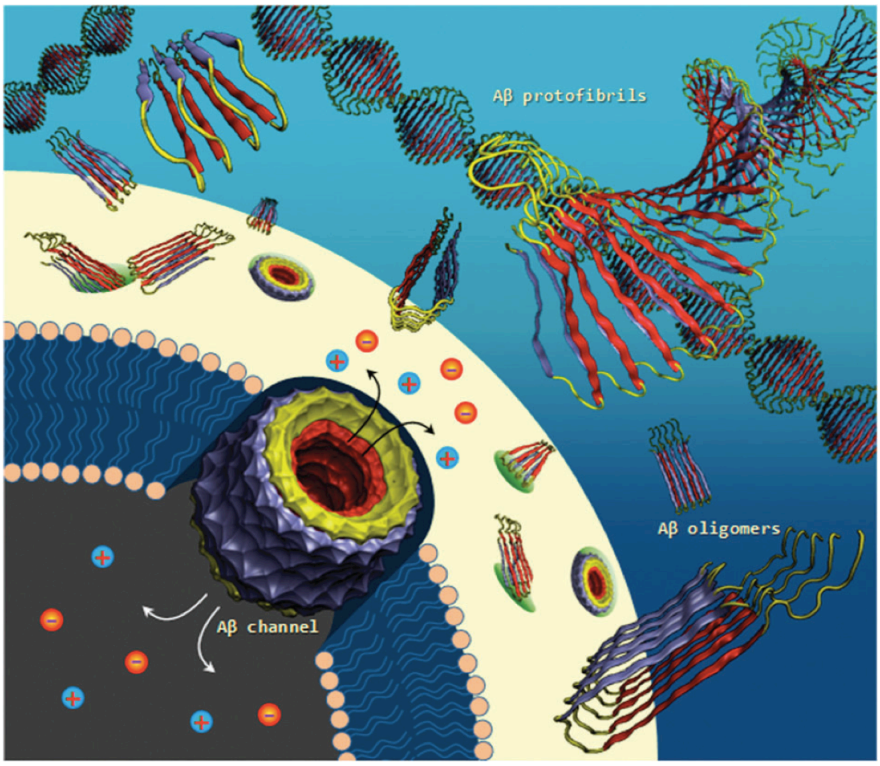

FIGURE 1.7 Schematic diagram of cell toxicity by Aβ oligomers. Small fibril-like oligomers with the parallel b-sheet structures and an exposed hydrophobic surface are believed to be toxic through a channel formation in the cell membranes.[52]

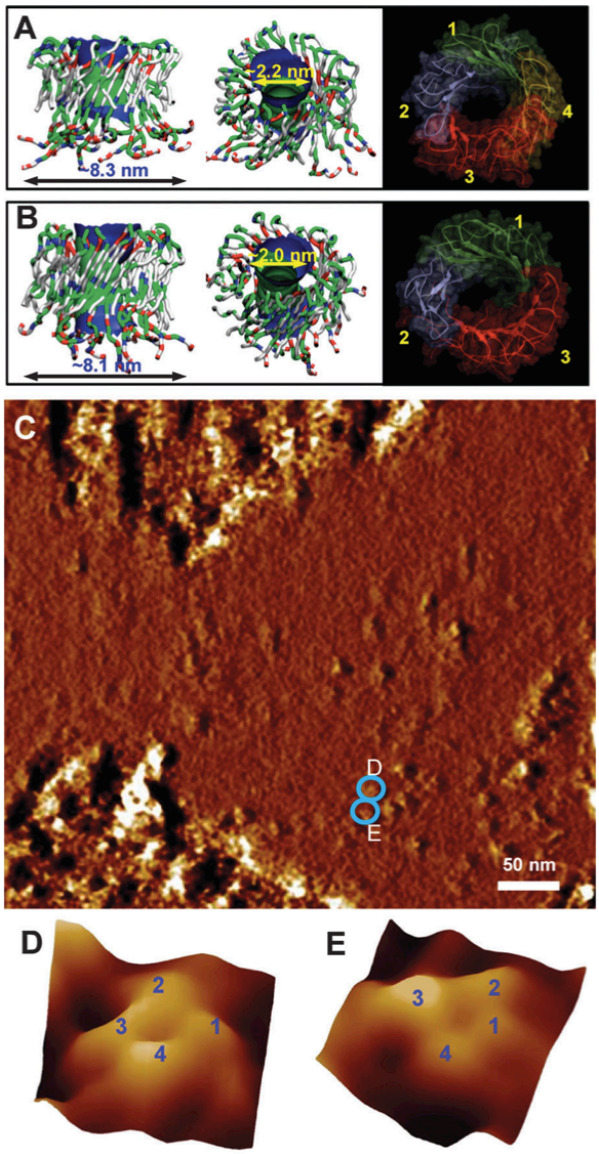

FIGURE 1.8 Full-length $A\beta_{1-42}$ channel conformations in the lipid bilayer. Simulated barrel structure with an embedded pore structure and highlighted subunits for (A) the conformer 1 and (B) the conformer 2 $A\beta_{1-42}$ barrels,[57] (C) AFM images of $A\beta_{1-42}$ reconstituted in the lipid bilayer. Individual $A\beta_{1-42}$ channels are enclosed by circles. (D and E) High resolution images of individual channels as indicated by the circles. The number of subunits is resolved and indicated for each channel. Image sizes are 18.6 nm (D) and 17.1 nm (E).[52]

PART I: STRUCTURE AND ACTIVITY OF β-AMYLOID CHANNELS

CHAPTER 2

All-D-Enantiomer of β-Amyloid

2.1 Abstract

Alzheimer's disease (AD) is a protein misfolding disease characterized by a build-up of β-amyloid (Aβ) peptide as senile plaques, uncontrolled neurodegeneration, and memory loss. AD pathology is linked to the destabilization of cellular ionic homeostasis and involves Aβ peptide-plasma membrane interactions. In principle, there are two possible ways through which disturbance of the ionic homeostasis can take place: directly, where the Aβ peptide either inserts into the membrane and creates ion-conductive pores or destabilizes the membrane organization; or, indirectly, where the Aβ peptide interacts with existing cell membrane receptors. To distinguish between these two possible types of Aβ-membrane interactions, we took advantage of the biochemical tenet that ligand-receptor interactions are stereospecific; L-amino acid peptides, but not their D-counterparts, bind to cell membrane receptors. However, with respect to the ion channel-mediated mechanism, like L-amino acids, D-amino acid peptides will also form ion channel-like structures. Using atomic force microscopy (AFM) we imaged the structures of both D- and L-enantiomers of the full length $A\beta_{1-42}$ when reconstituted in

lipid bilayers. AFM imaging shows that both L- and D-Aβ isomers form similar channel-like structures. Molecular dynamics (MD) simulations support the AFM imaged 3D structures. Earlier we have shown that D-$A\beta_{1-42}$ channels conduct ions similarly to their L-counter parts. Taken together, our results support the direct mechanism of Aβ ion channel-mediated destabilization of ionic homeostasis rather than the indirect mechanism through Aβ interaction with membrane receptors.

2.2 Introduction

Alzheimer's disease (AD) is characterized by an aberrant buildup of extracellular protein plaques, uncontrolled neurodegeneration, chronic dementia, and memory loss.[1]–[4] AD plaques are predominantly composed of β amyloid ($A\beta_{1-39\sim42}$) peptides derived from the proteolytic cleavage of its precursor protein, amyloid precursor protein (APP),[5], [6] and form amyloid structures.[7] The role of amyloidogenicity in cellular toxicity is unclear and mounting evidence supports the role of oligomeric Aβ.[8], [9] Further, the AD pathology is increasingly believed to be mediated by globular Aβ disrupting the ionic homeostasis through its interaction with cellular membranes.[10]–[14] Understanding the interaction of Aβ with the cell membrane and its effects on cellular degeneration is crucial to the understanding of the pathological origin of AD and would eventually aid the prevention and treatment of the disease.

Two mechanisms have been proposed to explain Aβ-mediated toxicity. According to the first, the Aβ peptide forms oligomeric complexes organized as pores, similar to

other cytotoxic peptides.[15] Atomic force microscopy (AFM) images support the presence of Aβ channels in lipid bilayers.[14], [16] The activity and function of these channels have been supported by electrophysiological recordings, molecular dynamics (MD) simulations, and cell calcium and degeneration studies:[17]–[22] amyloid channels conduct cations resulting in a gain-of-function type pathological response.[15], [23] According to this mechanism, Aβ inserts directly into the cell membrane and allows cellular Ca2+ uptake, thus unbalancing the cell ionic homeostasis which can lead to neurodegeneration. [10], [13], [14], [24], [25] An alternative mechanism for Aβ-mediated destabilization of ionic homeostasis suggests that the Aβ peptide interacts with the membrane via stereospecific interactions involving membrane receptors.[26]–[28] Several cellular stereospecificity studies related to Aβ membrane receptors have been reported, but with conflicting results.[27]–[29] This may be due to variation in cell lines, sample preparation and handling, and most importantly, the lack of any definite single toxic mechanism.

To distinguish between the two mechanisms, we address the question of whether such specific peptide-receptor interaction is a requirement for Aβ-mediated toxicity. Stereospecificity can be studied through comparison of the biological activities of the L- and D-enantiomers. In a stereospecific receptor-ligand relationship only L- (and not D-) amino acids are known to interact with membrane receptors. Thus, the formation of pores in the presence of the D-enantiomer-only would suggest that pore formation can take place in the absence of stereospecific interactions and as such, any cellular effect(s) would result from Aβ toxic channels directly, without receptors.

To date, there has been no study focusing on the structural stereospecificity of Aβ ionic channels. We have reported that the all L- and D-amino acids $A\beta_{1-42}$ isomers (L- $A\beta_{1-42}$ and D- $A\beta_{1-42}$, respectively) exhibit comparable channel conductivity in lipid bilayers.[30] Here, using AFM imaging and MD simulations, we present direct structural evidence for the pore-like morphology of the natural L- $A\beta_{1-42}$ peptide and its mirror image, the D- $A\beta_{1-42}$ isomer. D $A\beta_{1-42}$ retains the properties of its L-analog: the oligomer and fibril formation of the D- $A\beta_{1-42}$ are indistinguishable from the L- $A\beta_{1-42}$.

2.3 Experimental Methods

2.3.1 Materials

For storage, peptides were solubilized in ultrapure water at a concentration of 1 mg/mL, aliquoted, and stored at -80 °C. Aliquots were thawed once and used immediately. After thawing, an appropriate amount of 0.22 μm filtered NH_4OH solution was added to the aliquot to reach a 1% solution. Molecular Biology Grade water from Fisher Scientific (Pittsburgh, PA) was used for sample preparations and Dulbecco's phosphate buffered saline without Ca^{2+} and Mg^{2+} (Fisher Scientific) was used for AFM imaging in liquid. The phospholipid, 1,2-dioleoyl-sn-glycero-3-phosphocholine (DOPC) was purchased from Avanti polar lipids (Alabaster, AL).

2.3.2 AFM Imaging

A multimode AFM equipped with a NanoscopeIIIa controller (Bruker, Santa Barbara, CA) was used. Oxide sharpened cantilevers with nominal spring constants (k) of 0.02 N/m or 0.08 N/m were employed. For experiments performed in liquid, a fluid cell (Bruker) was utilized. Before each experiment, the fluid cell was washed with detergent (~5 min) and vigorously rinsed with constant stream of DI water. The fluid cell was then sonicated for 2 min in molecular grade water, dried with a Kim wipe and used immediately. Imaging in liquid was performed in phosphate-buffered saline (PBS) without Ca^{2+} and Mg^{2+}. Images in liquid were acquired in tapping mode at scan frequencies of 0.5-3.0 Hz and drive amplitudes below 100 mV. The cantilever oscillation frequency was 5-10 kHz. Image analysis was performed using the Bruker Nanoscope software. Some of the AFM images were low-pass filtered to remove noise.

Since the widths of fibers are increased in the AFM images due to tip-sample convolution we used a simple geometrical deconvolution model to obtain a good estimation of the actual size of the fiber width, ω, from the width, ω_O, observed in the AFM image,[31]–[33]

$$\omega_0 - \omega = 2(2Rh + h^2)^{1/2}$$

Here, *R* is the tip apex radius, and *h* is the height of the fiber. We assumed the tip radius to be 30 nm.[31]

2.3.3 Sample Preparation

Thawed from -80 °C, D- and L- $A\beta_{1-42}$ aliquots were mixed with 1.01% NH_4OH solution to bring the peptides to a 1% NH_4OH solution. For time-lapse imaging of peptides, these were sonicated for 20 min in an ice bath. New cantilevers or used cantilevers cleaned for 5 minutes in a UV/ozone chamber (Bioforce Nanosciences, Ames, IA) were utilized for imaging. Freshly cleaved mica was imaged in PBS without Ca^{2+} and Mg^{2+} to check for contamination before adding the peptide. The peptide-containing solution was added through the channel of the fluid cell and mixed with a pipette several times. Additional PBS was added as needed to account for evaporation. Samples were kept inside the AFM over the entire span of the experiment. The AFM was maintained at room temperature and covered with parafilm in a semi-humid environment to minimize evaporation of the peptide solution.

DOPC bilayers were formed by drying 30 μL of DOPC (10 mg/mL) dissolved in chloroform in a rotovap and replacing vacuum with Ar. The dried lipid cake was hydrated with 300 μL (1 mg/mL) of an electrolyte solution containing 150 mM KCl and 1 mM $MgCl_2$ buffered with 10 mM HEPES, pH 7.4 and vortexed gently. The liposomes formed through this procedure were sonicated for 5 minutes in an ice bath. Following thawing of the aliquoted peptide solutions, this was brought to a concentration of

1 mg/mL in 1% NH_4OH and sonicated for ~30 s. To incorporate the peptides in the lipid bilayer DOPC liposomes and peptide were combined at 20:1 weight ratio and sonicated in an ice bath for 10 min. The liposome-peptide mixture was allowed to adhere to freshly cleaved mica for 30 s and washed 10 times with PBS without Ca^{2+} and Mg^{2+}. Bilayers were imaged at room temperature.

For fibrils' preparation and imaging the peptide solutions were thawed and brought to solution concentrations of 1% NH_4OH (1 mg/mL). These were incubated in centrifuge tubes at 37 °C for up to 72 h without mixing. Incubated peptides (1 mg/mL) were allowed to adhere to freshly cleaved mica for 4 min, rinsed gently 3 times with Molecular Biology Grade Water and dried briefly under a stream of N_2.

2.3.4 Molecular Dynamics Simulations

To simulate Aβ barrels, we used two U-shaped monomer conformations: one is $A\beta_{1-42}$ as defined in the pentamer based on hydrogen/deuterium-exchange NMR data, side-chain packing constraints from pair-wise mutagenesis, solid-state NMR and EM (PDB code: 2BEG);[34] the other is $A\beta_{1-40}$ based on the solid-state NMR model of small protofibrils.[35] However, both conformers miss the N-terminal coordinates due to conformational disorder. We used the N-terminal coordinates obtained from the solution NMR structure of $A\beta_{1-16}$; however, removing the Zn^{2+} (PDB code: 1ZE7).[36] This structure was used to fill in the missing N-terminal portion of the peptides. For each combination of the N-terminal structure with the U-shaped motifs, two $A\beta_{1-42}$ conformers

were generated. Conformer 1 has a turn at Ser26-Ile31, and conformer 2 has a turn at Asp23-Gly29.30 In the latter conformer, two C-terminal residues, Ile41 and Ala42 were added to create $A\beta_{1-42}$.

The coordinates of all D-amino acids $A\beta_{1-42}$ are mirror-imaged coordinates of all L-amino acids $A\beta_{1-42}$ and can be obtained by reflecting the coordinates with respect to the reference plane. To simulate D-amino acids, a protein force field for asymmetric isomers is required. The standard CHARMM force field has been designed for L-amino acids. However, it can be directly used for D-amino acids, since a D-amino acid is a mirror-image of an L-amino acid. Thus, we adapted the same standard parameters to D-amino acids as used for the L-amino acids. However, the parameters include the dihedral angle cross term map (CMAP), which for D-amino acids needs to be corrected, since the map was constructed for L-amino acids.[37] Thus, in our simulation, we corrected CMAP for D-amino acids by reflecting the phi-psi CMAP matrix for L-amino acids.

To construct the β-barrel structure, both D- and L- $A\beta_{1-42}$ (each with two conformers) were inclined ~37° relative to the pore axis21 and then rotated 18 times with respect to the pore axis creating Aβ barrels (supplemental Fig. A.1). The construction follows known structures of β-barrel membrane proteins such as those in the outer membranes of bacteria, mitochondria, and chloroplasts, which have 8 to 22 β-strands with shear numbers ranging from 8 to 24, yielding a β-strand tilt angle range of 36° to 44° relative to the barrel axis.[38], [39] The Aβ barrels were then embedded in an anionic lipid bilayer containing 1,2-dioleoyl-sn-glycero-3-phosphoserine (DOPS) and 1-palmitoyl-2-oleoyl-sn-glycero-3-phosphoethanolamine (POPE). A unit cell containing two layers of lipids was constructed. An anionic lipid bilayer, composed of DOPS/POPE

(mole ratio 1:2) containing a total of 420 lipids, constitutes the unit cell with TIP3P waters added at both sides. For a given number of lipid molecules, the optimal value of lateral cell dimensions can be determined. The bilayer system containing an Aβ barrel, lipids, salts, and waters has almost 190,000 atoms. For the bilayer construction, we closely follow previous β-sheet channel simulations.[17]–[22], [30]

The CHARMM program[40] using the revised CHARMM27 (C27r) force field for lipids[41] and the modified TIP3P water model[42] were used to construct the set of starting points and to relax the systems to a production-ready stage. A series of minimizations were performed for the initial configurations to remove overlaps of the alkane chains in the lipids and to gradually relax the solvents around the Aβ barrel, which was held rigid. The initial configurations were gradually relaxed through dynamic cycles with electrostatic cutoffs (12 Å). In the subsequent pre-equilibrium stages, a series of dynamic cycles were performed with the harmonically restrained peptides in the channels, and then the harmonic restraints were gradually diminished until gone with the full Ewald electrostatics calculation. The entire pre-equilibration cycle took 5 ns to yield the starting point. A Nosé-Hoover thermostat/barostat was used to maintain constant temperature of 303 K. The simulations for the preequilibrations and production runs were performed on the NPAT (constant number of atoms, pressure, surface area, and temperature) ensemble. Production runs of 100 ns for the starting points with the NAMD code[43] on the Biowulf cluster (http://biowulf.nih.gov) at the NIH was used for the starting point with the same CHARMM27 force field.[40] Averages were taken after 20 ns discarding initial transients.

2.3.4 Comparison with Other Models

Recently, the $A\beta_{1-42}$ channel was also modeled into 36-mer β-barrel channels.[44] These consisted of a hexamer-of-hexamers; that is, six β-barrels each consisting of six monomers, yielding a complex of exactly 36 monomers. The transmembrane pores were proposed to form between the hexamers' barrels. The β-barrels of six hexamers span the bilayer, merging to form a 36-stranded β-barrel. In this model, two 12-stranded parallel β-barrels formed by the N-terminal domain of $A\beta_{1-42}$ are located symmetrically at both extramembranous bilayer leaflets, and 6 parallel β-strands wrap around each β-barrel. In the membrane core, 24 β-strands containing the central residues (17-21) line an inner antiparallel β-barrel forming a solvated pore and the C-terminal domain forms an outer 36-stranded antiparallel β-barrel interacting with lipids. This 36-mer barrel complex differs from our Aβ barrel in size (being considerably larger than ours), complexity (it is more complex), Aβ monomer conformation, barrel organization with respect to the bilayer (as described above), and its size uniqueness (the channel always consists exactly of hexamer-of-hexamers, i.e. 36 monomers, whereas our channels are dynamic, in consideration of bilayer fluidity, thus varied channel sizes as the loosely-associated subunits associate/dissociate). However, both models share similar residues that are engaged in a lipid-contacting outer barrel and the solvated pore. We emphasize that as always, modeling only provides models; eventually, any modeling requires direct, high

resolution experimental data. In the case of amyloids, given the heterogeneous landscape, we can expect a range of polymorphic channels.[45]

2.4 Results

2.4.1 D-Aβ_{1-42} Forms Stable Globular Units

Both D- and L- Aβ_{1-42} form oligomeric structures and these structures remain stable during the imaging by the AFM for up to a 23-25 h period. Within the first 45 min of AFM imaging after the addition of the peptide we saw mostly monomers approximately 1-2 nm in height and small oligomeric clusters (Fig. 1A). The amount of oligomeric clusters increased successively over time though no structural changes were apparent over the 23-25 h time period. Significantly, we found this pattern for both D- and L- Aβ_{1-42} peptides.

We measured the long axis of the oligomers and globular species at each time point for both isomers. We found the distribution for the D- Aβ_{1-42} oligomers to remain similar throughout the observation period (Fig. 1B). Similarly, the length distribution of the L- Aβ_{1-42} oligomers measured along their long axis, remained stable from the initial time point, at 1.5 h, throughout the ~24 h observation period (Fig. 1C). It has been shown that many factors, including concentration, affect the fibril formation kinetics.46 In our time lapsed study different concentrations were used for the D- Aβ_{1-42} (≈35 μg/mL) and

the L- $A\beta_{1-42}$ (≈13 μg/mL) peptides, therefore, the total extent of oligomerization over the observation period cannot be strictly compared between isomers. We observed the stability of the D- and L-isomers to be similar over similar time periods under similar ambient conditions.

2.4.2 D-$A\beta_{1-42}$ Forms Fibrils

Fibril formation of the $A\beta_{1-42}$ peptide incubated in ultrapure water at 37 °C for 72 h was studied in vitro to evaluate the kinetics and hierarchy of fibril structure for L- and D- $A\beta_{1-42}$.[31], [46], [47] We found the fibril formations for both isomers to be indistinguishable after 72 h of incubation (Fig. 2, A and B). Both isomers form a complex network of fibers, protofibrils, and oligomers. In both images globular complexes can be identified as well as fiber like complexes exhibiting varied widths and lengths.

Aliquots of both isomers after 72 h of incubation were diluted several times in order to identify and measure the width of individual fibrils (Fig. 2, A and B, insets). Numerous mature fibers had lengths greater than the maximum scan area (5 × 5 μm2) achievable with the scanner used for these experiments, and therefore could not be measured accurately. Random measurements of fibril widths were taken and deconvoluted.[31]–[33] We calculated the histograms of the distribution of fibril widths for both isomers (Fig. 2C). The D-isomer (gray bars) and the L-isomer (black bars) show fibers with widths most frequently between 25 nm and 30 nm. The D-isomer shows a slight bias towards thicker fiber formation. 43.2 % of the D-isomer width measurements

were between 25 nm and 35 nm. The L-isomer showed a comparable but slightly lower distribution of width measurements with 49.1 % of the measurements between 20 nm and 30 nm. The D-isomer and the L-isomer both show local minimum frequencies of width measurements just below these respective maximum ranges. The D-isomer local minimum frequency is between 20 nm and 25 nm and the L-isomer local minimum frequency is between 15 nm and 20 nm.

2.4.3 D-Aβ_{1-42} Forms Channels in Bilayers Characteristic of L-Aβ_{1-42}

The channel formation of D- Aβ_{1-42} was investigated by imaging the pores formed in supported lipid bilayers of DOPC. The DOPC lipids were chosen for their low transition temperature and consistency with previously reported evidence of Aβ_{1-42} pore formation by AFM studies and MD simulations.[14], [16]–[22], [48] The bilayer sample preparation was optimized using the L-isomer to repeat and confirm previously reported results.[14], [16] The sample preparation process was repeated exactly for the D-isomer and channels were consistently and repeatedly observed. We imaged pore-like structures in bilayer membrane by first finding the edge of the bilayer (with usual height of >5 nm with respect to the mica substrate plane) and sequentially minimizing the scan area to obtain a high resolution image of the bilayer surface. This approach ensures that the features observed were characteristic of the bilayer and inserted peptide and not due to contamination of the mica surface. Control DOPC bilayers were imaged in high resolution in the absence of the peptide and no pore-like topography was observed.

The D- $A\beta_{1-42}$ peptide forms channels in DOPC bilayers with a varying number of subunits (Fig. 3, A-C), structurally indistinguishable from the L- $A\beta_{1-42}$ channels (Fig. 3D). The pores are heterogeneous, presenting trimers, tetramers, pentamers and hexamers, with tetramers being the most prevalent observed structures (Fig. 3E). Pores were identified by the presence of individual segments forming a circular group in the amplitude image, coinciding with a small height increase with respect to the bilayer membrane surface in the AFM height image. Because of the larger size of the AFM tip compared to the typical inner diameters of ion channels (~1 nm), the AFM images only provide information relating to depths which are in close proximity of the lipid bilayer/solution interface, and cannot discern whether the individual annular structures actually traverse the entire thickness of the lipid bilayer. However, functional evidence provided by electrophysiological experiments with lipid bilayers reconstituted with $A\beta_{1-42}$ peptides suggests the presence of conductive pores, able to allow the selective passage of ions.[14], [16], [30]

The inherent tendency of amyloid peptides to adopt the β-sheet conformation leads to formation of a complex β-barrel-like channel structure comprised of several β-sheet subunits in the membrane, where lipids promote the β-sheet formation.[49]–[51] In our previous simulations, we modeled two truncated Aβ barrels, $A\beta_{17-42}$ (p3) and $A\beta_{9-42}$ (N9),[21] using U-shaped peptides with the β-strand-turn-β-strand motif.[34], [35] To model the full sequence $A\beta_{1-42}$ barrels, we again employ the U-shaped peptides as the membrane embedded portion and adopt the N-terminal structure from the $A\beta_{1-16}$ (coordinates taken from PDB code: 1ZE7)[36] as the extramembranous portion. Thus, two $A\beta_{1-42}$ conformers define the turn: at Ser26-Ile31 (Conformer 1) and at Asp23-Gly29

(Conformer 2). Using these conformers, we constructed the D- and $A\beta_{1-42}$ isomer barrels and performed 100 ns explicit MD simulations on the Aβ barrels embedded in an anionic lipid bilayer composed of DOPS/POPE (mole ratio 1:2). During the simulations, the Aβ barrels are gradually relaxed through the interaction with surrounding lipids (supplemental Fig. A.2). While small fluctuations in the membrane embedded portions including the pore and C-terminal strands strongly preserve the U-shaped structure in the Aβ barrels, large fluctuations convert the N-terminal strands to disordered chains in the bulk water area (Fig. 4). In the Aβ barrels, the fluctuation of the individual peptide's dynamics is inhomogeneous, although the dynamic motions for some adjacent peptides are correlated to each other (supplemental Fig. A.3). We note that the MD simulations employed the anionic lipid bilayer composed of DOPS/POPE, and the AFM experiments used the zwitterionic lipid bilayer with DOPC; however, the results are expected to relate. In our modeling, the peptides are pre-inserted into the membrane core and assembled to form a channel. Under these circumstances, the hydrophobic interactions between lipid-facing residues in the channel and lipid tails should be an important factor to stabilize the channel conformation, and formation of the subunits in the channel structure may not completely rely on the interaction with the negatively charged PS lipid headgroups. Further, in our previous simulations we compared the subunits in the channel conformations for the p3 ($A\beta_{17-42}$) and N9 ($A\beta_{9-42}$) channels, when embedded in zwitterionic DOPC and in anionic POPC/POPG lipid bilayers, and observed no significant differences between the two.[18], [22] Therefore, our results with the anionic bilayer are expected to display the essential characteristics of $A\beta_{1-42}$ channels in the zwitterionic bilayers.

The molecular mass of our 18-mer Aβ barrel is ~81.2 kDa, which is in the intermediate range of the Aβ channels.[18], [22] The outer/pore diameters of our simulated barrels are ~7.8/~1.9 and ~8.2/~2.1 nm for the conformer 1 and 2 D- $A\beta_{1-42}$ barrels, and ~8.3/~2.2 and ~8.1/~2.0 nm for the conformer 1 and 2 L- $A\beta_{1-42}$ barrels, respectively. The sizes measured for the barrels largely depend on the number of peptides composing the Aβ barrels and partly on the location of the extramembranous N-terminal portions. The N-terminal strands containing several charged residues stretch toward the lipid headgroups. The strong electrostatic interactions can increase the channel size; alternatively they can interact with each other at the channel mouth blocking the entry into the pore. We speculate that the interactions of the N-terminal strands near the channel mouth may correlate with features of calcium selective amyloid channels and zinc blockage. The 18-mer simulations obtained three to five subunits in the anionic bilayer (Fig. 5). As we noted in our previous simulations, subunit formations result from the fluidic lipid bilayer dynamics, and even the same channel sizes may break into different number of subunits.[17]–[22] To determine the subunits, we calculated the parameters, including the percentage of β-sheet content based on the intermolecular backbone hydrogen bonds (H-bonds), the β-strand order parameter, and the description of secondary structure, using our previous protocol (supplemental Fig. A.4). Both D- and L-isomer Aβ barrels present a range of sizes and morphologies similar to the imaged AFM channels. No difference is found between D- and L- $A\beta_{1-42}$ barrels, suggesting that both $A\beta_{1-42}$ isomers form ion channels in the lipid membrane, and thus Aβ toxicity can take place in the absence of stereospecific interactions.

2.5 Discussion

We have studied the formation of channel-like structures using all D-amino acids $A\beta_{1-42}$ and its chiral opposite, the all L-amino acids $A\beta_{1-42}$. We imaged indistinguishable pore structures formed by both isomers. Since the imaging was carried out in a lipid bilayer composed of DOPC lipids and without any inserted membrane receptors, we infer that the channel formation by the peptides in the membrane does not depend on stereospecificity. Moreover, the formation of channels in the absence of the negatively charged phosphatidylserine (PS) phospholipids as used in previous studies,[27] indicates that once inserted into the membrane, $A\beta_{1-42}$ does not rely on a stereospecific interaction with PS to form the segmented channel structure.

Based on the structure-function relationship characteristics of peptides, we reasoned that the physicochemical behavior of the all D-amino acids enantiomer of $A\beta_{1-42}$ will be identical to the naturally occurring all L-amino acids, if the structural and kinetic behavior of $A\beta_{1-42}$ is independent of chirality. Time-lapse imaging of D- $A\beta_{1-42}$ on mica showed that under appropriate physiological conditions, immediately after addition of freshly dissolved peptides, monomeric and oligomeric clusters are present and are stable over periods of time of ~23 h. Thus, these 3D structural units are characteristic of those present during the formation of pores in the presence of a lipid membrane. The physicochemical behavior of D- $A\beta_{1-42}$ in the time lapsed study was similar to that of the previously reported behavior of L- $A\beta_{1-42}$, which was also confirmed in this study.[52]

We observed the formation of $A\beta_{1-42}$ fibers and larger oligomers after 72 h of incubation at 37 °C in 1% NH_4OH. Both isomers exhibited a similar distribution of widths of fibers. The similar maximum frequency widths preceded by local minimum frequency widths is likely due to the amyloid fibers' tendency to form hierarchical fibrillar structures.[31], [53] The D-enantiomer of $A\beta_{1-42}$ showed comparable physicochemical behavior to the L-enantiomer, with monomeric and oligomeric forms stable over short periods of incubation at room temperature in physiological buffer and fiber formation over long time periods at 37 °C in ultrapure water. Therefore, the species available for channel formation in the preparation of the supported lipid membrane are monomers and oligomers, but not fibers.

Previous studies on the toxicity D- and L- $A\beta_{1-42}$ enantiomers presented conflicting results. Ciccotosto et al reported $A\beta_{1-42}$ toxicity through receptor interaction with the PS lipid flipped to the extracellular side of the lipid bilayer.[27] Cribbs et al asserted that L- and D- $A\beta_{1-42}$ show no difference in cellular toxicity.[29] Both studies focused on the binding of $A\beta_{1-42}$ to the cell membrane and the subsequent toxicity through fluorescence and viability assays. Neither study identified the mechanism of the toxicity, such as fibril adhesion, channel formation, oxidative stress, etc.[27], [29] In our study we focused on peptide insertion and channel formation with ion conductive pores in an effort to elucidate this path of toxicity and our results show that both L- and D-isomers form characteristic channels in supported lipid bilayer.

A number of cell membrane receptors which can bind to Aβ, whether in monomeric or fibrillar form, have been discussed and summarized by Verdier et al.[54] Our current data as well as our previous experiments and MD simulations performed with

model membranes reconstituted with Ab peptides in a receptor free environment,[14], [16], [20], [30] show pore-like structural features and functional activity suggestive of an ion channel conductive mechanism that does not depend on the presence of cell receptors. However, due to the very nature of these model systems, they cannot rule out the action of cell receptor mechanisms in the complex cellular environment relevant to the disease.

2.6 Conclusions

In summary, we have studied the structure of channels in the lipid membrane as well as fibril formation in solution by the naturally occurring L- $A\beta_{1-42}$ peptide and its chiral opposite, the D- $A\beta_{1-42}$ enantiomer. We show that the two isomers exhibit indistinguishable pore structures, consistent with the MD results, and similar fibril formation behavior and stability. Earlier we have shown that the D- $A\beta_{1-42}$ analog conducts ions, also in a manner indistinguishable from the L- $A\beta_{1-42}$ peptides.[30] Therefore it is likely that insertion and toxic channel formation of $A\beta_{1-42}$ does not occur through a stereospecific interaction but by a direct pathway – through an ion channel.

2.7 Acknowledgements

Chapter 2, in full, is a reprint of the material as it appears in the Journal of Physical Chemistry B, 2012, Connelly L, Jang H, Arce FT, Capone R, Kotler SA,

Ramachandran S, Kagan BL, Nussinov R, Lal R. LC completed all AFM work and drafted the manuscript. HJ completed all modeling and supplemented the manuscript. No authors had competing interests regarding the publication of this research. The dissertation author was the primary investigator and author of this paper.

This research was supported by the National Institutes of Health (National Institute on Aging AG028709 to R.L.). This project has been funded in whole or partially with Federal funds from the National Cancer Institute, National Institutes of Health, under contract number HHSN261200800001E. This research was supported (partially) by the Intramural Research Program of the NIH, National Cancer Institute, Center for Cancer Research. All simulations had been performed using the high-performance computational facilities of the Biowulf PC/Linux cluster at the National Institutes of Health, Bethesda, MD (http://biowulf.nih.gov).

2.8 References

[1] P. A. Temussi, L. Masino, and A. Pastore, "From Alzheimer to Huntington: why is a structural understanding so difficult?," *EMBO J*, vol. 22, pp. 355–61, Feb. 2003.

[2] C. M. Dobson, "Protein folding and misfolding," *Nature*, vol. 426, pp. 884–90, Dec. 2003.

[3] D. J. Selkoe, "Folding proteins in fatal ways," *Nature*, vol. 426, pp. 900–4, Dec. 2003.

[4] T. Revesz, J. Ghiso, T. Lashley, G. Plant, A. Rostagno, B. Frangione, and J. L. Holton, "Cerebral amyloid angiopathies: a pathologic, biochemical, and genetic view," *J Neuropathol Exp Neurol*, vol. 62, pp. 885–98, Sep. 2003.

[5] K. E. Neet and G. Thinakaran, "Thematic minireview series on the molecular basis of Alzheimer disease," *J Biol Chem*, vol. 283, pp. 29613–4, Oct. 2008.

[6] J. Kang, H. G. Lemaire, A. Unterbeck, J. M. Salbaum, C. L. Masters, K. H. Grzeschik, G. Multhaup, K. Beyreuther, and B. Muller-Hill, "The precursor of Alzheimer's disease amyloid A4 protein resembles a cell-surface receptor," *Nature*, vol. 325, pp. 733–6, Feb. 1987.

[7] N. Suzuki, T. T. Cheung, X. D. Cai, A. Odaka, L. Otvos, C. Eckman, T. E. Golde, and S. G. Younkin, "An increased percentage of long amyloid beta protein secreted by familial amyloid beta protein precursor (beta APP717) mutants," *Science*, vol. 264, pp. 1336–40, May 1994.

[8] D. M. Walsh, I. Klyubin, J. V. Fadeeva, W. K. Cullen, R. Anwyl, M. S. Wolfe, M. J. Rowan, and D. J. Selkoe, "Naturally secreted oligomers of amyloid beta protein potently inhibit hippocampal long-term potentiation in vivo," *Nature*, vol. 416, pp. 535–9, Apr. 2002.

[9] J. Hardy and D. J. Selkoe, "The amyloid hypothesis of Alzheimer's disease: progress and problems on the road to therapeutics," *Science*, vol. 297, pp. 353–6, Jul. 2002.

[10] N. Arispe, E. Rojas, and H. B. Pollard, "Alzheimer disease amyloid beta protein forms calcium channels in bilayer membranes: blockade by tromethamine and aluminum," *Proc Natl Acad Sci U A*, vol. 90, pp. 567–71, Jan. 1993.

[11] H. B. Pollard, E. Rojas, and N. Arispe, "A new hypothesis for the mechanism of amyloid toxicity, based on the calcium channel activity of amyloid beta protein (A beta P) in phospholipid bilayer membranes," *Ann N Acad Sci*, vol. 695, pp. 165–8, Sep. 1993.

[12] R. Bhatia, H. Lin, and R. Lal, "Fresh and globular amyloid beta protein (1-42) induces rapid cellular degeneration: evidence for AbetaP channel-mediated cellular toxicity," *FASEB J*, vol. 14, pp. 1233–43, Jun. 2000.

[13] S. K. Rhee, A. P. Quist, and R. Lal, "Amyloid beta protein-(1-42) forms calcium-permeable, Zn2+-sensitive channel," *J Biol Chem*, vol. 273, pp. 13379–82, May 1998.

[14] H. Lin, R. Bhatia, and R. Lal, "Amyloid beta protein forms ion channels: implications for Alzheimer's disease pathophysiology," *FASEB J*, vol. 15, pp. 2433–44, Nov. 2001.

[15] J. I. Kourie and A. A. Shorthouse, "Properties of cytotoxic peptide-formed ion channels," *Am J Physiol Cell Physiol*, vol. 278, pp. C1063–87, Jun. 2000.

[16] A. Quist, "Amyloid ion channels: A common structural link for protein-misfolding disease," *Proc. Natl. Acad. Sci.*, vol. 102, pp. 10427–10432, 2005.

[17] H. Jang, J. Zheng, and R. Nussinov, "Models of β-Amyloid Ion Channels in the Membrane Suggest That Channel Formation in the Bilayer Is a Dynamic Process," *Biophys. J.*, vol. 93, pp. 1938–1949, 2007.

[18] H. Jang, F. T. Arce, R. Capone, S. Ramachandran, R. Lal, and R. Nussinov, "Misfolded Amyloid Ion Channels Present Mobile β-Sheet Subunits in Contrast to Conventional Ion Channels," *Biophys. J.*, vol. 97, pp. 3029–3037, 2009.

[19] H. Jang, J. Zheng, R. Lal, and R. Nussinov, "New structures help the modeling of toxic amyloidß ion channels," *Trends Biochem. Sci.*, vol. 33, pp. 91–100, 2008.

[20] H. Jang, F. T. Arce, S. Ramachandran, R. Capone, R. Azimova, B. L. Kagan, R. Nussinov, and R. Lal, "Truncated -amyloid peptide channels provide an alternative mechanism for Alzheimer's Disease and Down syndrome," *Proc. Natl. Acad. Sci.*, vol. 107, pp. 6538–6543, 2010.

[21] H. Jang, F. T. Arce, S. Ramachandran, R. Capone, R. Lal, and R. Nussinov, "β-Barrel Topology of Alzheimer's β-Amyloid Ion Channels," *J. Mol. Biol.*, vol. 404, pp. 917–934, 2010.

[22] H. Jang, F. Teran Arce, S. Ramachandran, R. Capone, R. Lal, and R. Nussinov, "Structural Convergence Among Diverse, Toxic Œ≤-Sheet Ion Channels," *J. Phys. Chem. B*, vol. 114, pp. 9445–9451, Jul. 2010.

[23] B. L. Kagan, R. Azimov, and R. Azimova, "Amyloid Peptide Channels," *J. Membr. Biol.*, vol. 202, pp. 1–10, 2004.

[24] N. Arispe, H. B. Pollard, and E. Rojas, "Giant multilevel cation channels formed by Alzheimer disease amyloid beta-protein [A beta P-(1-40)] in bilayer membranes," *Proc Natl Acad Sci U A*, vol. 90, pp. 10573–7, Nov. 1993.

[25] A. Demuro, M. Smith, and I. Parker, "Single-channel Ca(2+) imaging implicates Abeta1-42 amyloid pores in Alzheimer's disease pathology," *J Cell Biol*, vol. 195, pp. 515–24, Oct. 2011.

[26] Y. Verdier and B. Penke, "Binding sites of amyloid beta-peptide in cell plasma membrane and implications for Alzheimer's disease," *Curr Protein Pept Sci*, vol. 5, pp. 19–31, Feb. 2004.

[27] G. D. Ciccotosto, D. J. Tew, S. C. Drew, D. G. Smith, T. Johanssen, V. Lal, T.-L. Lau, K. Perez, C. C. Curtain, J. D. Wade, F. Separovic, C. L. Masters, J. P. Smith, K. J. Barnham, and R. Cappai, "Stereospecific interactions are necessary for Alzheimer disease amyloid-β toxicity," *Neurobiol. Aging*, vol. 32, pp. 235–248, 2011.

[28] P. N. Lacor, M. C. Buniel, P. W. Furlow, A. Sanz Clemente, P. T. Velasco, M. Wood, K. L. Viola, and W. L. Klein, "A Oligomer-Induced Aberrations in Synapse Composition, Shape, and Density Provide a Molecular Basis for Loss of Connectivity in Alzheimer's Disease," *J. Neurosci.*, vol. 27, pp. 796–807, 2007.

[29] D. H. Cribbs, C. J. Pike, S. L. Weinstein, P. Velazquez, and C. W. Cotman, "All-D-enantiomers of beta-amyloid exhibit similar biological properties to all-L-beta-amyloids," *J Biol Chem*, vol. 272, pp. 7431–6, Mar. 1997.

[30] R. Capone, H. Jang, S. A. Kotler, L. Connelly, F. Teran Arce, S. Ramachandran, B. L. Kagan, R. Nussinov, and R. Lal, "All-d-Enantiomer of beta-Amyloid Peptide Forms Ion Channels in Lipid Bilayers," *J Chem Theory Comput*, vol. 8, pp. 1143–1152, Mar. 2012.

[31] M. Arimon, I. Diez-Perez, M. J. Kogan, N. Durany, E. Giralt, F. Sanz, and X. Fernandez-Busquets, "Fine structure study of Abeta1-42 fibrillogenesis with atomic force microscopy," *FASEB J*, vol. 19, pp. 1344–6, Aug. 2005.

[32] A. Relini, S. Torrassa, R. Ferrando, R. Rolandi, S. Campioni, F. Chiti, and A. Gliozzi, "Detection of Populations of Amyloid-Like Protofibrils with Different Physical Properties," *Biophys. J.*, vol. 98, no. 7, pp. 1277–1284, Apr. 2010.

[33] H. Jang, F. T. Arce, M. Mustata, S. Ramachandran, R. Capone, R. Nussinov, and R. Lal, "Antimicrobial Protegrin-1 Forms Amyloid-Like Fibrils with Rapid Kinetics Suggesting a Functional Link," *Biophys. J.*, vol. 100, pp. 1775–1783, 2011.

[34] T. Luhrs, C. Ritter, M. Adrian, D. Riek-Loher, B. Bohrmann, H. Dobeli, D. Schubert, and R. Riek, "3D structure of Alzheimer's amyloid-beta(1-42) fibrils," *Proc Natl Acad Sci U A*, vol. 102, pp. 17342–7, Nov. 2005.

[35] A. T. Petkova, W. M. Yau, and R. Tycko, "Experimental constraints on quaternary structure in Alzheimer's beta-amyloid fibrils," *Biochemistry (Mosc.)*, vol. 45, pp. 498–512, Jan. 2006.

[36] S. Zirah, S. A. Kozin, A. K. Mazur, A. Blond, M. Cheminant, I. Segalas-Milazzo, P. Debey, and S. Rebuffat, "Structural changes of region 1-16 of the Alzheimer disease amyloid beta-peptide upon zinc binding and in vitro aging," *J Biol Chem*, vol. 281, pp. 2151–61, Jan. 2006.

[37] A. D. Mackerell, M. Feig, and C. L. Brooks, "Extending the treatment of backbone energetics in protein force fields: limitations of gas-phase quantum mechanics in reproducing protein conformational distributions in molecular dynamics simulations," *J Comput Chem*, vol. 25, pp. 1400–15, Aug. 2004.

[38] G. E. Schulz, "The structure of bacterial outer membrane proteins," *Biochim Biophys Acta*, vol. 1565, pp. 308–17, Oct. 2002.

[39] D. Marsh and T. Pali, "Infrared dichroism from the X-ray structure of bacteriorhodopsin," *Biophys J*, vol. 80, pp. 305–12, Jan. 2001.

[40] B. R. Brooks, R. E. Bruccoleri, B. D. Olafson, D. J. States, S. Swaminathan, and M. Karplus, "CHARMM: A program for macromolecular energy, minimization, and dynamics calculations," *J. Comput. Chem.*, vol. 4, pp. 187–217, 1983.

[41] J. B. Klauda, B. R. Brooks, A. D. MacKerell, R. M. Venable, and R. W. Pastor, "An ab initio study on the torsional surface of alkanes and its effect on molecular simulations of alkanes and a DPPC bilayer," *J Phys Chem B*, vol. 109, pp. 5300–11, Mar. 2005.

[42] S. R. Durell, B. R. Brooks, and A. Ben-Naim, "Solvent-Induced Forces between Two Hydrophilic Groups," *J. Phys. Chem.*, vol. 98, pp. 2198–2202, Feb. 1994.

[43] J. C. Phillips, R. Braun, W. Wang, J. Gumbart, E. Tajkhorshid, E. Villa, C. Chipot, R. D. Skeel, L. Kalé, and K. Schulten, "Scalable molecular dynamics with NAMD," *J. Comput. Chem.*, vol. 26, pp. 1781–1802, 2005.

[44] Y. Shafrir, S. Durell, N. Arispe, and H. R. Guy, "Models of membrane-bound Alzheimer's Abeta peptide assemblies," *Proteins*, vol. 78, pp. 3473–87, Dec. 2010.

[45] Y. Miller, B. Ma, and R. Nussinov, "Polymorphism in Alzheimer Abeta amyloid organization reflects conformational selection in a rugged energy landscape," *Chem Rev*, vol. 110, pp. 4820–38, Aug. 2010.

[46] O. N. Antzutkin, "Amyloidosis of Alzheimer's Abeta peptides: solid-state nuclear magnetic resonance, electron paramagnetic resonance, transmission electron microscopy, scanning transmission electron microscopy and atomic force microscopy studies," *Magn Reson Chem*, vol. 42, pp. 231–46, Feb. 2004.

[47] J. D. Harper, C. M. Lieber, and P. T. Lansbury, "Atomic force microscopic imaging of seeded fibril formation and fibril branching by the Alzheimer's disease amyloid-beta protein," *Chem Biol*, vol. 4, pp. 951–9, Dec. 1997.

[48] F. T. Arce, H. Jang, S. Ramachandran, P. B. Landon, R. Nussinov, and R. Lal, "Polymorphism of amyloid beta peptide in different environments: implications for membrane insertion and pore formation," *Soft Matter*, vol. 7, pp. 5267–5273, May 2011.

[49] J. Thundimadathil, R. W. Roeske, and L. Guo, "Effect of membrane mimicking environment on the conformation of a pore-forming (xSxG)6 peptide," *Biopolymers*, vol. 84, pp. 317–328, 2006.

[50] B. L. Kagan and J. Thundimadathil, "Amyloid peptide pores and the beta sheet conformation," *Adv Exp Med Biol*, vol. 677, pp. 150–67, 2010.

[51] L. N. Zhao, S. W. Chiu, J. Benoit, L. Y. Chew, and Y. Mu, "Amyloid beta peptides aggregation in a mixed membrane bilayer: a molecular dynamics study," *J Phys Chem B*, vol. 115, pp. 12247–56, Oct. 2011.

[52] T. Kowalewski and D. M. Holtzman, "In situ atomic force microscopy study of Alzheimer's beta-amyloid peptide on different substrates: new insights into mechanism of beta-sheet formation," *Proc Natl Acad Sci U A*, vol. 96, pp. 3688–93, Mar. 1999.

[53] C. Ionescu-Zanetti, R. Khurana, J. R. Gillespie, J. S. Petrick, L. C. Trabachino, L. J. Minert, S. A. Carter, and A. L. Fink, "Monitoring the assembly of Ig light-chain amyloid fibrils by atomic force microscopy," *Proc Natl Acad Sci U A*, vol. 96, pp. 13175–9, Nov. 1999.

[54] Y. Verdier, M. Zarandi, and B. Penke, "Amyloid beta-peptide interactions with neuronal and glial cell plasma membrane: binding sites and implications for Alzheimer's disease," *J Pept Sci*, vol. 10, pp. 229–48, May 2004.

[55] O. S. Smart, J. M. Goodfellow, and B. A. Wallace, "The pore dimensions of gramicidin A," *Biophys J*, vol. 65, pp. 2455–60, Dec. 1993.

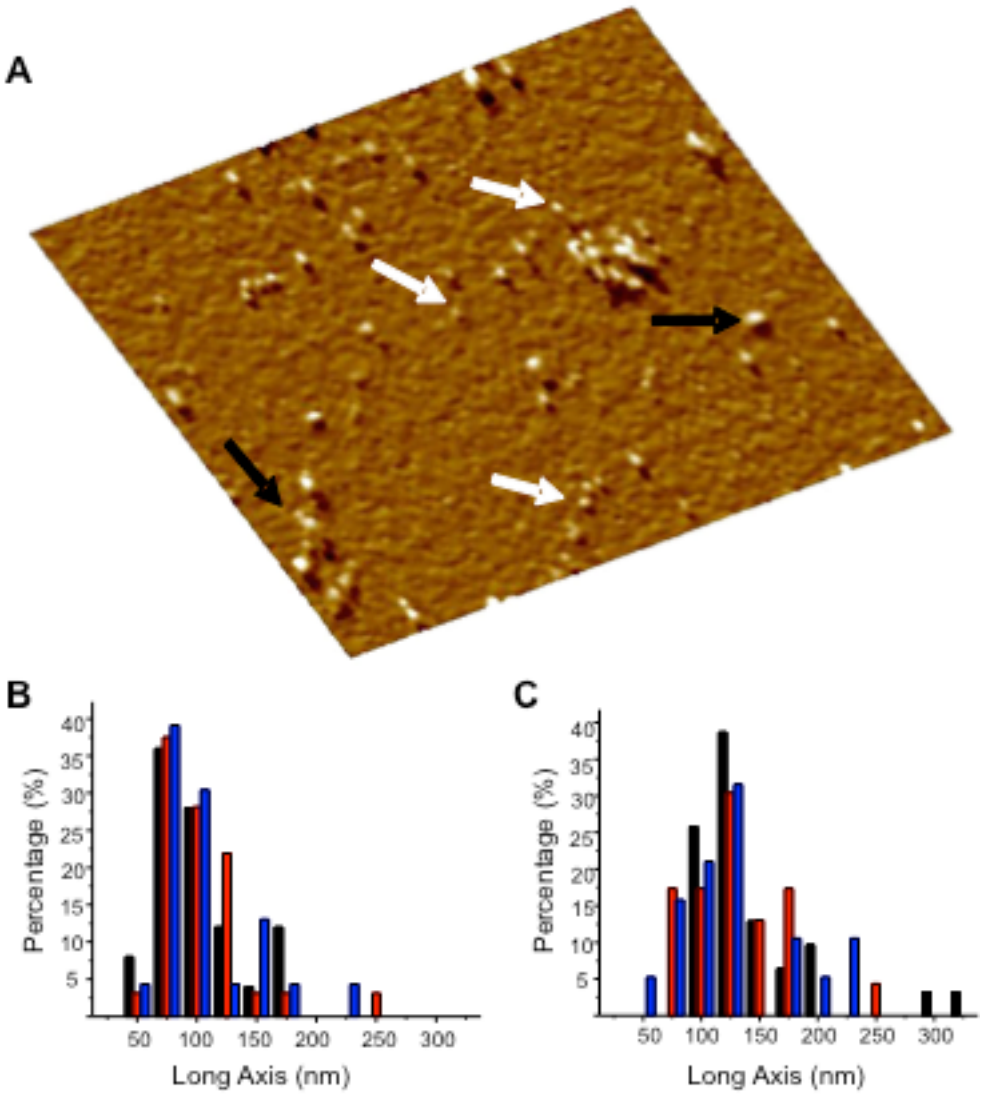

FIGURE 2.1 (A) AFM amplitude image (area 402 × 402 nm^2) of freshly dissolved all D-amino acids $A\beta_{1-42}$ in PBS without Ca^{2+} or Mg^{2+} at t = 0 of time lapsed imaging of the peptide. White arrows show peptides with heights of 1-2 nm, consistent with the size of monomers. Black arrows show higher order oligomers and clusters. The freshly cleaved mica surface was imaged in PBS solution alone to confirm zero contamination. The peptide was added to the PBS solution directly on the AFM stage to a final concentration of ≈ 35 µg/mL and the adsorbed peptide was imaged within 45 min. The length distribution of the long axis of the oligomers was measured for the (B) all D-amino acids $A\beta_{1-42}$ and (C) all L-amino acids $A\beta_{1-42}$ isomers. In B, the colors indicate: black for 1.5 h (n = 25, here n denotes the number of oligomers), red stripes for 5 h (n = 32), and blue for 23 h (n = 23). In C, the colors indicate: black for 1.5 h (n = 31), red stripes for 6 h (n = 23), and blue for 25 h (n = 19). There is little change in distribution for both isomers indicating stability of the oligomers.

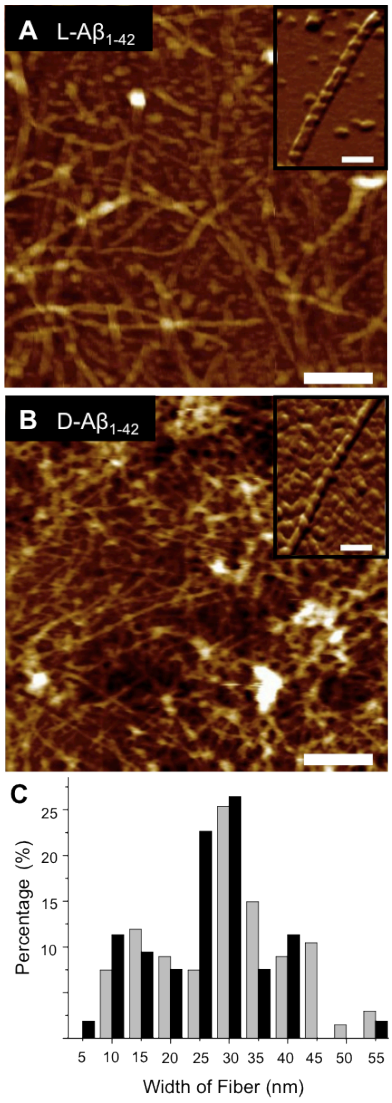

FIGURE 2.2 The (A) L- and (B) D-$A\beta_{1-42}$ isomers induced towards fibril formation in the absence of a lipid membrane by incubation in 1% NH_4OH at 37 °C for 72 h, dried overnight on fresh mica, and imaged with AFM in air. Both isomers form similar complex networks of globular units, oligomers, protofibrils, and fibrils. Insets show high resolution images of individual fibers (scale bars = 250 nm, height color scales = 25 nm, inset scale bars = 100 nm). (C) The distribution of randomly measured widths (n = 67, here n denotes the number of samples) of fibers of the D-$A\beta_{1-42}$ fibers (gray bars) after incubation at 37 °C for 72 h shows a distribution with fiber widths most frequently between 25 nm and 30 nm. The distribution of the L-$A\beta_{1-42}$ fibril widths (black bars), after similar incubation, also shows a distribution (n = 53) with fiber widths most frequently between 25 nm and 30nm. The overall range of values is comparable for both isomers.

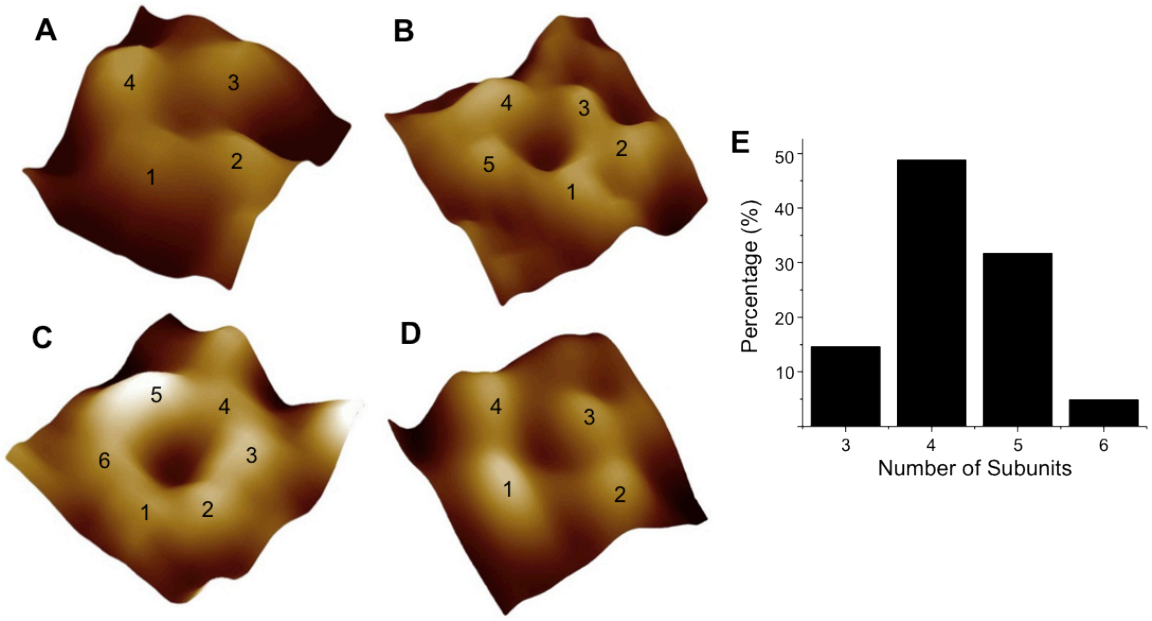

FIGURE 2.3 (A-C) AFM images of individual D-A$\beta_{1\text{-}42}$ channels in high resolution. Channels are resolved in the error mode image, seen here. These channels are heterogeneous and were observed as trimeric (*not shown*), (A) tetrameric, (B) pentameric, and (C) hexameric subunits assemblies. The channels formed by D-A$\beta_{1\text{-}42}$ are indistinguishable from the previously reported L-A$\beta_{1\text{-}42}$ channels. (D) An example AFM image of the L-A$\beta_{1\text{-}42}$ channels from the current study is shown. Channels are not observed in the absence A$\beta_{1\text{-}42}$ peptide. Image sizes are 11.5 nm for (A), 18.1 nm for (B), 13.2 nm for (C), and 14.4 nm for (D). (E) The distribution of channels formed by a varying number of A$\beta_{1\text{-}42}$ subunits. Channels with 3, 4, 5, or 6 subunits were observed. The most common structure is the channel with four subunits.

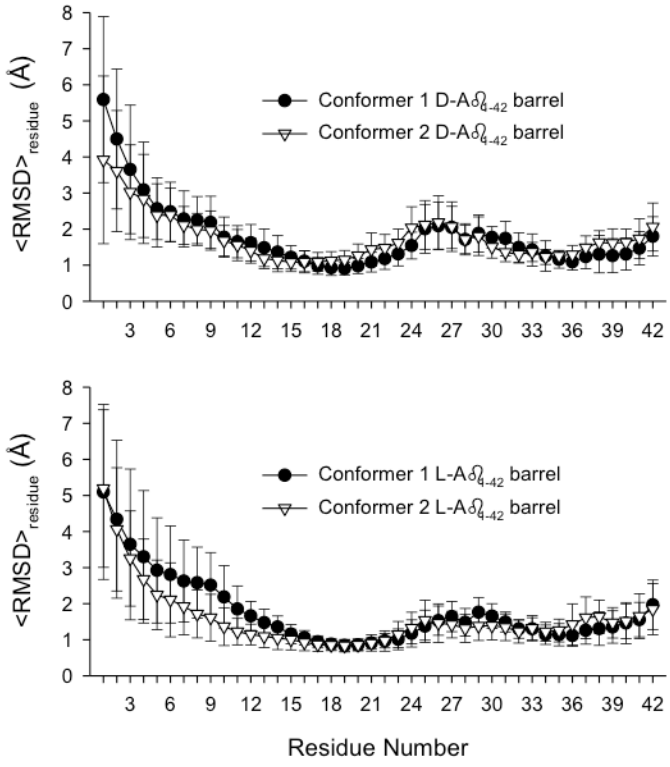

FIGURE 2.4 Residue averaged root-mean-squared deviation,$\langle RMSD \rangle_{residue}$, from the starting point for C_α atoms of the peptides for the (A) conformer 1 and 2 D-Aβ_{1-42} barrels, and the (B) conformer 1 and 2 L-Aβ_{1-42} barrels.

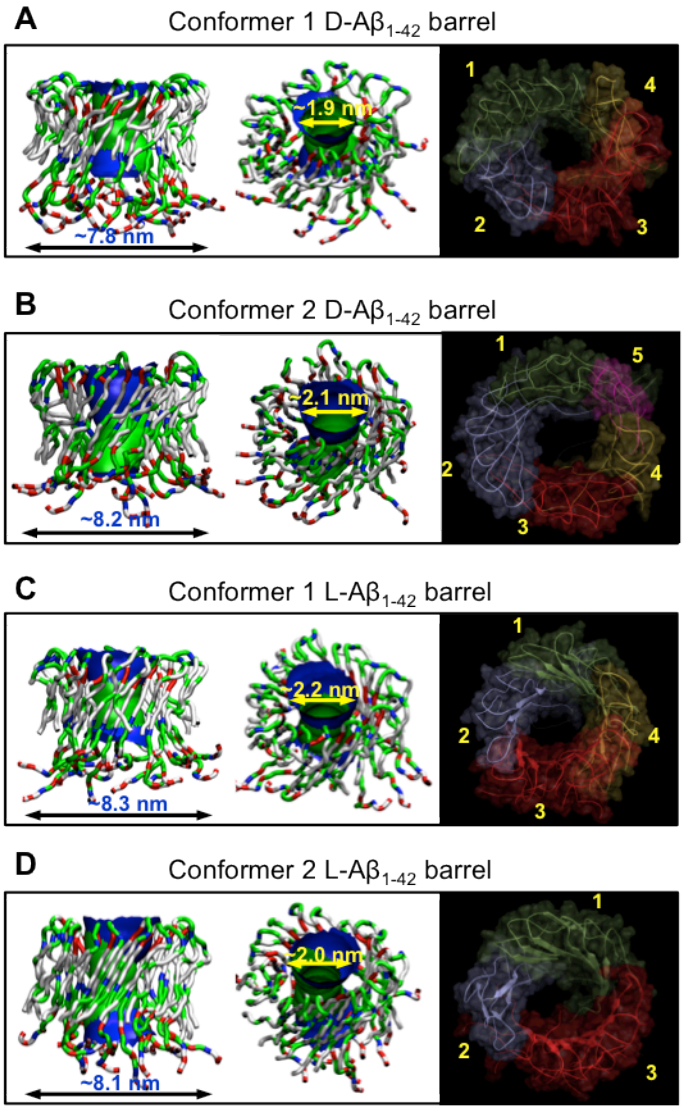

FIGURE 2.5 Averaged pore structures calculated by the HOLE program[55] embedded in the averaged barrel conformations during the simulations for the (A) conformer 1 and (B) 2 D-A$\beta_{1\text{-}42}$ barrels, and the (C) conformer 1 and (D) 2 L-A$\beta_{1\text{-}42}$ barrels. In the side (left) and angle (middle) views of the pore structure, whole barrel structures are shown with the ribbon representation. In the peptide, hydrophobic residues are shown in white, polar and Gly residues are shown in green, positively charged residues are shown in blue, and negatively charged residues are shown in red. For the pore structures in the surface representation, red denotes pore radius of $r < 0.9$ nm, green denotes pore radius in the range, 0.9 nm $\leq r \leq$ 1.1 nm, and blue denotes pore radius of $r > 1.3$ nm. The simulated barrel structures (right) with highlighted subunits for the averaged barrels in the surface representation are shown in the view along the membrane normal.

CHAPTER 3

Effects of Point Substitutions on the Structure and Activity of β—Amyloid Channels

3.1 Abstract

Alzheimer's disease (AD) is a misfolded protein disease characterized by the accumulation of β-amyloid (Aβ) peptide as senile plaques, progressive neurodegeneration, and memory loss. Recent evidence suggests that AD pathology is linked to the destabilization of cellular ionic homeostasis mediated by toxic pores made of Aβ peptides. Understanding the exact nature by which these pores conduct electrical and molecular signals could aid in identifying potential therapeutic targets for the prevention/treatment of AD. Here using atomic force microscopy (AFM) and molecular dynamics (MD) simulations, we compared the imaged pore structures with models to predict channel conformations as a function of amino acid sequence. Site-specific amino acid (AA) substitutions in the wild type $A\beta_{1-42}$ peptide yield information regarding the location and significance of individual AA residues to its characteristic structure-activity relationship. We selected two AAs that our MD simulation predicted to inhibit or permit pore conductance. The substitution of Phe19 to Pro (F19P) has previously been shown to eliminate conductance in the planar lipid bilayer (PLB) system. Our MD simulations predict a channel-like shape with a collapsed pore, which is supported by the AFM channel images. We suggest that proline, a known β-sheet breaker, creates a kink in the

center of the pore and prevents conductance via blockage. This residue may be a viable target for drug development studies aiming to inhibit Aβ from inducing ionic destabilization toxicity. The substitution of Phe20 with Cys (F20C) exhibits pore structures indistinguishable from the wild type in AFM images. MD simulations predict site 20 to face the solvated pore. Overall, the mutations support the previously predicted β-sheet-based channel structure.

3.2 Introduction

The β-amyloid (Aβ) peptide is the primary component of extracellular fibrillar deposits, termed amyloid plaques, found post mortem in brain tissues of patients with Alzheimer's disease (AD).[1], [2] These peptides are able to form distinct polymorphic structures, ranging from globular oligomers to mature fibrils.[2]–[4] Fibrillar structures have been widely investigated through in vivo and in vitro studies,[5]–[7] but interest has gradually shifted towards smaller oligomers, as increasing evidence points to the structures formed by these oligomers as the pathogenic agents involved at the onset of AD.[4], [8]–[10] More recently, the amyloid channel hypothesis that postulates the presence of pore structures, formed by small oligomers which are able to disrupt cellular ionic homeostasis, is emerging as one of the principal hypotheses associated with pathogenesis.[9], [11]–[14]

Point mutations in the amyloid precursor protein (APP) located within or in close vicinity of the full length Aβ peptide have been linked to disease.[15], [16] Of particular

interest, are the mutations clustered around a central hydrophobic cluster of Aβ. These include the E22Q point mutation, associated with hereditary cerebral hemorrhage by amyloidosis of the Dutch-type (HCHWA-D); the E22G mutation, known as the arctic mutation; and the A21G mutation, known as the Flemish mutation, related to cerebral amyloid angiopathy (CAA) and pre-senile dementia.[15], [16] Proline mutations in this central region have attracted particular interest, as they have been shown to suppress β-sheet and fibril formation in the Aβ peptide and fragments thereof.[17]–[20] The β-sheet conformation in individual Aβ peptides has been modeled as essential to the formation of cell membrane penetrating pores.[21]–[23] Cysteine mutations have also been investigated in this central region, with L17C and V18C point mutations resulting in decreased fibril formation, but F20C produced a similar degree of fibril formation as the $A\beta_{1-40}$ wild type.[24]

Using Molecular Dynamics (MD) simulations of pores formed by $A\beta_{17-42}$ (p3) peptides inside lipid bilayers, we have previously suggested that the central cluster of the full-length $A\beta_{1-42}$ sequence is located in the β-sheet lining the pore region.[23], [25]–[27] According to these MD simulations using the U-shaped peptides with the β-strand-turn-β-strand motif, the more hydrophilic N-terminus lines the pore, while the more hydrophobic C-terminus lines the lipid bilayer. In recent studies, a F19P point substitution to the p3 peptide (p3-F19P) and to the full length $A\beta_{1-42}$ was shown to form collapsed pores, unable to conduct ionic currents across lipid bilayers.[25], [28] In this paper, we have used atomic force microscopy (AFM) and MD simulations to investigate the effect of F19P and F20C mutations on the pore structures formed by the full-length $A\beta_{1-42}$ peptide inside lipid bilayers. We correlate these point substitutions in the amino

acid sequence of Aβ with changes in the pore structure, propensity for β-sheet formation, variations in the peptide-peptide as well as peptide-lipid interaction energies, and different energy landscape for ions inside the pores. Adding to previous data, this new study helps elucidate the structure-activity relationship of Aβ as a toxic pore and provides additional evidence that Aβ pores destabilize cellular ionic homeostasis.

3.3 Experimental Methods

3.3.1 Materials

For storage, peptides were solubilized in 1% NH_4OH ultra-pure solution at a concentration of 1 mg/mL, separated into aliquots, and stored at -80 °C. Aliquots were thawed once and used immediately. Molecular Biology Grade water from Fisher Scientific (Pittsburgh, PA) was used for sample preparations. Electrolyte solutions at pH 7.4, containing 150 mM KCl, 1 mM $MgCl_2$ and buffered with 10 mM HEPES were used for AFM imaging in liquid. The phospholipid, 1,2-dioleoyl-sn-glycero-3-phosphocholine (DOPC) was purchased from Avanti polar lipids (Alabaster, AL). Peptides were purchased from Bachem (Torrance, CA).

3.3.2 Atomic Force Microscopy Imaging

Multimode AFMs equipped with a Nanoscope IIIa controller and a Nanoscope IV controller (Bruker, Santa Barbara, CA) were used. Oxide sharpened cantilevers (Asylum Research, Santa Barbara, CA) with nominal spring constants (kn) of 0.02 N/m or 0.08 N/m were employed. For experiments performed in liquid, a fluid cell (Bruker) was utilized. Before each experiment, the fluid cell was washed with detergent (~5 min) and vigorously rinsed with constant stream of DI water. The fluid cell was then sonicated for 2 min in molecular grade water, dried with a Kim wipe and used immediately. In some cases the liquid cell, with cantilever mounted, was UV/ozone cleaned for 30 min. Images in liquid were acquired in tapping mode at scan frequencies of 0.5 - 3.0 Hz and drive amplitudes below 100 mV. The cantilever oscillation frequency was 5 - 10 kHz. Imaging of dried fiber samples were performed in air in contact mode. Some of the AFM images were low-pass filtered to remove noise. Image analysis was performed using the Bruker Nanoscope software. The average outer diameters of the wild type, F19P, and F20C pores were determined using the NanoScope software Analyze Width feature and Circular dimensions option. The area of the pore was determined by selecting a local maximum in the correlation graph that corresponded with a zoomed in area of the pore.

3.3.3 Sample Preparation

DOPC bilayers were formed by drying 60 μL of DOPC (5 mg/mL) dissolved in chloroform in a rotovap and replacing vacuum with Ar. The dried lipid cake was hydrated with 300 μL (1mg/mL) electrolyte solution containing 150 mM KCl and 1 mM $MgCl_2$ buffered with 10 mM HEPES, pH 7.4 and vortexed gently. The liposomes formed through this procedure were sonicated for 5 mins in an ice bath. Following thawing of the F19P and F20C mutants solutions, aliquots were sonicated for ~1 min and immediately incorporated into liposomes of DOPC. To incorporate the peptides in the lipid bilayer DOPC liposomes and peptide were combined at 20:1 weight ratio and sonicated in an ice bath for 10 min. The liposome-peptide mixture was allowed to adhere to freshly cleaved mica for 30 s and washed 10 times with the electrolyte solution. Bilayers were imaged at room temperature. For imaging of fibers, aliquots of peptide in water were thawed and incubated without shaking for 72 h at 37 °C. The aliquots were then diluted and deposited on fresh mica and allowed to dry overnight.

3.3.4 Molecular Dynamics Simulations

To model Alzheimer's Aβ channels, we conceptually designed an Aβ barrel in an annular shape using two U-shaped monomers: one is $A\beta_{1\text{-}42}$ as defined in the fibril based

on hydrogen/deuterium-exchange NMR data, side-chain packing constraints from pair-wise mutagenesis, solid-state NMR and EM (PDB code: 2BEG);[29] the other is $A\beta_{1-40}$ based on the solid-state NMR model of small protofibrils.[30] However, both conformers miss the N-terminal coordinates due to conformational disorder. We used the N-terminal coordinates obtained from the solution NMR structure of $A\beta_{1-16}$; however, removing the Zn^{2+} (PDB code: 1ZE7).[31] This structure was used to fill in the missing N-terminal portion of the peptides. For each combination of the N-terminal structure with the U-shaped motifs, two $A\beta_{1-42}$ conformers were generated. Conformer 1 has a turn at Ser26-Ile31, and conformer 2 has a turn at Asp23-Gly29.[32], [33] In the latter conformer, two C-terminal residues, Ile41 and Ala42 were added to create $A\beta_{1-42}$. For convenience, We divided both Aβ conformers into four domains: N-terminal chain (residues 1-16 and 1-8 for conformer 1 and 2, respectively), pore-lining β-stand (residues 17-25 and 9-22 for conformer 1 and 2, respectively), turn (residues 26-31 and 23-29 for conformer 1 and 2, respectively), and C-terminal β-stand (residues 32-42 and 30-42 for conformer 1 and 2, respectively).

For both conformers, we replaced two phenylalanine residues, Phe19 and Phe20 with Pro19 and Cys20 respectively, creating coordinates for F19P and F20C point mutants (Figure 3.1A,B). Now we have six Aβ1-42 monomer conformations, wild type and two mutants from each conformer, which are subjected to the Aβ barrel simulations. These Aβ conformers were inclined ~37 ° relative to the pore axis,[26] and then rotated 18 times with respect to the pore axis creating Aβ barrels (Figure 3.1C,D). These Aβ barrels were embedded in an anionic lipid bilayer containing 1,2-dioleoyl-sn-glycero-3-phosphoserine (DOPS) and 1-palmitoyl-2-oleoyl-sn-glycero-3-phosphoethanolamine

(POPE) (mole ratio 1:2). The anionic lipid bilayer containing a total of 420 lipids constitutes the unit cell with TIP3P waters, added at both sides. The system contains Mg^{2+}, K^{+}, Ca2+, and Zn^{2+} at the same concentration of 25 mM to satisfy a total cation concentration near 100 mM. The CHARMM program[34] was used to construct the set of starting points and to relax the systems to a production-ready stage. For production runs, the NAMD code[35] on the Biowulf cluster (http://biowulf.nih.gov) at the NIH was used for the starting point with the same CHARMM27 force field. Averages were taken after 20 ns discarding initial transients. Analysis was performed with the CHARMM programming package.[34] More detailed simulations methods can be found elsewhere.[25]–[27], [32], [33], [36], [37]

3.4 Results

3.4.1 AFM Analysis of F19P and F20C Pore Structure

High resolution AFM images of F19P and F20C mutants of $A\beta_{1-42}$ incorporated in a DOPC bilayer supported on mica were acquired. When the presence of a single bilayer was confirmed by imaging hole defects with characteristic depths of ~4 nm, high resolution imaging of the pores was attempted in the vicinity of the defect. The pores produced by the F19P mutant in DOPC bilayers show similar behavior as the previously reported full-length wild type $A\beta_{1-42}$ (Figure 3.2A).[9], [12] The pores could be identified

as central dips inside doughnut-like structures and in some cases individual subunits appeared as protrusions in the amplitude images (Figure 3.2B). The pores were seen in the AFM images prior to noise removal (Figure S1, Supporting Information). The pore structures of F19P are multimeric. Trimers, tetramers, and pentamers were identified (Figure 3.2B). Many of the structures observed could not be resolved into individual subunits. These unresolved structures may indicate the presence of globular oligomers or inability of the AFM tip to resolve the subunits. For the F20C peptide, the protruding structures appeared clustered and could be seen within scan areas of 500 × 500 nm2 (Figure 3.2C and Figure S1, Supporting Information). While the majority of the F20C pores were seen as pentamers, wild type $A\beta_{1\text{-}42}$ typically showed a preference for trimeric to hexameric pore conformations (Figure 3.2D).[9], [12] The F20C pore structures were seen in unprocessed AFM images (Figure S1, Supporting Information).

Height images without noise removal for both F19P and F20C (Figure S1A, C, Supporting Information), acquired simultaneously to the amplitude images, clearly indicate a pore structure. From AFM images the average pore diameter (± standard deviation) was 11.3 ± 1.6 nm (n = 16) for the wild type $A\beta_{1—42}$, 11.2 ± 1.6 nm (n = 16) for the F19P, and 7.9 ± 1.4 nm (n = 16) for F20C, as shown in (Figure 3.2E).

The F19P peptide was incubated for 72 h in water at 37 °C, dried on fresh mica, and imaged in air. Fiber formation appeared similar to previously reported images of the wild type peptide (Figure 3.3). This incubation and imaging was preformed several times with different batches of peptide. Each sample set showed fiber formation had occurred.

3.4.2 MD Simulations of F19P and F20C Pore Structure

We performed 100 ns explicit all-atoms molecular dynamics (MD) simulations on Aβ barrels, assembled by wild type $A\beta_{1-42}$ and its F19P and F20C mutants, embedded in an anionic lipid bilayer composed of DOPS/POPE (mole ratio 1:2). In the lipid bilayer, the Aβ barrels gradually removed the initial frustration in the annular conformation via relaxation of the lipid bilayer. We calculated the interaction energy for each peptide's U-shaped portion with the lipids and then averaged the interaction energy over the number of peptides as a function of the simulation time (Figure S2, Supporting Information). The effect of point mutation is not immediately reflected in the peptide-lipid interaction, since both point mutations occurred in the pore-lining β-strands that face the solvated pore. The lipids are in proximity to the hydrophobic C-terminal β-strands. However, the point mutations elicit peptide fluctuations during the simulations. In particular, the pore-lining β-strands are less stable due to the mutated residues compared to the wild type, increasing the overall peptide fluctuations (Figure 3.4). Large fluctuations in the N-terminal domains indicate that they are disordered chains in the bulk water area, while small fluctuations in the U-shaped portion including the pore-lining β-strand, the turn, and the C-terminal β-stand suggest that the U-shaped portions sustain the assembled Aβ barrel structures.

The 18-mer $A\beta_{1-42}$ barrels gradually relax during the simulations. Heterogeneous Aβ barrel structures are presented as cartoon for both conformers and for the wild type and two mutants barrels (Figure 3.5). The cartoons represent the averaged barrel structures embedding the averaged pore structures as calculated by the HOLE

program.[38] Regardless of the point mutations, the outlines of the Aβ barrels in each conformer are very similar to each other. However, the inner water pore structures are significantly evolved toward a collapsed pore in the mutant barrels. While both conformer 1 and 2 wild type barrels preserve a fat-tube-like pore, wide enough for active ion conductance, the F19P pores are completely clogged up and collapsed with conformer 1 and 2, respectively. In previous simulations, we observed that p3-F19P mutant also form a collapsed pore.[25] The conformer 1 F19P has the same U-shape as the p3-F19P mutant, but contains an extra N-terminal chain composing of residues 1 - 16. With F20C mutations, conformer 1 preserves a wide pore, while conformer 2 yields a partially collapsed pore. The calculated outer dimensions and pore sizes are summarized (Table 1). Both mutants decrease the outer and pore diameters.

In the F19P barrel, kinks at Pro19 destabilize an inner β-sheet formed by the pore-lining β-strands. As a result, the N-terminal chains containing highly charged residues bind to each other at the channel mouth in the lower bilayer leaflet. These N-terminal chains interactions are responsible for the collapsed pore observed in the F19P mutant barrels. In the wild type barrels, the N-terminal chains interactions are in proximity, i.e. mostly interacting with neighboring chains. For example, a contour map representing N-term/N-term interaction energy for the conformer 1 wild type barrel shows strong interactions along the diagonal, indicating neighboring chains interactions (Figure 3.6A). In contrast, for the conformer 1 F19P mutant barrel contour lines enclosing the strong N-terminal chains interactions are dispersed from the diagonal line, indicating that some chains are cross-linked to other chains at opposite side (Figure 3.6B). In the F20C barrels,

although the mutation did not provide a kink, the conformer 2 barrel produces a smaller pore compared to the wild type.

3.5 Discussion

Oligomeric Aβ's role in the pathology of Alzheimer's disease is a growing area of interest. The ability to form fibers and bind Congo red is characteristic of many amyloids including wild type Aβ.[39]–[41] Previous studies of the F19P mutation have reported an inability to form such characteristic fibers and bind Congo red.[17], [19] Such differences in the mutant behavior to the wild type, suggests that the F19P point substitution causes a significant functional change to the peptide. Similarly, we have observed that the F19P mutant of the p3 ($A\beta_{17-42}$) peptide has the ability to elicit changes in the functional behavior of the wild type Aβ17-42. The p3-F19P mutant forms collapsed pores that do not allow ion conductance through planar lipid bilayers and do not alter the intracellular Ca^{2+} levels in mouse fibroblast cells.[25] Consistent with that behavior, we have found that the characteristic ion conductance of wild type $A\beta_{1-42}$ is completely inhibited by the F19P mutant.[28] Although fiber formation, Congo red binding, and conductance of the F19P mutation have been previously reported to prevent amyloidogenic behavior, the effect of the F19P mutation on pore formation has not been examined for the full length Aβ. Following the behavior presented by the p3 peptide, we hypothesized that the pore structure would also be significantly different from the wild type for the full-length $A\beta_{1-}$

$_{42}$. We sought to determine if F19P prevents insertion into the lipid bilayer or F19P inserts effectively but results in a structurally compromised pore.

Through AFM analysis we show that F19P is capable of insertion into the bilayer and the pore formation on the bilayer surface is structurally indistinguishable from the wild type. AFM image analysis reports that the channels are multimeric as observed in the wild type and have outer diameters similar to the wild type. MD simulations show that the overall outer morphologies of the F19P barrels are very similar to the wild type. Also, the outer dimensions of the F19P barrels are in the experimental range, although slightly smaller than the wild type. In the MD simulations, the outer size measured for the barrels mainly depends on the number of Aβ peptides composing of the barrels. Here, we reported the values for 18-mer Aβ barrels. The AFM experiments provide images of channels with a wide variety of sizes and shapes, but simulated Aβ barrels are limited to cover all ranges of channel sizes that are imaged by AFM. MD simulations support the hypothesis that the different functional behavior of wild type $A\beta_{1\text{-}42}$ and F19P channels is due to a modified channel structure. Although the F19P pores are collapsed or clogged, the AFM images do not reveal any change in its internal dimensions because the AFM tip is unable to penetrate deep enough inside the pore to detect a change in the inner pore diameter (Figure 3.5). Overall through MD simulations and AFM imaging we found F20C to be indistinguishable from the wild type $A\beta_{1\text{-}42}$. This is in good agreement with previous activity reports that both the wild type, p3-F20C, and full length F20C mutant presented ion conductance by electrophysiology and p3-F20C altered intracellular Ca2+ levels.[25], [28]

The similar structural behavior of pores formed from wild type as well as F19P and F20C mutants for the full length $A\beta_{1-42}$ and the $A\beta_{17-42}$ fragment in simplified lipid compositions might suggest that the amyloidogenic and non-amyloidogenic pathways can be similarly disruptive to cell membranes. The fact that both pathways are not equally pathogenic to cells is probably due to the presence of additional biochemical processes related to the cellular network and more complex lipid compositions in cellular environments.

Our previous MD simulations suggested that the β-sheet structure is essential to the formation of Aβ pores.[23], [25]–[27], [36], [37] Our current results further support the idea that pore formation and β-sheet formation are linked. Following previous studies, we suggest two possibilities: (i) The F19P mutation does not completely inhibit β-sheet formation and therefore fiber formation may be possible under specific environmental conditions. (ii) Aβ pore formation is not solely reliant on β-sheet formation and involves other mechanisms. Our preliminary AFM results show that F19P, when incubated at 37 °C in water for 72 h, forms fibers (Figure 3.3). Previous reports that did not observe fiber formation for the F19P were done under different experimental conditions.[17], [20] Furthermore, other studies suggested that a proline mutation[42] or an isostructural mutation[43] at the F19 position may kinetically delay but not prevent oligomer formation. This inconsistency promotes further study of the role of β-sheets in pore formation, such as through additional point mutations and oligomer studies including incubation times, pH conditions, and temperatures.

3.6 Conclusions

We report a structural study of two point mutations of Alzheimer's disease $A\beta_{1-42}$. The propensity of the F19P mutation to form channels was found to be similar to the wild type through AFM imaging in DOPC bilayer. MD simulations also predicted channel formation; however, with a collapsed or clogged pore for the two available solid state NMR-based $A\beta_{1-42}$ conformers. This is in agreement with previous electrophysiology studies, which report no ionic conductance by the F19P mutant. The proline substitution is a β-sheet breaker. This indicates a role for β-sheet in the Aβ pore, and argues for further studies of its contribution and conformation during channel formation. The degree to which the β-sheet was disrupted by this mutation is still unclear, and is likely to vary in the heterogeneous channel landscape. Due to the compromised structure and activity the F19 position and the β-sheet structure it may be a viable target for AD therapeutic development against pore conductance. Structurally, the F20C mutation was found to behave similarly to the wild type both in MD simulations and AFM imaging of pore formation.

3.7 Acknowledgements

I would like to acknowledge my co-authors from Chapter 3, which in full, is a reprint of the material as it appears in Biochemistry, 2012, Connelly L, Jang H, Arce FT, Ramachandran S, Kagan BL, Nussinov R, Lal R. LC completed all AFM work, and

drafted the manuscript. HJ completed all modeling and supplemented the manuscript. No authors had competing interests regarding the publication of this research. The dissertation author was the primary investigator and author of this paper.

This research was supported by the National Institutes of Health (National Institute on Aging AG028709 to R.L.). This project has been funded in whole or partially with Federal funds from the National Cancer Institute, National Institutes of Health, under contract number HHSN261200800001E. This research was supported (partially) by the Intramural Research Program of the NIH, National Cancer Institute, Center for Cancer Research. All simulations had been performed using the high-performance computational facilities of the Biowulf PC/Linux cluster at the National Institutes of Health, Bethesda, MD (http://biowulf.nih.gov).

3.8 References

[1] K. Blennow, M. J. de Leon, and H. Zetterberg, "Alzheimer's disease," *Lancet*, vol. 368, no. 9533, pp. 387–403, Jul. 2006.

[2] F. Chiti and C. M. Dobson, "Protein misfolding, functional amyloid, and human disease," *Annu. Rev. Biochem.*, vol. 75, pp. 333–366, 2006.

[3] F. T. Arce, H. Jang, S. Ramachandran, P. B. Landon, R. Nussinov, and R. Lal, "Polymorphism of amyloid beta peptide in different environments: implications for membrane insertion and pore formation," *Soft Matter*, vol. 7, pp. 5267–5273, May 2011.

[4] S. M. Butterfield and H. A. Lashuel, "Amyloidogenic protein-membrane interactions: mechanistic insight from model systems," *Angew. Chem. Int. Ed Engl.*, vol. 49, no. 33, pp. 5628–5654, Aug. 2010.

[5] J. D. Harper, C. M. Lieber, and P. T. Lansbury, "Atomic force microscopic imaging of seeded fibril formation and fibril branching by the Alzheimer's disease amyloid-beta protein," *Chem Biol*, vol. 4, pp. 951–9, Dec. 1997.

[6] C. Ionescu-Zanetti, R. Khurana, J. R. Gillespie, J. S. Petrick, L. C. Trabachino, L. J. Minert, S. A. Carter, and A. L. Fink, "Monitoring the assembly of Ig light-chain amyloid fibrils by atomic force microscopy," *Proc Natl Acad Sci U A*, vol. 96, pp. 13175–9, Nov. 1999.

[7] J. D. Sipe and A. S. Cohen, "Review: history of the amyloid fibril," *J. Struct. Biol.*, vol. 130, no. 2–3, pp. 88–98, Jun. 2000.

[8] S. L. Bernstein, N. F. Dupuis, N. D. Lazo, T. Wyttenbach, M. M. Condron, G. Bitan, D. B. Teplow, J.-E. Shea, B. T. Ruotolo, C. V. Robinson, and M. T. Bowers, "Amyloid-β protein oligomerization and the importance of tetramers and dodecamers in the aetiology of Alzheimer's disease," *Nat. Chem.*, vol. 1, no. 4, pp. 326–331, Jul. 2009.

[9] A. Quist, "Amyloid ion channels: A common structural link for protein-misfolding disease," *Proc. Natl. Acad. Sci.*, vol. 102, pp. 10427–10432, 2005.

[10] C. G. Glabe, "Structural classification of toxic amyloid oligomers," *J. Biol. Chem.*, vol. 283, no. 44, pp. 29639–29643, Oct. 2008.

[11] A. Demuro, M. Smith, and I. Parker, "Single-channel Ca(2+) imaging implicates Abeta1-42 amyloid pores in Alzheimer's disease pathology," *J Cell Biol*, vol. 195, pp. 515–24, Oct. 2011.

[12] H. Lin, R. Bhatia, and R. Lal, "Amyloid beta protein forms ion channels: implications for Alzheimer's disease pathophysiology," *FASEB J*, vol. 15, pp. 2433–44, Nov. 2001.

[13] H. A. Lashuel, D. Hartley, B. M. Petre, T. Walz, and P. T. Lansbury Jr, "Neurodegenerative disease: amyloid pores from pathogenic mutations," *Nature*, vol. 418, no. 6895, p. 291, Jul. 2002.

[14] N. A. Shirwany, D. Payette, J. Xie, and Q. Guo, "The amyloid beta ion channel hypothesis of Alzheimer's disease," *Neuropsychiatr. Dis. Treat.*, vol. 3, no. 5, pp. 597–612, 2007.

[15] L. L. Iversen, R. J. Mortishire-Smith, S. J. Pollack, and M. S. Shearman, "The toxicity in vitro of beta-amyloid protein," *Biochem. J.*, vol. 311 (Pt 1), pp. 1–16, Oct. 1995.

[16] N. S. de Groot, F. X. Aviles, J. Vendrell, and S. Ventura, "Mutagenesis of the central hydrophobic cluster in Abeta42 Alzheimer's peptide. Side-chain properties correlate with aggregation propensities," *FEBS J.*, vol. 273, no. 3, pp. 658–668, Feb. 2006.

[17] S. J. Wood, R. Wetzel, J. D. Martin, and M. R. Hurle, "Prolines and amyloidogenicity in fragments of the Alzheimer's peptide beta/A4," *Biochemistry (Mosc.)*, vol. 34, no. 3, pp. 724–730, Jan. 1995.

[18] A. D. Williams, E. Portelius, I. Kheterpal, J. Guo, K. D. Cook, Y. Xu, and R. Wetzel, "Mapping abeta amyloid fibril secondary structure using scanning proline mutagenesis," *J. Mol. Biol.*, vol. 335, no. 3, pp. 833–842, Jan. 2004.

[19] D. M. Walsh, A. Lomakin, G. B. Benedek, M. M. Condron, and D. B. Teplow, "Amyloid beta-protein fibrillogenesis. Detection of a protofibrillar intermediate," *J. Biol. Chem.*, vol. 272, no. 35, pp. 22364–22372, Aug. 1997.

[20] S. L. Bernstein, T. Wyttenbach, A. Baumketner, J.-E. Shea, G. Bitan, D. B. Teplow, and M. T. Bowers, "Amyloid beta-protein: monomer structure and early aggregation states of Abeta42 and its Pro19 alloform," *J. Am. Chem. Soc.*, vol. 127, no. 7, pp. 2075–2084, Feb. 2005.

[21] S. R. Durell, B. R. Brooks, and A. Ben-Naim, "Solvent-Induced Forces between Two Hydrophilic Groups," *J. Phys. Chem.*, vol. 98, pp. 2198–2202, Feb. 1994.

[22] N. Arispe, "Architecture of the Alzheimer's A beta P ion channel pore," *J. Membr. Biol.*, vol. 197, no. 1, pp. 33–48, Jan. 2004.

[23] H. Jang, J. Zheng, R. Lal, and R. Nussinov, "New structures help the modeling of toxic amyloidß ion channels," *Trends Biochem. Sci.*, vol. 33, pp. 91–100, 2008.

[24] S. Shivaprasad and R. Wetzel, "Analysis of amyloid fibril structure by scanning cysteine mutagenesis," *Methods Enzymol.*, vol. 413, pp. 182–198, 2006.

[25] H. Jang, F. T. Arce, S. Ramachandran, R. Capone, R. Azimova, B. L. Kagan, R. Nussinov, and R. Lal, "Truncated -amyloid peptide channels provide an alternative mechanism for Alzheimer's Disease and Down syndrome," *Proc. Natl. Acad. Sci.*, vol. 107, pp. 6538–6543, 2010.

[26] H. Jang, F. T. Arce, S. Ramachandran, R. Capone, R. Lal, and R. Nussinov, "β-Barrel Topology of Alzheimer's β-Amyloid Ion Channels," *J. Mol. Biol.*, vol. 404, pp. 917–934, 2010.

[27] H. Jang, J. Zheng, and R. Nussinov, "Models of β-Amyloid Ion Channels in the Membrane Suggest That Channel Formation in the Bilayer Is a Dynamic Process," *Biophys. J.*, vol. 93, pp. 1938–1949, 2007.

[28] R. Capone, H. Jang, S. A. Kotler, B. L. Kagan, R. Nussinov, and R. Lal, "Probing structural features of Alzheimer's amyloid-β pores in bilayers using site-specific amino acid substitutions," *Biochemistry (Mosc.)*, vol. 51, no. 3, pp. 776–785, Jan. 2012.

[29] T. Luhrs, C. Ritter, M. Adrian, D. Riek-Loher, B. Bohrmann, H. Dobeli, D. Schubert, and R. Riek, "3D structure of Alzheimer's amyloid-beta(1-42) fibrils," *Proc Natl Acad Sci U A*, vol. 102, pp. 17342–7, Nov. 2005.

[30] A. T. Petkova, W. M. Yau, and R. Tycko, "Experimental constraints on quaternary structure in Alzheimer's beta-amyloid fibrils," *Biochemistry (Mosc.)*, vol. 45, pp. 498–512, Jan. 2006.

[31] S. Zirah, S. A. Kozin, A. K. Mazur, A. Blond, M. Cheminant, I. Segalas-Milazzo, P. Debey, and S. Rebuffat, "Structural changes of region 1-16 of the Alzheimer disease amyloid beta-peptide upon zinc binding and in vitro aging," *J Biol Chem*, vol. 281, pp. 2151–61, Jan. 2006.

[32] R. Capone, H. Jang, S. A. Kotler, L. Connelly, F. Teran Arce, S. Ramachandran, B. L. Kagan, R. Nussinov, and R. Lal, "All-d-Enantiomer of beta-Amyloid Peptide Forms Ion Channels in Lipid Bilayers," *J Chem Theory Comput*, vol. 8, pp. 1143–1152, Mar. 2012.

[33] L. Connelly, H. Jang, F. T. Arce, R. Capone, S. A. Kotler, S. Ramachandran, B. L. Kagan, R. Nussinov, and R. Lal, "Atomic force microscopy and MD simulations reveal pore-like structures of all-D-enantiomer of Alzheimer's β-amyloid peptide: relevance to the ion channel mechanism of AD pathology," *J. Phys. Chem. B*, vol. 116, no. 5, pp. 1728–1735, Feb. 2012.

[34] B. R. Brooks, R. E. Bruccoleri, B. D. Olafson, D. J. States, S. Swaminathan, and M. Karplus, "CHARMM: A program for macromolecular energy, minimization, and dynamics calculations," *J. Comput. Chem.*, vol. 4, pp. 187–217, 1983.

[35] J. C. Phillips, R. Braun, W. Wang, J. Gumbart, E. Tajkhorshid, E. Villa, C. Chipot, R. D. Skeel, L. Kalé, and K. Schulten, "Scalable molecular dynamics with NAMD," *J. Comput. Chem.*, vol. 26, pp. 1781–1802, 2005.

[36] H. Jang, F. T. Arce, R. Capone, S. Ramachandran, R. Lal, and R. Nussinov, "Misfolded Amyloid Ion Channels Present Mobile β-Sheet Subunits in Contrast to Conventional Ion Channels," *Biophys. J.*, vol. 97, pp. 3029–3037, 2009.

[37] H. Jang, F. Teran Arce, S. Ramachandran, R. Capone, R. Lal, and R. Nussinov, “Structural Convergence Among Diverse, Toxic Œ≤-Sheet Ion Channels,” *J. Phys. Chem. B*, vol. 114, pp. 9445–9451, Jul. 2010.

[38] O. S. Smart, J. M. Goodfellow, and B. A. Wallace, “The pore dimensions of gramicidin A,” *Biophys J*, vol. 65, pp. 2455–60, Dec. 1993.

[39] D. J. Selkoe, “Folding proteins in fatal ways,” *Nature*, vol. 426, pp. 900–4, Dec. 2003.

[40] C. M. Dobson, “Protein folding and misfolding,” *Nature*, vol. 426, pp. 884–90, Dec. 2003.

[41] A. Roher, D. Wolfe, M. Palutke, and D. KuKuruga, “Purification, ultrastructure, and chemical analysis of Alzheimer disease amyloid plaque core protein,” *Proc. Natl. Acad. Sci. U. S. A.*, vol. 83, no. 8, pp. 2662–2666, Apr. 1986.

[42] M. J. Cannon, A. D. Williams, R. Wetzel, and D. G. Myszka, “Kinetic analysis of beta-amyloid fibril elongation,” *Anal. Biochem.*, vol. 328, no. 1, pp. 67–75, May 2004.

[43] J. Bieschke, S. J. Siegel, Y. Fu, and J. W. Kelly, “Alzheimer’s Abeta peptides containing an isostructural backbone mutation afford distinct aggregate morphologies but analogous cytotoxicity. Evidence for a common low-abundance toxic structure(s)?,” *Biochemistry (Mosc.)*, vol. 47, no. 1, pp. 50–59, Jan. 2008.

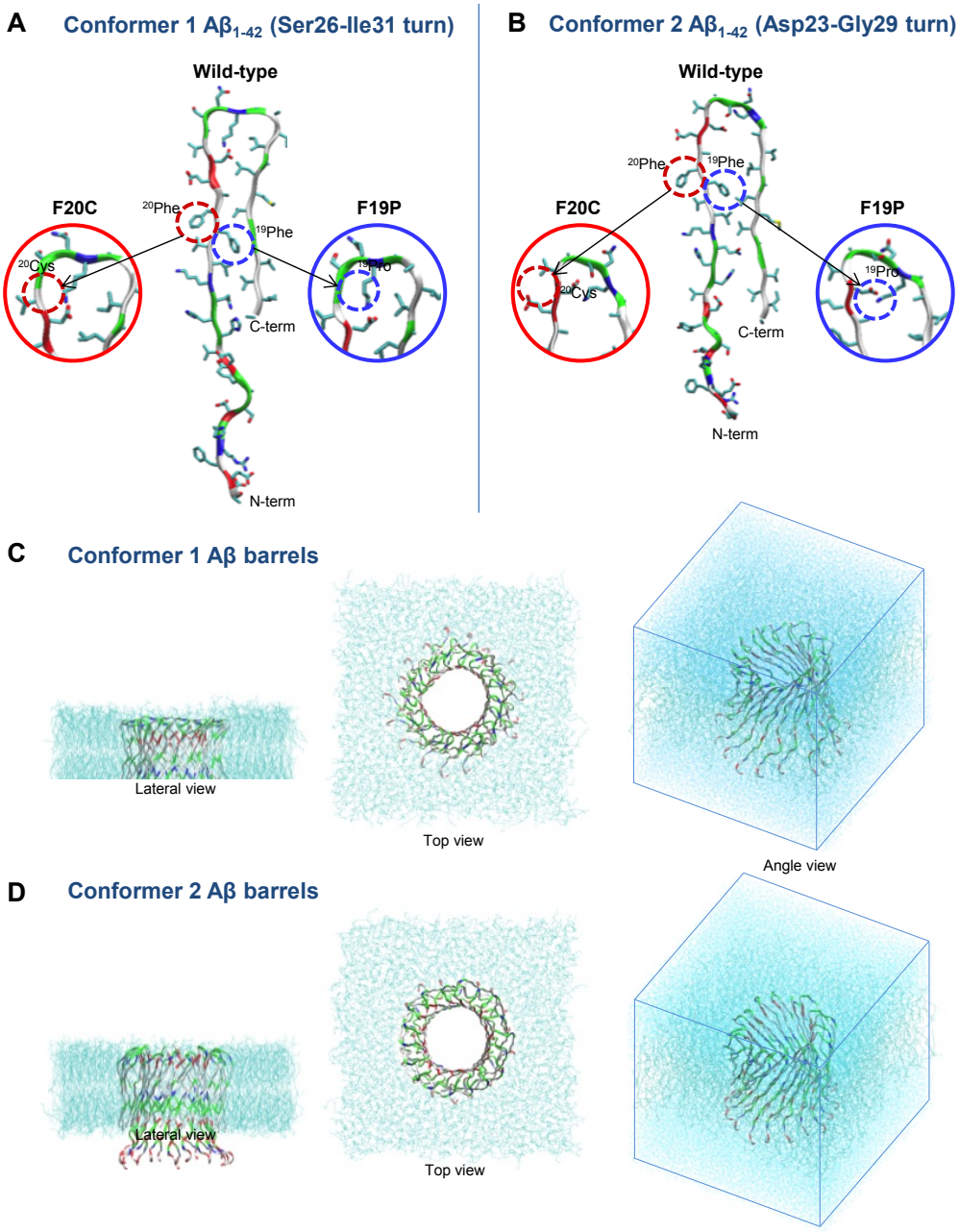

Figure 3.1 Monomer conformations of Aβ1-42 wild-type, F19P and F20C mutants with different turns at (A) Ser26-Ile31 (conformer 1) and (B) Asp23-Gly29 (conformer 2). Starting points of the Aβ1-42 barrels embedded in the lipid bilayer for the MD simulations for (C) conformer 1 and (D) conformer 2 Aβ1-42 barrels. Waters are removed for clarity in lateral and top views, but they are denoted as cyan dots in simulation box in angle view. In the peptide ribbon, hydrophobic residues are shown in white, polar and Gly residues are shown in green, positively charged residues are shown in blue, and negatively charged residues are shown in red.

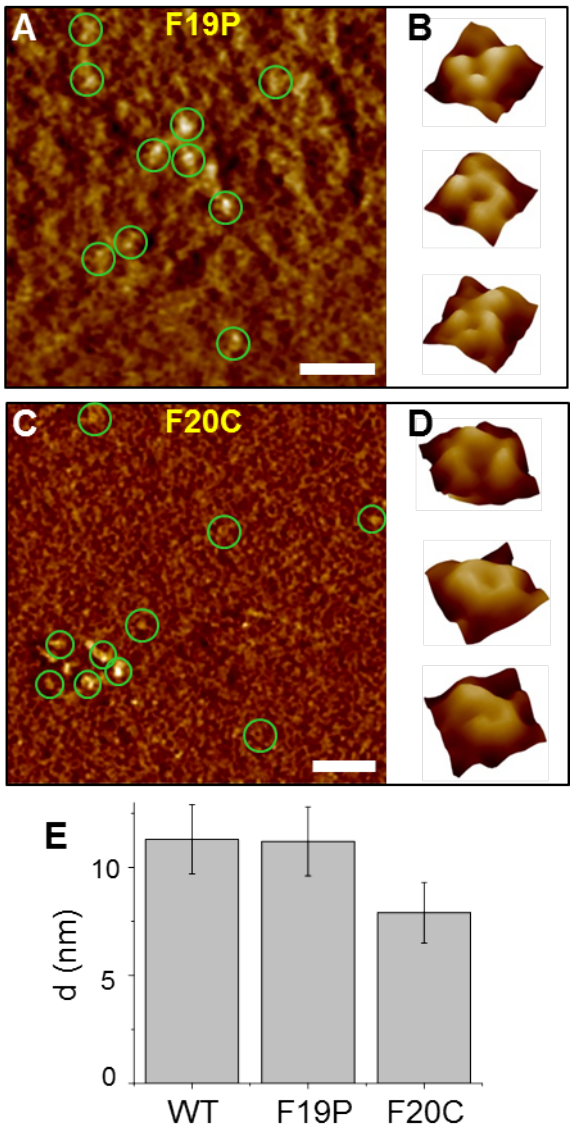

Figure 3.2 Amplitude AFM images of (A) F19P and (C) F20C mutants of Aβ1-42 incorporated in DOPC bilayers on mica. Pores with a central dip were resolved in both processed, and unprocessed amplitude and height images correlate with height increases in the height image (Figure S1, Supporting Information). (B) and (D) Individual pores from the amplitude images were selected and resolved into multimeric structures: trimers, tetramers, and pentamers. The pores appear characteristic of the wild type Aβ1-42 and, as a surface structure image, do not exhibit any indication of a compromised pore structure. A Gaussian low pass of 4 nm once in the x-direction and once in the y-direction was applied to (A-D) for noise removal. Lateral scale bars are 50 nm for (A) and (C). The height color scale is 7 nm in (A) and 5 nm in (C). Image sizes in (B) are: 17.46, 13.15, and 14.54 nm. Image sizes in (D) are: 14.00, 11.02, 12.5 nm. (E) Histograms for the average outer pore diameters, d, for the wild type Aβ1-42, (n = 16) and its F19P (n = 16) and F20C (n = 16) mutants.

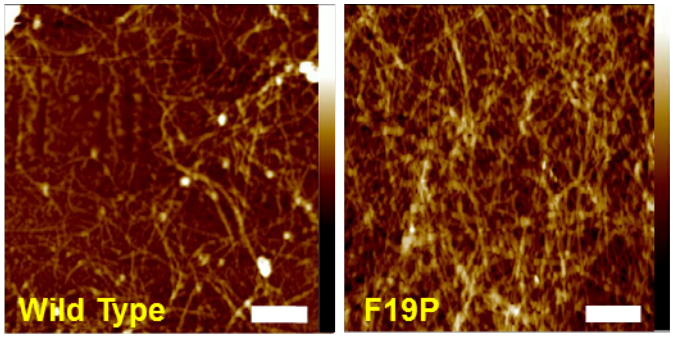

Figure 3.3 AFM height images of (A) wild type Aβ1-42 and (B) F19P mutant. Both peptides were incubated in H2O for 72 h at 37 °C and dried on fresh mica surface and imaged in air. Similar fiber formation is seen for both peptides as a variety of sizes is clearly observed. Scale bars are 500 nm and color scale bars are 50 nm.

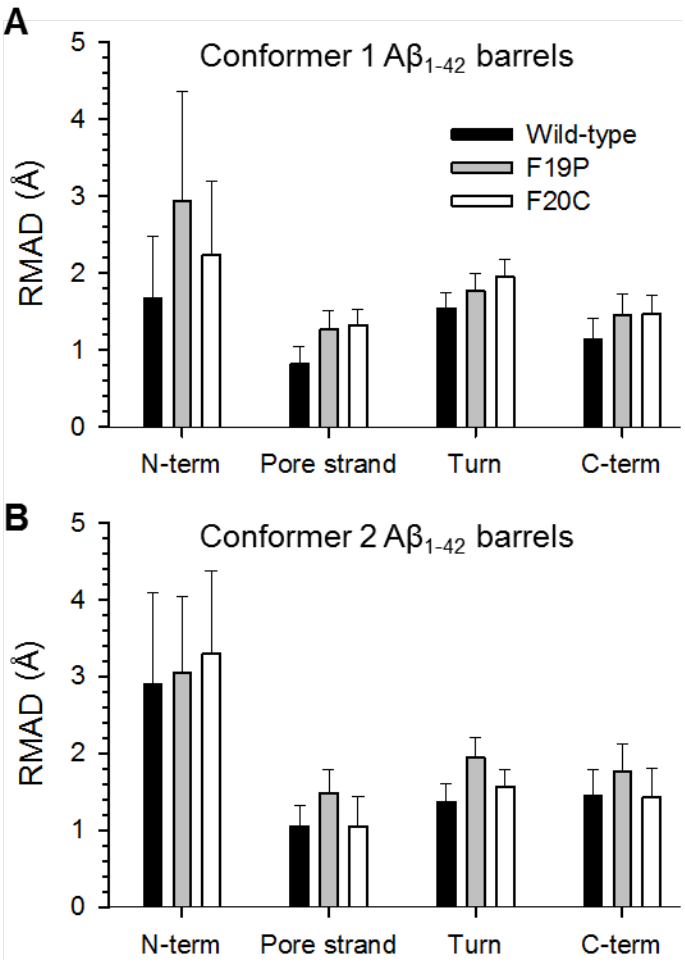

Figure 3.4 Averaged root-mean-squared deviation, RMSD, from the starting point for Cα atoms of the peptides for the (A) conformer 1 and (B) 2 Aβ1-42 barrels. The RMSD was calculated separately for the peptides in the barrels by dividing into four domains; N-terminal chain, pore-lining β-stand, turn, and C-terminal β-stand.

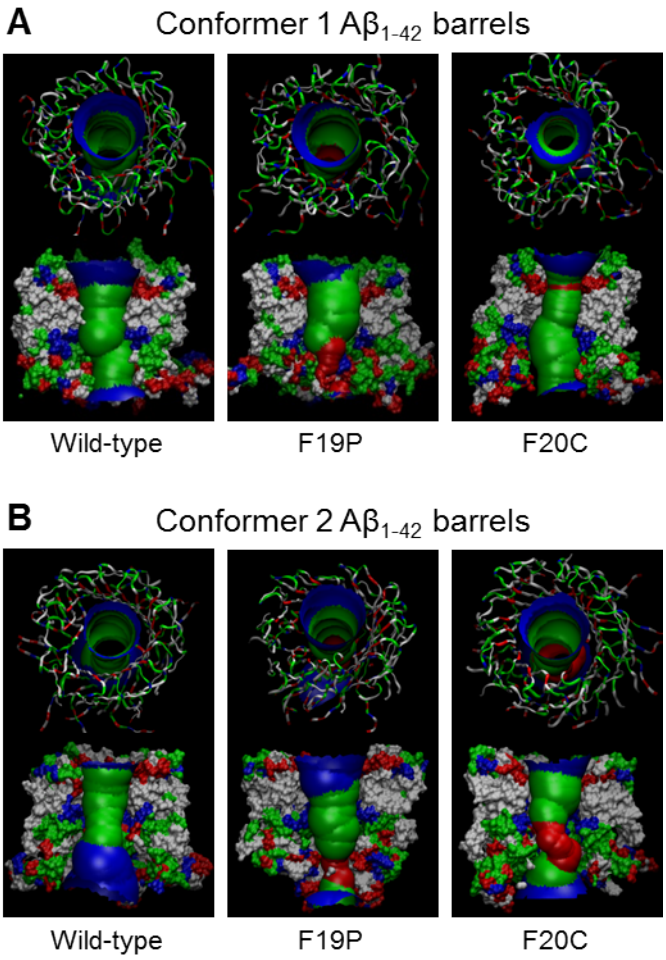

Figure 3.5 Averaged pore structures calculated by the HOLE program38 embedded in the averaged barrel conformations during the simulations for the (A) conformer 1 and (B) 2 $A\beta_{1\text{-}42}$ barrels. In the angle views of the pore structure (upper cartoons in each panel), whole barrel structures are shown with the ribbon representation. In the lateral views of the pore structure (lower cartoons in each panel), cross-sectioned barrels are given in the surface representation. In the peptide, hydrophobic residues are shown in white, polar and Gly residues are shown in green, positively charged residues are shown in blue, and negatively charged residues are shown in red.

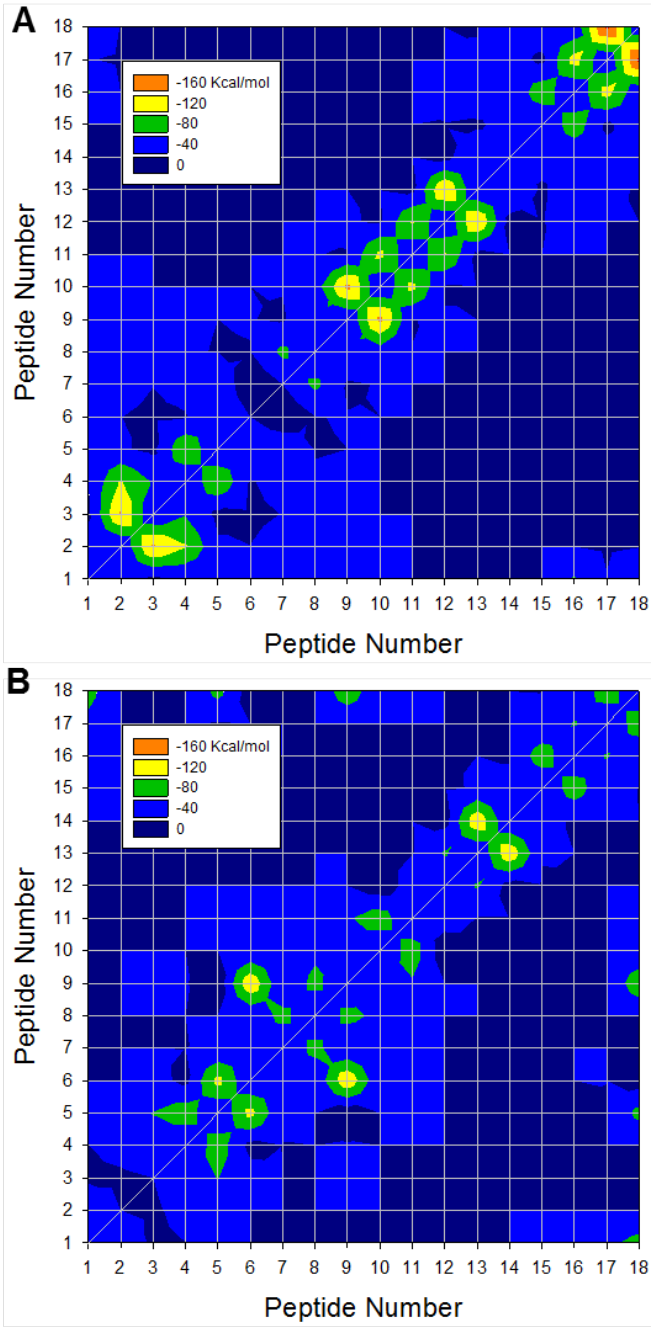

Figure 3.6 A contour map representing N-terminal/N-terminal chains interaction energy for the conformer 1 (A) Aβ1-42 wild type barrel and (B) F19P mutant barrel.

Table 3.1 The calculated outer and pore dimensions with a description of the pore status for the conformer 1 and 2 Aβ1-42 barrels composed of wild type peptide, and F19P and F20C mutants.

	Conformer 1 $A\beta_{1-42}$ barrel			Conformer 2 $A\beta_{1-42}$ barrel		
	Wild type	F19P	F20C	Wild type	F19P	F20C
Outer diameter (nm)	~8.2	~7.7	~7.9	~8.1	~7.6	~8.1
Pore height (nm)	~4.1	~5.6	~5.2	~4.5	~5.9	~5.3
Pore diameter* (nm)	~1.8	~1.5	~1.7	~1.9	~1.7	~1.7
Pore status	Opened	Clogged up	Opened	Opened	Collapsed	Partially collapsed

* Pore diameters are averaged along the pore axis within the cutoffs defined by the height of pore.

CHAPTER 4

Clinical Perspectives

4.1 Abstract

The current paradigm in the amyloid hypothesis brands small oligomers of β-amyloid (Aβ) as the toxic species in Alzheimer's disease (AD). These oligomers are fibril-like; contain β-sheet structure, and present an exposed hydrophobic surface. Oligomers with this motif are capable of penetrating the cell membrane, gathering to form toxic ion channels. Preliminary results are presented on utilizing brain derived Aβ and pharmacological channel blockers to further understand the toxicity of Aβ ion channels. Synthetic Aβ is highly purified and homogeneous. However, brain derived Aβ is exposed to diverse environments through its lifetime and may have slight structural differences from synthetic Aβ. Here, the structure of brain derived and synthetic Aβ are compared in AFM images of globular species and fibrils. Pharmacologic blockers are being developed to disrupt the formation of toxic Aβ ion channels. Preliminary results show lipid bilayers incorporated with the Anle138b channel blocker appear structurally indistinguishable from normal bilayers. Aβ oligomers were incorporated into bilayers containing anle138b. AFM images show protrusions from the bilayer with and without anle138b channel blocker. It appears Aβ inserts into the bilayer as normal in the presence of anle138b and any observed loss in channel activity is likely due to effects of the

compound within the bilayer leaflet. Finally, a brief overview of therapeutic development for Aβ ion channels and an argument for a combination of drugs, targeting oligomers on, and in, the membrane is presented.

4.2 Brain Derived β-Amyloid

4.2.1 Background

Proteins are responsible for carrying out and controlling many functions in living systems. The intricate and unique structure of a protein determines its function. Even, minute differences in structure can cause a healthy protein to have fatal consequences.[1] β-Amyloid (Aβ), a misfolded protein associated with Alzheimer's disease (AD), is known to exist as several length variations (36-43) and many aggregated states from monomers to fibrils. The function and therefore the structure of Aβ has been linked to the pathology of AD.[2]–[7] Synthetic peptides offers easy access to large quantities of high quality (known purity), that ensures consistent sample preparation and reliable characterization. In addition, protein engineering techniques enable point substitutions to mimic biological mutations to study them in detail. Studies using synthetic Aβ *in vivo* and *in vitro* has led to a wealth of knowledge on the structure and activity of Aβ.[8]–[17] An alternative to synthetic Aβ, brain derived Aβ has been extracted from cells or tissue for examination.[18]–[23] Although synthetic peptides have yielded pivotal information

in AD research, the findings from synthetic Aβ must be confirmed with brain derived Aβ to fully characterize the true function of Aβ in AD.[8], [18]

Due to the slow turnover of the Aβ in the diseased brain, they are subjected to post-modifications such as oxidation, glycosylation, glycation, truncation, deamidation, phosphorylation, methylation, oligomerization, etc., associations with non- Aβ species such as CLAC-P, ApoE in the plaques, or different folding and bonding within the peptide.[18] Therefore, research experiments with brain derived Aβ, may provide information more true to the biological function of Aβ that is otherwise not possible with synthetic peptides. Ideally, brain derived Aβ would be extracted and isolated by a procedure free of denaturing agents or detergents, thereby preserving the natural state of the peptide.[8]

Determining the authenticity of extracted brain derived Aβ has remained challenging. The degree of influence the extraction process has on the peptide's structural and chemical condition is undetermined. Additionally, samples of brain derived Aβ are not pure and therefore the concentration Aβ is often unknown. However, the validity of brain derived Aβ experiments may be supported by behavioral similarities with synthetic Aβ. Presented here, are AFM images of brain derived Aβ as obtained from the Masliah Group at UCSD. It is shown that brain derived Aβ, as received, contains monomers and oligomers. In spite of detergent treatment during the extraction process, these monomers and oligomers aggregate to form fibrils similar to synthetic Aβ, upon incubation. The similarity in kinetic behavior of the brain derived Aβ with their synthetic form, suggests the extraction process does not functionally change the peptide. Therefore this brain derived Aβ may serve as a valuable tool for other brain derived Aβ investigations.

4.2.2 Materials

We obtained brain derived Aβ in the particulate form. The extraction and processing of this particulate is detailed elsewhere (Pham et al., 2010) and was performed in Dr. Masliah lab at UCSD. Briefly, the particulate membrane fraction of a moderate to advanced AD case was homogenized in Buffer A: NaCl/P_i, 0.32 M sucrose, 50 mm HEPES, 25 mm $MgCl_2$, 0.5 mm dithiothreitol, 200 μg/mL phenylmethanesulfonyl fluoride, 2 μg/mL pepstatin A, 4 μg/mL leupeptin, and 30μg/mL benzamidine, pH 7.4) and fractionated at 100,000 *g* for 1 h. Only the particulate fraction for the oligomer pull down was used because Aβ monomer and its oligomers are most concentrated in the fraction. The elute primarily contained Aβ monomers, oligomers and 82E1 antibody in a solution containing 130 mM Tris, 4.6 % SDS, 2 % DTT, and 10 % glycerol (pH 8.0). The sample also contains many unknown proteins. A negative control from a pull down with normal mouse IgG was also obtained for comparison.

4.2.3 Results and Discussion

Aliquots of the brain derived Aβ and the negative control were diluted in factors of 10 in PBS (without Ca or Mg), deposited on fresh mica, and allowed to dry in air at RT. Each sample was then imaged using atomic force microscopy in air to characterize each species (Fig. 4.1). The fraction containing Aβ monomers and oligomers shows circular deposits of varying sizes. In Fig. 4.1 A, larger deposits are 4-10 nm in height as

indicated with black arrows and smaller deposits exhibit ~1 nm height as indicated with white arrows. The negative control shows deposits of IgG material at a uniform height of ~1 nm that occurs as a uniform residue on the mica surface (Fig. 4.1 B). The oligomeric structures seen in Fig 4.1 are absent in the negative control and therefore distinctly different. A control mica sample of dried PBS was also imaged, and as expected appears clear of the features observed in Fig 4.1 A and B (Fig. 4.1C). Any features present in the Fig.4.1C may be due to small amounts of contamination.

The spherical bodies observed in Fig. 4.1A are similar to previously reported AFM images of synthetic Aβ. Small synthetic globules have been reported with heights of 1-3 nm and 8-10 nm for larger globules.[24]–[27] Although it is not possible to distinguish Aβ from other proteins in these images it is noted that no fibers were seen in the Aβ sample. Therefore, this procedure is a reliable means for extracting natural monomeric and oligomeric Aβ that, while contaminated with other proteins, is free of the fibrillar forms.

Aliquots of the brain derived Aβ particulate were incubated at 37 °C as received and dilutions imaged at 40 h and 4 days. Samples at each time point were deposited on fresh mica, rinsed to remove remaining salt contents, and dried with N_2 gas. AFM imaging was done in air and shown in Fig 4.2 A, B. Fibers appear to have formed at both time points and circular protofibrils, characteristic of amyloid formation, are visible for the shorter incubation time. Fiber formation is characteristic of all amyloids including brain derived Aβ prior to extraction and synthetic Aβ[25]–[29](Fig. 4.2 C). This fiber formation supports functional Aβ composing a high percentage of the monomers and oligomers observed in Fig 4.1A, regardless the potentially degrading detergent treatment

used during extraction. High resistance to degradation is an important characteristic of amyloidogenic proteins.[30] Fiber formation kinetics are highly dependent on many factors such as concentration, incubation time, purity, and pH which may contribute to size and shape differences between the natural and synthetic Aβ.[31]

AFM images of the brain derived Aβ shows comparable sizes of monomers, oligomers, and fibrils to synthetic Aβ.[24]–[28] This is a first step in the pursuit of more elaborate structural studies of brain derived Aβ. Access to oligomeric forms of Aβ is crucial for ion channel activity and structure studies of the brain derived species. Electrophysiology and AFM are the two most prominent techniques used to study the activity and structure of individual Aβ ion channels. Brain derived Aβ channels have not been successfully imaged via AFM *in vivo* due to resolution limitations and the inability to be differentiated from other membrane proteins. Isolation of brain derived Aβ will enable its use in supported synthetic membranes. Such membrane studies were not pursued here because of high concentration of SDS in the sample, which destroys supported membranes. A modified extraction procedure without the use of detergents and selective isolation and purification of Aβ without other contaminating species is needed for better structural and functional characterization of brain derived Aβ peptides and is currently being pursued.

4.3 β-Amyloid Pore Structure in the Presence of a Pharmacologic Blocker

4.3.1 Background

It has been well established that ion channels, including toxic Aβ pores, can be visualized and studied through atomic force microscopy.[25], [32]–[34] Currently, pharmacologic blockers are being developed to disrupt the formation of toxic ion channels in AD as well as related neurodegenerative diseases.[35]–[38] A novel oligomer modulator, anle138b, was developed to target neurodegenerative diseases such as prion's, Parkinson's, and Alzheimer's disease (Fig 4.3).[35], [36] The selection of anle138b is described in depth elsewhere and was completed by Wagner et. al. and is published in Acta Neuropathology, 2013[36] and US Patent: 2011/0293520 A1.[35] Anle138b has shown to directly target pathological aggregation at the oligomeric level and inhibit the pore activity of α-syn. Aβ is similar to α-syn in that both peptides form extracellular deposits in diseased patients, are rich in β-sheet structures, form ion channels in the cell membrane, and are associated with neurodegenerative disease.[4], [15] Wagner et. al.[36] reports the anle138b compound functions by targeting structure dependent epitopes. Therefore, the similarity in structural features of α-syn and Aβ aggregation naturally leads to the application of anle138b to the pore formation of Aβ.

The anle138b compound is highly hydrophobic and insoluble in aqueous solutions. To observe the effect of anle138b on the pore structure of Aβ, the compound must be incorporated into the lipid bilayer. Here we present AFM analysis of lipid bilayers incorporated with the anle138b compound. We also incorporated $A\beta_{1-42}$ into lipid bilayers with and without the anle138b compound.

4.3.2 Materials and Methods

Peptide preparation: For dilution and storage of $A\beta_{1-42}$, (Anaspec Inc., Fremont, CA), 1.0 % NH_4OH was added to the lyophilized powder (35-40 µL to 0.5 mg peptide or 70-80 µL to 1 mg peptide). This solution was further diluted with 1x PBS to a final concentration of ~ 1mg/mL of peptide concentration. The peptide solution was aliquot into 50 µL volumes and stored at -20°C. Before use, peptide solutions were sonicated for about 5 min in a bath sonicator.

Compound incorporation to liposomes: Compound anle138b, in powder form, as obtained from the Griesinger group (Max Planck Institute for Physical Chemistry, Göttingen, Germany) was dissolved in chloroform. Anle138b was mixed with lipids (in chloroform) such that the final concentration of the compound would be 10-20 mM (by lipid volume) upon hydration of the lipid cake. The lipids/anle138b mixture was dried under vacuum in a rotovap or overnight in a desiccator. The resulting lipid cake was then hydrated with buffer or peptide (see below) to a lipid concentration of 1 mg/mL.

Peptide insertion in liposomes: (1) Liposome solutions were the first solution prepared. Phospholipid, 1,2-dioleoyl-sn-glycero-3-phosphocholine (DOPC) and 1,2-

dipalmitoyl-*sn*-glycero-3-phosphocholine (DPPC) were purchased from Avanti polar lipids (Alabaster, AL). DOPC was typically used (sometimes DOPC/DPPC mixtures, at 1:1 ratios) lipids in PBS at concentrations ranging from 0.1-1 mg/mL. For peptide insertion, the peptide solution was added to the liposome suspension in peptide/lipid ratios ranging from 1:100 - 1:10 (by mass) and sonicated for 5-10 minutes. The liposome suspensions were then extruded in 100 nm filters. *(2)* Alternatively, the peptide solution was added directly to the dried lipid cake during the lipid hydration process in the expectation that peptide insertion into the lipid bilayer would be more efficient. 1:10 peptide/lipid mass ratios were used. The mixture was vortexed for 30 minutes during hydration and further sonicated for 5 minutes before liposome extrusion using 100 nm filters.

4.3.3 Results and Discussion

The anle138b compound was incorporated into the lipid bilayer and imaged the bilayer with AFM (Fig. 4.4). Bilayers incorporated with anle138 appeared structurally indistinguishable from bilayers without the compound. Height differences within a single bilayer and a mica surface may vary by ~1.5 nm especially in contact mode. This variation is often due to the tip repeatedly scanning a surface area and gently compressing the lipid layers. Therefore the height differences Fig. 4.4 C and D between DPPC and DOPC are negligible. The height difference between the DPPC and mica is also not significant enough to be clearly attributed to the presence of anle138b. The bilayer/anle138b images (Fig. 4.4) serve as controls for the later imaging of

bilayer/anle138b with Aβ. The bilayers, free of peptide appear smooth. This similarity is supported by the previous report by Griesinger et. al. that anle138b functions by direct interaction with structural epitopes of peptides and not indirectly through changes to the lipid bilayer.[35] It is therefore reasonable that anle138b does not significantly disrupt the bilayer due to its small size, 343 D, which can easily fit between the bilayers.[35]

Preliminary results show Aβ in lipid bilayers with and without the anle138b compound (Fig. 4.5). Both bilayers with and without anle138b show indications of oligomeric Aβ embedded in the bilayers (red arrows). Smaller protrusions are observed in both bilayers suggesting the possible presence of pore structures (green arrows). Higher resolution images of bilayers were not obtained for these samples due to instabilities. Electrophysiology studies of Aβ pore activity in the presence of anle138b have shown that it is effective in decreasing and eventually preventing pore activity (unpublished data Greisinger et. al). Although Fig. 4.5 suggests pore structures may be present it is possible that the anle138b compound compromises the inner pore channel, inhibits complete pore formation, or collapses pores preventing activity.

The images suggest Aβ inserts into the lipid bilayer and therefore that any activity inhibition observed in the presence of anle138b is due to peptide-compound interaction, not an artifact of Aβ failing to insert into the bilayer. It is also notable that no fibrils are observed in either bilayer. Higher resolution images of Aβ in bilayers with anle138b are necessary to fully evaluate the presence of pores, oligomers, or other Aβ structures. Such structural patterns may include inner and outer diameters and number of subunits. Finer structural details may indicate the exact changes to the pores that occur in the presence of anle138b and are currently being pursued. In conclusion, we have shown that anle138b

can be incorporated into supported lipid bilayers and are indistinguishable from lipid bilayers without it. Aβ inserts into lipid bilayers and may form pore like structures in the presence of anle138b. Thus, an effect of the compound on the pore activity may be due to a structural change within the pore lining or inner pore bilayer interface but more extensive analysis is necessary.

4.4 Therapeutic Development Recommendations

4.4.1 Introduction

The shift of the amyloid cascade hypothesis gradually toward the focus of amyloid toxicity of smaller oligomers[39] has prompted us to reexamine AD pathology and drug discovery. The ion channel hypothesis,[6] and its further validation[40] have long argued that toxicity is mediated by channel formations. Due to the unfavorable chemistry and high energetic cost of complete preformed channels sliding into the membrane, we have previously suggested[41] that Aβ oligomers can irreversibly insert into a membrane and spontaneously form an ion channel, leading to cell death. While the channels can be blocked by drugs,[42] their broad conformational heterogeneity leads us to suggest that Aβ directed therapeutics should consider a combination therapy that targets the toxic Aβ oligomers on the membrane before they are inserted, and, in parallel, targets the oligomers that have already penetrated into the membrane, where these agents could prevent toxic channel formations. While this suggestion currently presents a

daunting challenge, the development of therapeutic agents to target already formed toxic channels is further hampered by the channels' highly polymorphic nature, encompassing different sizes, shapes, and chemistries, suggesting that a "one size fits all" blocker may, or may not work. A combination therapy has important implications for the development and the clinical trials of new therapeutic drugs in the pathogenesis of AD. The free energy landscapes of Aβ monomers, oligomers, and membrane-embedded oligomers and channels are all highly polymorphic,[43], [44] emphasizing the hurdles facing drug development, and pointing to the need to rethink drug strategies. Such Aβ-direct 'attacks' are in addition to a focus on the complex cellular network controlling and mediating Aβ expression and processing. We believe that it is unlikely that a single, universal, approach will suppress all Aβ-related pathologies.

4.4.2 Tentative therapeutic targets/agents

4.4.2.1 Fibril-like Aβ oligomers

Wu et al.[45] reported that small soluble Aβ oligomers, known as fibrillar oligomers (FOs), contained 3-10 Aβ monomers and exhibited fibril-like morphology rich in β-sheet structure. They noted that FOs could increase toxicity, since the oligomers were able to replicate and expose the hydrophobic sheet surfaces. It has been suggested that a more toxic Aβ oligomer has a solvent exposed hydrophobic face, while a less toxic Aβ oligomer is deficient in β-sheet conformation.[46] Using ssNMR and EM, it was observed that the small fibril-like Aβ oligomer intermediates have predominantly parallel

β-sheet structures.[47] A recent MD study demonstrated that parallel β-sheet Aβ oligomers with the U-shaped peptide motif were capable of penetrating the membrane.[41] Taken together, it is not surprising that fibril-like oligomers with exposed hydrophobic surface are cytotoxic, since they spontaneously insert into the membranes and several of these gather to form toxic ion channels. Thus, drugs aimed at inhibiting the production of these oligomers, or inhibitors preventing the oligomers attachment to the membranes would attenuate the Aβ toxicity, indicating that the fibril-like β-sheet oligomers would be tentative therapeutic targets in AD.

4.4.2.2 Ion channel blockers

The amyloid hypothesis of AD implicated the toxic ion channel formation in membranes on the basis of large body of experimental and computational observations.[6], [7], [15], [25], [33], [48]–[60] Ion channel blockers were thought to be intuitive therapeutic agents that lead to blockage of conducting pores. Diaz et al.[42] introduced two small molecular blockers of Aβ channel: MRS2481 and an enatiomeric species, MRS2485. While both blockers could potentially protect neurons from Aβ toxicity, MRS2485 was found to be virtually irreversible in the channel inhibition. Developing pharmacologic inhibitors with high specificity aimed to block the pore would be a major challenge,[61] since structural modeling of Aβ channels has suggested that channels are mobile and flexible in the lipid bilayers, with varying sizes and shapes.[53], [55], [56] Amyloid channels are highly polymorphic, suggesting that “one size fits all” blockers may not be effective in comprehensive treatment of amyloid channels. Indirect

strategies to inhibit Aβ channel activity prompted development of drugs that can control existing channels. Liu et al.[62] introduced a drug, known as diazoxide, a potassium ATP channel activator. They demonstrated that diazoxide improved memory and reduced Aβ and tau pathology in a transgenic AD mouse model. Since Aβ channels tend to lower the membrane potential due to their relative lack of selectivity, membrane hyperpolarization by the potassium opener can suppress the depolarizing effect of the Aβ channel. A similar approach also demonstrated that voltage-gated calcium channel blockers, such as verapamil, diltiazem, isradipine and nimodipine, exerted protective effects on cultured neurons from Aβ toxicity.[63] Thus, drugs that hyperpolarize membranes would be possible therapeutic agents in AD.

4.4.2.3 Point mutations

Naturally occurring point mutations of Aβ clustered at residues 22 and 23 were related to familial forms of AD.[64] These Aβ mutations were found in fibrillar aggregates on a membrane[65] and related to cerebral amyloid angiopathy (CAA) and presenile dementia.[66], [67] Unlike the disease-related Aβ mutants, proline mutation in the central region of Aβ recently demonstrated that substitution of Phe19 with Pro (F19P) in both truncated Aβ17−42 (p3) and full length Aβ1−42 channels could prevent bilayer channel activity and cellular toxicity.[54], [58], [60] Proline, known as β-sheet breaker, destabilized pore-lining β-strands based on the computational models, producing kinks at the locations of Pro19. As a result, Aβ channels formed with collapsed pores consequently inhibited ions crossing through the pore (Fig. 7). This indicates that the

mutant exhibits no toxic oligomer, and hence no active functioning ion channel in the membrane. Function compromising residues of ion channels, such as Phe19, may serve as potential targets in the drug development

4.4.3 Conclusions

Current therapeutic drugs targeting Aβ peptides were designed to inhibit proteases in the process of APP cleavages. Such β- and γ- secretase inhibitors were aimed at reducing Aβ production.[68], [69] Yet the development of safe secretase inhibitor drugs is not promoted due to side effects; the enzymes have additional physiological substrates in the cell, most prominent among these is Notch which is cleaved by γ-secretase.[70] In the amyloid hypothesis, small oligomers gained interest as a toxic species.[71] Fibril-like oligomers rich in β structure were identified as active cytotoxic molecules, spontaneously inserting into the membrane and assembling to form toxic ion channels.[41], [45]–[47] The mechanisms of their membrane insertion/disruption are similar to those observed for antimicrobial peptides (AMPs).[41], [61] Therapeutic development efforts for amyloid-removing or disassembling agents have not been rewarded, to date largely failing in clinical trials. This failure of the current agents appears to at least partly stem from poor permeability of cell membranes. Toxic Aβ oligomers are irreversibly inserted into the cells and form channels in the cell membrane or (possibly) in the mitochondrial membrane in the cytoplasm.[72] Under such circumstances, therapeutic agents might be unable to penetrate the cell membrane to block or disassemble the channels inside the membrane and the cell. To compound the challenge, amyloid channels are as highly

polymorphic as amyloid fibrils. To date, an effective blocker is yet to be discovered. Here, we argue for a combination of drugs, targeting oligomers on, and in, the membrane. The properties of the drugs will need to differ, given the varied chemical environment, a solvated extracellular milieu and a lipidic bilayer. Combined, these drugs would prevent Aβ insertion into the membrane and act to retain a healthy membrane, preventing channel formation by already 'infected' membranes. The heterogeneity may call for drugs that recognize the prevailing conformational species. While here we focused on Aβ, similar strategies may be used in other amyloid species.

4.5 Acknowledgements

I would like to recognize my co-authors for Chapter 4. Section 4.4, which, in part, is a reprint of the material as it appears in Physical Chemistry Chemical Physics, 2013, Jang H, Connelly L, Arce FT, Ramachandran S, Lal R, Kagan BL, Nussinov R. The dissertation author was a shared investigator and author with Dr. Hyunbum Jang of this paper. I would like to thank Dr. Eliezer Masliah and Dr. Sarah Michael for providing the brain derived amyloid used in Section 4.2. I would like to thank Dr. Christian Griesinger for providing the anle138b compound in Section 4.3. The dissertation author was the primary author and investigator for this material.

4.6 References

[1] P. J. Thomas, B.-H. Qu, and P. L. Pedersen, "Defective protein folding as a basis of human disease," *Trends Biochem. Sci.*, vol. 20, no. 11, pp. 456–459, Nov. 1995.

[2] B. Caughey and P. T. Lansbury, "Protofibrils, pores, fibrils, and neurodegeneration: separating the responsible protein aggregates from the innocent bystanders," *Annu. Rev. Neurosci.*, vol. 26, pp. 267–298, 2003.

[3] D. B. Teplow, "Structural and kinetic features of amyloid beta-protein fibrillogenesis," *Amyloid Int. J. Exp. Clin. Investig. Off. J. Int. Soc. Amyloidosis*, vol. 5, no. 2, pp. 121–142, Jun. 1998.

[4] P. A. Temussi, L. Masino, and A. Pastore, "From Alzheimer to Huntington: why is a structural understanding so difficult?," *EMBO J*, vol. 22, pp. 355–61, Feb. 2003.

[5] J. Hardy and D. J. Selkoe, "The amyloid hypothesis of Alzheimer's disease: progress and problems on the road to therapeutics," *Science*, vol. 297, pp. 353–6, Jul. 2002.

[6] N. Arispe, E. Rojas, and H. B. Pollard, "Alzheimer disease amyloid beta protein forms calcium channels in bilayer membranes: blockade by tromethamine and aluminum," *Proc Natl Acad Sci U A*, vol. 90, pp. 567–71, Jan. 1993.

[7] N. Arispe, H. B. Pollard, and E. Rojas, "Giant multilevel cation channels formed by Alzheimer disease amyloid beta-protein [A beta P-(1-40)] in bilayer membranes," *Proc Natl Acad Sci U A*, vol. 90, pp. 10573–7, Nov. 1993.

[8] D. M. Walsh and D. J. Selkoe, "A beta oligomers - a decade of discovery," *J. Neurochem.*, vol. 101, no. 5, pp. 1172–1184, Jun. 2007.

[9] C. J. Pike, D. Burdick, A. J. Walencewicz, C. G. Glabe, and C. W. Cotman, "Neurodegeneration induced by beta-amyloid peptides in vitro: the role of peptide assembly state," *J. Neurosci.*, vol. 13, no. 4, pp. 1676–1687, Apr. 1993.

[10] J. D. Harper, S. S. Wong, C. M. Lieber, and P. T. Lansbury, "Observation of metastable Abeta amyloid protofibrils by atomic force microscopy," *Chem. Biol.*, vol. 4, no. 2, pp. 119–125, Feb. 1997.

[11] D. M. Hartley, D. M. Walsh, C. P. Ye, T. Diehl, S. Vasquez, P. M. Vassilev, D. B. Teplow, and D. J. Selkoe, "Protofibrillar intermediates of amyloid beta-protein induce acute electrophysiological changes and progressive neurotoxicity in cortical neurons," *J. Neurosci. Off. J. Soc. Neurosci.*, vol. 19, no. 20, pp. 8876–8884, Oct. 1999.

[12] D. M. Walsh, A. Lomakin, G. B. Benedek, M. M. Condron, and D. B. Teplow, "Amyloid beta-protein fibrillogenesis. Detection of a protofibrillar intermediate," *J. Biol. Chem.*, vol. 272, no. 35, pp. 22364–22372, Aug. 1997.

[13] D. M. Walsh, D. M. Hartley, Y. Kusumoto, Y. Fezoui, M. M. Condron, A. Lomakin, G. B. Benedek, D. J. Selkoe, and D. B. Teplow, "Amyloid beta-protein fibrillogenesis. Structure and biological activity of protofibrillar intermediates," *J. Biol. Chem.*, vol. 274, no. 36, pp. 25945–25952, Sep. 1999.

[14] G. Bitan, M. D. Kirkitadze, A. Lomakin, S. S. Vollers, G. B. Benedek, and D. B. Teplow, "Amyloid beta -protein (Abeta) assembly: Abeta 40 and Abeta 42 oligomerize through distinct pathways," *Proc. Natl. Acad. Sci. U. S. A.*, vol. 100, no. 1, pp. 330–335, Jan. 2003.

[15] H. A. Lashuel, D. Hartley, B. M. Petre, T. Walz, and P. T. Lansbury Jr, "Neurodegenerative disease: amyloid pores from pathogenic mutations," *Nature*, vol. 418, no. 6895, p. 291, Jul. 2002.

[16] M. P. Lambert, A. K. Barlow, B. A. Chromy, C. Edwards, R. Freed, M. Liosatos, T. E. Morgan, I. Rozovsky, B. Trommer, K. L. Viola, P. Wals, C. Zhang, C. E. Finch, G. A. Krafft, and W. L. Klein, "Diffusible, nonfibrillar ligands derived from Abeta1-42 are potent central nervous system neurotoxins," *Proc. Natl. Acad. Sci. U. S. A.*, vol. 95, no. 11, pp. 6448–6453, May 1998.

[17] Y. Gong, L. Chang, K. L. Viola, P. N. Lacor, M. P. Lambert, C. E. Finch, G. A. Krafft, and W. L. Klein, "Alzheimer's disease-affected brain: presence of oligomeric A beta ligands (ADDLs) suggests a molecular basis for reversible memory loss," *Proc. Natl. Acad. Sci. U. S. A.*, vol. 100, no. 18, pp. 10417–10422, Sep. 2003.

[18] D. M. Walsh, I. Klyubin, G. M. Shankar, M. Townsend, J. V. Fadeeva, V. Betts, M. B. Podlisny, J. P. Cleary, K. H. Ashe, M. J. Rowan, and D. J. Selkoe, "The role of cell-derived oligomers of Abeta in Alzheimer's disease and avenues for therapeutic intervention," *Biochem. Soc. Trans.*, vol. 33, no. Pt 5, pp. 1087–1090, Nov. 2005.

[19] E. Pham, L. Crews, K. Ubhi, L. Hansen, A. Adame, A. Cartier, D. Salmon, D. Galasko, S. Michael, J. N. Savas, J. R. Yates, C. Glabe, and E. Masliah, "Progressive accumulation of amyloid-beta oligomers in Alzheimer's disease and in amyloid precursor protein transgenic mice is accompanied by selective alterations in synaptic scaffold proteins," *FEBS J.*, vol. 277, no. 14, pp. 3051–3067, Jul. 2010.

[20] S. Lesné, M. T. Koh, L. Kotilinek, R. Kayed, C. G. Glabe, A. Yang, M. Gallagher, and K. H. Ashe, "A specific amyloid-beta protein assembly in the brain impairs memory," *Nature*, vol. 440, no. 7082, pp. 352–357, Mar. 2006.

[21] M. B. Podlisny, B. L. Ostaszewski, S. L. Squazzo, E. H. Koo, R. E. Rydell, D. B. Teplow, and D. J. Selkoe, "Aggregation of secreted amyloid beta-protein into sodium dodecyl sulfate-stable oligomers in cell culture," *J. Biol. Chem.*, vol. 270, no. 16, pp. 9564–9570, Apr. 1995.

[22] D. M. Walsh, B. P. Tseng, R. E. Rydel, M. B. Podlisny, and D. J. Selkoe, "The oligomerization of amyloid beta-protein begins intracellularly in cells derived from human brain," *Biochemistry (Mosc.)*, vol. 39, no. 35, pp. 10831–10839, Sep. 2000.

[23] D. M. Walsh, I. Klyubin, J. V. Fadeeva, W. K. Cullen, R. Anwyl, M. S. Wolfe, M. J. Rowan, and D. J. Selkoe, "Naturally secreted oligomers of amyloid beta protein potently inhibit hippocampal long-term potentiation in vivo," *Nature*, vol. 416, pp. 535–9, Apr. 2002.

[24] O. N. Antzutkin, "Amyloidosis of Alzheimer's Abeta peptides: solid-state nuclear magnetic resonance, electron paramagnetic resonance, transmission electron microscopy, scanning transmission electron microscopy and atomic force microscopy studies," *Magn Reson Chem*, vol. 42, pp. 231–46, Feb. 2004.

[25] H. Lin, R. Bhatia, and R. Lal, "Amyloid beta protein forms ion channels: implications for Alzheimer's disease pathophysiology," *FASEB J*, vol. 15, pp. 2433–44, Nov. 2001.

[26] H. Lin, Y. J. Zhu, and R. Lal, "Amyloid beta protein (1-40) forms calcium-permeable, Zn2+-sensitive channel in reconstituted lipid vesicles," *Biochemistry (Mosc.)*, vol. 38, no. 34, pp. 11189–11196, Aug. 1999.

[27] A. Parbhu, H. Lin, J. Thimm, and R. Lal, "Imaging real-time aggregation of amyloid beta protein (1-42) by atomic force microscopy," *Peptides*, vol. 23, no. 7, pp. 1265–1270, Jul. 2002.

[28] A. Relini, S. Torrassa, R. Ferrando, R. Rolandi, S. Campioni, F. Chiti, and A. Gliozzi, "Detection of Populations of Amyloid-Like Protofibrils with Different Physical Properties," *Biophys. J.*, vol. 98, no. 7, pp. 1277–1284, Apr. 2010.

[29] D. Burdick, B. Soreghan, M. Kwon, J. Kosmoski, M. Knauer, A. Henschen, J. Yates, C. Cotman, and C. Glabe, "Assembly and aggregation properties of synthetic Alzheimer's A4/beta amyloid peptide analogs.," *J. Biol. Chem.*, vol. 267, no. 1, pp. 546–554, Jan. 1992.

[30] I. Cherny and E. Gazit, "Amyloids: Not Only Pathological Agents but Also Ordered Nanomaterials," *Angew. Chem. Int. Ed.*, vol. 47, no. 22, pp. 4062–4069, 2008.

[31] M. D. Kirkitadze, M. M. Condron, and D. B. Teplow, "Identification and characterization of key kinetic intermediates in amyloid β-protein fibrillogenesis," *J. Mol. Biol.*, vol. 312, no. 5, pp. 1103–1119, Oct. 2001.

[32] J. Thimm, A. Mechler, H. Lin, S. Rhee, and R. Lal, "Calcium-dependent Open/Closed Conformations and Interfacial Energy Maps of Reconstituted Hemichannels," *J. Biol. Chem.*, vol. 280, no. 11, pp. 10646–10654, Mar. 2005.

[33] A. Quist, "Amyloid ion channels: A common structural link for protein-misfolding disease," *Proc. Natl. Acad. Sci.*, vol. 102, pp. 10427–10432, 2005.

[34] D. J. Muller and A. Engel, "Strategies to prepare and characterize native membrane proteins and protein membranes by AFM," *Curr. Opin. Colloid Interface Sci.*, vol. 13, no. 5, pp. 338–350, Oct. 2008.

[35] A. Giese, U. Bertsch, H. Kretzschmar, M. Habeck, T. Hirschberger, P. Tavan, C. Griesinger, A. Leonov, S. Ryazanov, P. Weber, M. Geissen, M. H. Groschup, and J. Wagner, "New Drug for Inhibiting Aggregation of Proteins Involved in Diseases Linked." US Patent WO2010000372 A2 Jan 7, 2010.

[36] J. Wagner, S. Ryazanov, A. Leonov, J. Levin, S. Shi, F. Schmidt, C. Prix, F. Pan-Montojo, U. Bertsch, G. Mitteregger-Kretzschmar, M. Geissen, M. Eiden, F. Leidel, T. Hirschberger, A. A. Deeg, J. J. Krauth, W. Zinth, P. Tavan, J. Pilger, M. Zweckstetter, T. Frank, M. Bähr, J. H. Weishaupt, M. Uhr, H. Urlaub, U. Teichmann, M. Samwer, K. Bötzel, M. Groschup, H. Kretzschmar, C. Griesinger, and A. Giese, "Anle138b: a novel oligomer modulator for disease-modifying therapy of neurodegenerative diseases such as prion and Parkinson's disease," *Acta Neuropathol. (Berl.)*, vol. 125, no. 6, pp. 795–813, Jun. 2013.

[37] B. S. Gadad, G. B. Britton, and K. S. Rao, "Targeting Oligomers in Neurodegenerative Disorders: Lessons from α-Synuclein, Tau, and Amyloid-β Peptide," *J. Alzheimers Dis.*, vol. 24, no. 0, pp. 223–232, Jan. 2011.

[38] J. R. Streffer, I. D. Grachev, C. Fitzer-Attas, B. Gomez-Mancilla, B. Boroojerdi, J. Bronzova, S. Ostrowitzki, S. J. Victor, P. Fontoura, and R. Alexander, "Prerequisites to launch neuroprotective trials in Parkinson's disease: An industry perspective," *Mov. Disord.*, vol. 27, no. 5, pp. 651–655, 2012.

[39] E. Karran, M. Mercken, and B. De Strooper, "The amyloid cascade hypothesis for Alzheimer's disease: an appraisal for the development of therapeutics," *Nat. Rev. Drug Discov.*, vol. 10, no. 9, pp. 698–712, Sep. 2011.

[40] T. Mirzabekov, M. C. Lin, W. L. Yuan, P. J. Marshall, M. Carman, K. Tomaselli, I. Lieberburg, and B. L. Kagan, "Channel formation in planar lipid bilayers by a neurotoxic fragment of the beta-amyloid peptide," *Biochem. Biophys. Res. Commun.*, vol. 202, no. 2, pp. 1142–1148, Jul. 1994.

[41] H. Jang, L. Connelly, F. Teran Arce, S. Ramachandran, B. L. Kagan, R. Lal, and R. Nussinov, "Mechanisms for the Insertion of Toxic, Fibril-like β-Amyloid Oligomers into the Membrane," *J. Chem. Theory Comput.*, vol. 9, no. 1, pp. 822–833, Jan. 2013.

[42] J. C. Diaz, O. Simakova, K. A. Jacobson, N. Arispe, and H. B. Pollard, "Small molecule blockers of the Alzheimer Abeta calcium channel potently protect neurons from Abeta cytotoxicity," *Proc. Natl. Acad. Sci. U. S. A.*, vol. 106, no. 9, pp. 3348–3353, Mar. 2009.

[43] Y. Miller, B. Ma, and R. Nussinov, "Polymorphism in Alzheimer Abeta amyloid organization reflects conformational selection in a rugged energy landscape," *Chem Rev*, vol. 110, pp. 4820–38, Aug. 2010.

[44] B. Ma and R. Nussinov, "Selective molecular recognition in amyloid growth and transmission and cross-species barriers," *J. Mol. Biol.*, vol. 421, no. 2–3, pp. 172–184, Aug. 2012.

[45] J. W. Wu, L. Breydo, J. M. Isas, J. Lee, Y. G. Kuznetsov, R. Langen, and C. Glabe, "Fibrillar oligomers nucleate the oligomerization of monomeric amyloid beta but do not seed fibril formation," *J. Biol. Chem.*, vol. 285, no. 9, pp. 6071–6079, Feb. 2010.

[46] A. R. A. Ladiwala, J. Litt, R. S. Kane, D. S. Aucoin, S. O. Smith, S. Ranjan, J. Davis, W. E. Van Nostrand, and P. M. Tessier, "Conformational differences between two amyloid β oligomers of similar size and dissimilar toxicity," *J. Biol. Chem.*, vol. 287, no. 29, pp. 24765–24773, Jul. 2012.

[47] S. Chimon, M. A. Shaibat, C. R. Jones, D. C. Calero, B. Aizezi, and Y. Ishii, "Evidence of fibril-like β-sheet structures in a neurotoxic amyloid intermediate of Alzheimer's β-amyloid," *Nat. Struct. Mol. Biol.*, vol. 14, no. 12, pp. 1157–1164, Dec. 2007.

[48] H. B. Pollard, E. Rojas, and N. Arispe, "A new hypothesis for the mechanism of amyloid toxicity, based on the calcium channel activity of amyloid beta protein (A beta P) in phospholipid bilayer membranes," *Ann N Acad Sci*, vol. 695, pp. 165–8, Sep. 1993.

[49] N. Arispe, H. B. Pollard, and E. Rojas, “beta-Amyloid Ca(2+)-channel hypothesis for neuronal death in Alzheimer disease,” *Mol. Cell. Biochem.*, vol. 140, no. 2, pp. 119–125, Nov. 1994.

[50] N. Arispe, H. B. Pollard, and E. Rojas, “Zn2+ interaction with Alzheimer amyloid beta protein calcium channels,” *Proc. Natl. Acad. Sci. U. S. A.*, vol. 93, no. 4, pp. 1710–1715, Feb. 1996.

[51] H. Jang, J. Zheng, and R. Nussinov, “Models of β-Amyloid Ion Channels in the Membrane Suggest That Channel Formation in the Bilayer Is a Dynamic Process,” *Biophys. J.*, vol. 93, pp. 1938–1949, 2007.

[52] H. Jang, J. Zheng, R. Lal, and R. Nussinov, “New structures help the modeling of toxic amyloidß ion channels,” *Trends Biochem. Sci.*, vol. 33, pp. 91–100, 2008.

[53] H. Jang, F. T. Arce, R. Capone, S. Ramachandran, R. Lal, and R. Nussinov, “Misfolded Amyloid Ion Channels Present Mobile β-Sheet Subunits in Contrast to Conventional Ion Channels,” *Biophys. J.*, vol. 97, pp. 3029–3037, 2009.

[54] H. Jang, F. T. Arce, S. Ramachandran, R. Capone, R. Azimova, B. L. Kagan, R. Nussinov, and R. Lal, “Truncated -amyloid peptide channels provide an alternative mechanism for Alzheimer’s Disease and Down syndrome,” *Proc. Natl. Acad. Sci.*, vol. 107, pp. 6538–6543, 2010.

[55] H. Jang, F. Teran Arce, S. Ramachandran, R. Capone, R. Lal, and R. Nussinov, “Structural Convergence Among Diverse, Toxic Œ≤-Sheet Ion Channels,” *J. Phys. Chem. B*, vol. 114, pp. 9445–9451, Jul. 2010.

[56] H. Jang, F. T. Arce, S. Ramachandran, R. Capone, R. Lal, and R. Nussinov, “β-Barrel Topology of Alzheimer’s β-Amyloid Ion Channels,” *J. Mol. Biol.*, vol. 404, pp. 917–934, 2010.

[57] R. Capone, H. Jang, S. A. Kotler, L. Connelly, F. Teran Arce, S. Ramachandran, B. L. Kagan, R. Nussinov, and R. Lal, “All-d-Enantiomer of beta-Amyloid Peptide Forms Ion Channels in Lipid Bilayers,” *J Chem Theory Comput*, vol. 8, pp. 1143–1152, Mar. 2012.

[58] R. Capone, H. Jang, S. A. Kotler, B. L. Kagan, R. Nussinov, and R. Lal, “Probing structural features of Alzheimer’s amyloid-β pores in bilayers using site-specific amino acid substitutions,” *Biochemistry (Mosc.)*, vol. 51, no. 3, pp. 776–785, Jan. 2012.

[59] L. Connelly, H. Jang, F. T. Arce, R. Capone, S. A. Kotler, S. Ramachandran, B. L. Kagan, R. Nussinov, and R. Lal, "Atomic force microscopy and MD simulations reveal pore-like structures of all-D-enantiomer of Alzheimer's β-amyloid peptide: relevance to the ion channel mechanism of AD pathology," *J. Phys. Chem. B*, vol. 116, no. 5, pp. 1728–1735, Feb. 2012.

[60] L. Connelly, H. Jang, F. T. Arce, S. Ramachandran, B. L. Kagan, R. Nussinov, and R. Lal, "Effects of point substitutions on the structure of toxic Alzheimer's β-amyloid channels: atomic force microscopy and molecular dynamics simulations," *Biochemistry (Mosc.)*, vol. 51, no. 14, pp. 3031–3038, Apr. 2012.

[61] B. L. Kagan, H. Jang, R. Capone, F. Teran Arce, S. Ramachandran, R. Lal, and R. Nussinov, "Antimicrobial Properties of Amyloid Peptides," *Mol. Pharm.*, vol. 9, no. 4, pp. 708–717, Apr. 2012.

[62] D. Liu, M. Pitta, J.-H. Lee, B. Ray, D. K. Lahiri, K. Furukawa, M. Mughal, H. Jiang, J. Villarreal, R. G. Cutler, N. H. Greig, and M. P. Mattson, "The KATP channel activator diazoxide ameliorates amyloid-β and tau pathologies and improves memory in the 3xTgAD mouse model of Alzheimer's disease," *J. Alzheimers Dis. JAD*, vol. 22, no. 2, pp. 443–457, 2010.

[63] T. S. Anekonda, J. F. Quinn, C. Harris, K. Frahler, T. L. Wadsworth, and R. L. Woltjer, "L-type voltage-gated calcium channel blockade with isradipine as a therapeutic strategy for Alzheimer's disease," *Neurobiol. Dis.*, vol. 41, no. 1, pp. 62–70, Jan. 2011.

[64] K. Murakami, K. Irie, A. Morimoto, H. Ohigashi, M. Shindo, M. Nagao, T. Shimizu, and T. Shirasawa, "Synthesis, aggregation, neurotoxicity, and secondary structure of various A beta 1-42 mutants of familial Alzheimer's disease at positions 21-23," *Biochem. Biophys. Res. Commun.*, vol. 294, no. 1, pp. 5–10, May 2002.

[65] P. M. Pifer, E. A. Yates, and J. Legleiter, "Point mutations in Aβ result in the formation of distinct polymorphic aggregates in the presence of lipid bilayers," *PloS One*, vol. 6, no. 1, p. e16248, 2011.

[66] K. Murakami, K. Irie, A. Morimoto, H. Ohigashi, M. Shindo, M. Nagao, T. Shimizu, and T. Shirasawa, "Neurotoxicity and physicochemical properties of Abeta mutant peptides from cerebral amyloid angiopathy: implication for the pathogenesis of cerebral amyloid angiopathy and Alzheimer's disease," *J. Biol. Chem.*, vol. 278, no. 46, pp. 46179–46187, Nov. 2003.

67] N. S. de Groot, F. X. Aviles, J. Vendrell, and S. Ventura, “Mutagenesis of the central hydrophobic cluster in Abeta42 Alzheimer’s peptide. Side-chain properties correlate with aggregation propensities,” *FEBS J.*, vol. 273, no. 3, pp. 658–668, Feb. 2006.

[68] M. Citron, “Strategies for disease modification in Alzheimer’s disease,” *Nat. Rev. Neurosci.*, vol. 5, no. 9, pp. 677–685, Sep. 2004.

[69] A. F. Teich and O. Arancio, “Is the amyloid hypothesis of Alzheimer’s disease therapeutically relevant?,” *Biochem. J.*, vol. 446, no. 2, pp. 165–177, Sep. 2012.

[70] J. Nunan and D. H. Small, “Regulation of APP cleavage by alpha-, beta- and gamma-secretases,” *FEBS Lett.*, vol. 483, no. 1, pp. 6–10, Oct. 2000.

[71] P. Prangkio, E. C. Yusko, D. Sept, J. Yang, and M. Mayer, “Multivariate analyses of amyloid-beta oligomer populations indicate a connection between pore formation and cytotoxicity,” *PloS One*, vol. 7, no. 10, p. e47261, 2012.

[72] B. L. Kagan and J. Thundimadathil, “Amyloid peptide pores and the beta sheet conformation,” *Adv Exp Med Biol*, vol. 677, pp. 150–67, 2010.

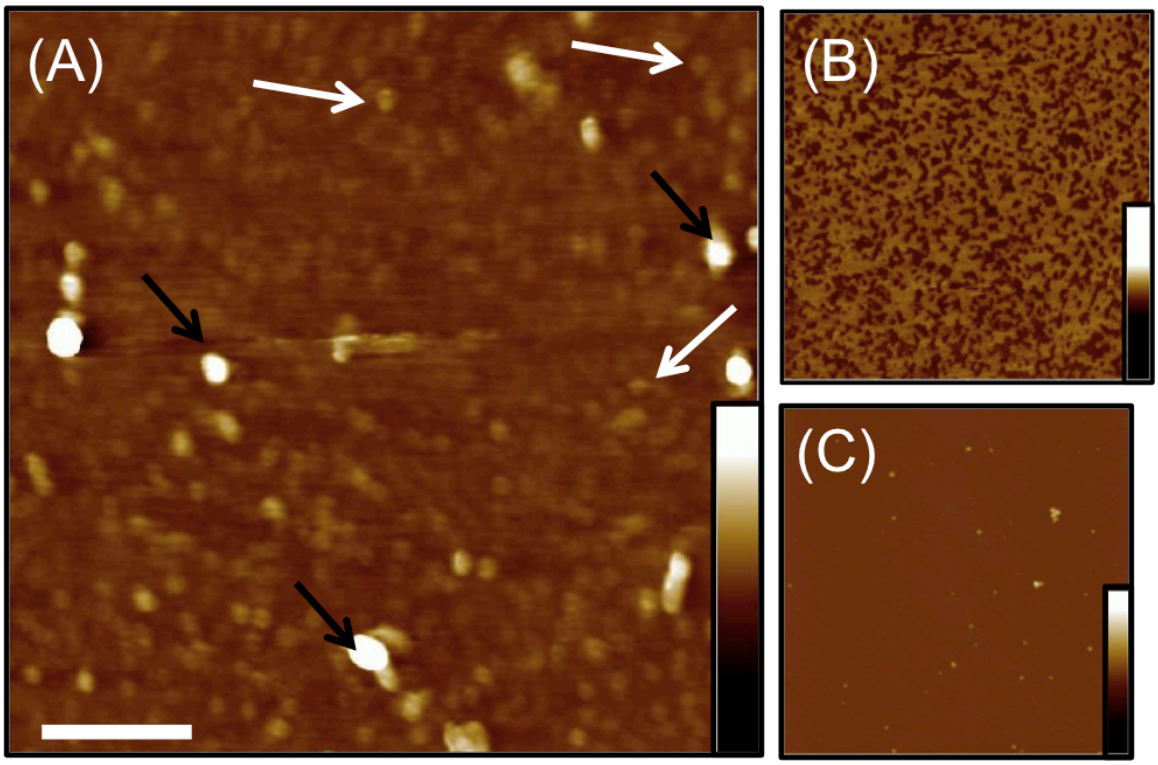

FIGURE 4.1 (A) AFM height image of brain derived Aβ particulate in air. Large globular deposits (black arrows) range in height from 4-10 nm and small, likely monomeric Aβ are approximately 1 nm in height (white arrows). No fibrillar species are observed. Scale bar 1 μm, height range 15 nm. (B) AFM height image of IgG in air (negative control). A uniform deposition of about 1 nm in height is seen absent of globular structures. Image size 1 μm, height range 10 nm (C) AFM height image of control dried PBS on mica in air. Contamination observed but no fibrillar or globular species are seen. Image size 3 μm, height range 15 nm.

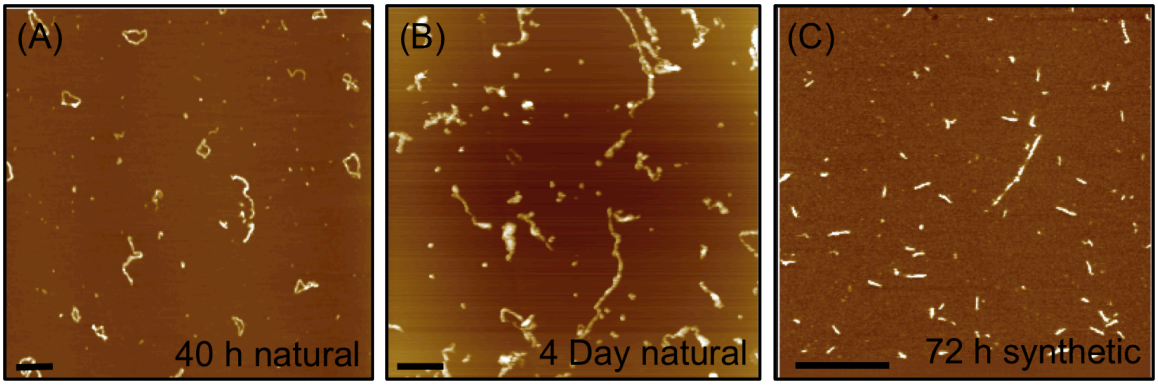

FIGURE 4.2 AFM height image of dried brain derived Aβ particulate after (A) 40 h and (B) 4 days of incubation in 37 °C. (C) AFM height image of synthetic dried natural $A\beta_{1-42}$ after 72 h of incubation at 37 °C. Fibers are observed after incubation of both synthetic and the natural Aβ. The synthetic Aβ is composed only of the full length form $A\beta_{1-42}$ while the Aβ natural particulate is composed of all forms of Aβ. Fiber formation is highly dependent on the incubation conditions such as pH, concentration, and time which may account for differences in the appearance of the fibers.

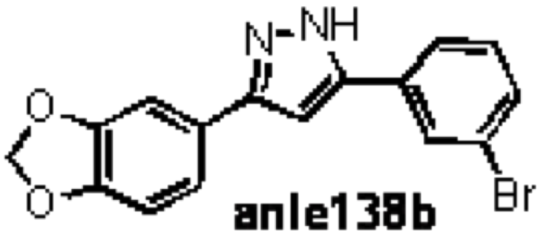

FIGURE 4.3 Chemical structure of the compound anle138b.[35], [36]

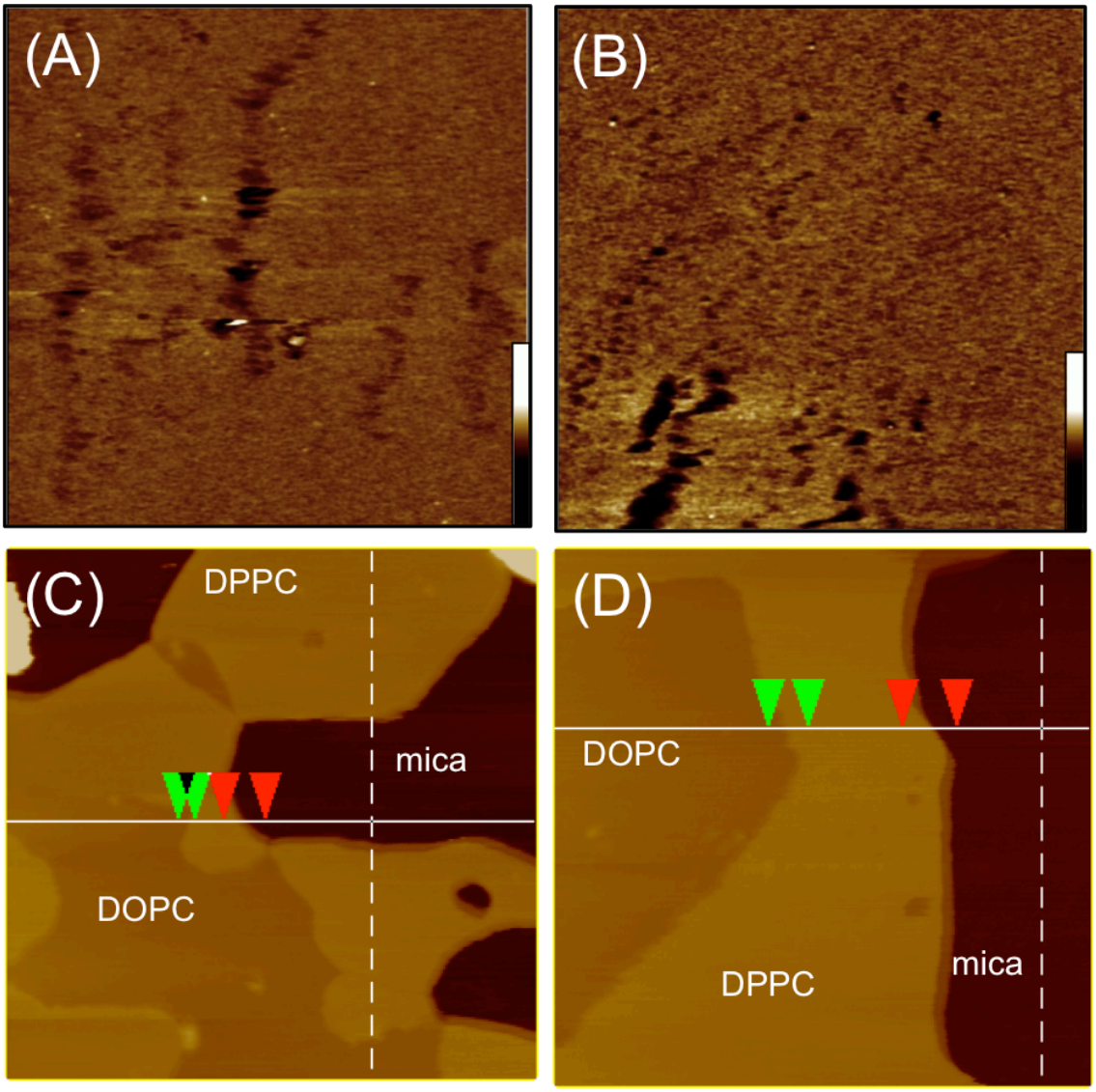

FIGURE 4.4 AFM height images in tapping mode of (A) DOPC only lipid bilayer (image size 3 μm and height range 20 nm) and (B) DOPC/anle138b lipid bilayer (image size 4 μm and height scale bar 10 nm). (C) AFM contact mode height image of DOPC/DPPC only bilayer on mica surface. The height difference between the DOPC and DPPC phases of the bilayer is 1.161 nm (green arrows). The height difference between the DPPC bilayer phase and the mica surface is 7.523 nm (red arrows). (D) AFM contact mode height image of DOPC/DPPC/anle138b bilayer on mica surface. The height change between the DOPC and DPPC phases of the bilayer with anle138b is 1.206 nm (green arrows). The height change between the DPPC bilayer phase with anle138b and the mica surface is 6.283 nm (red arrows). In all cases the pure lipid bilayer and the lipid bilayer incorporated with anle138b are indistinguishable.

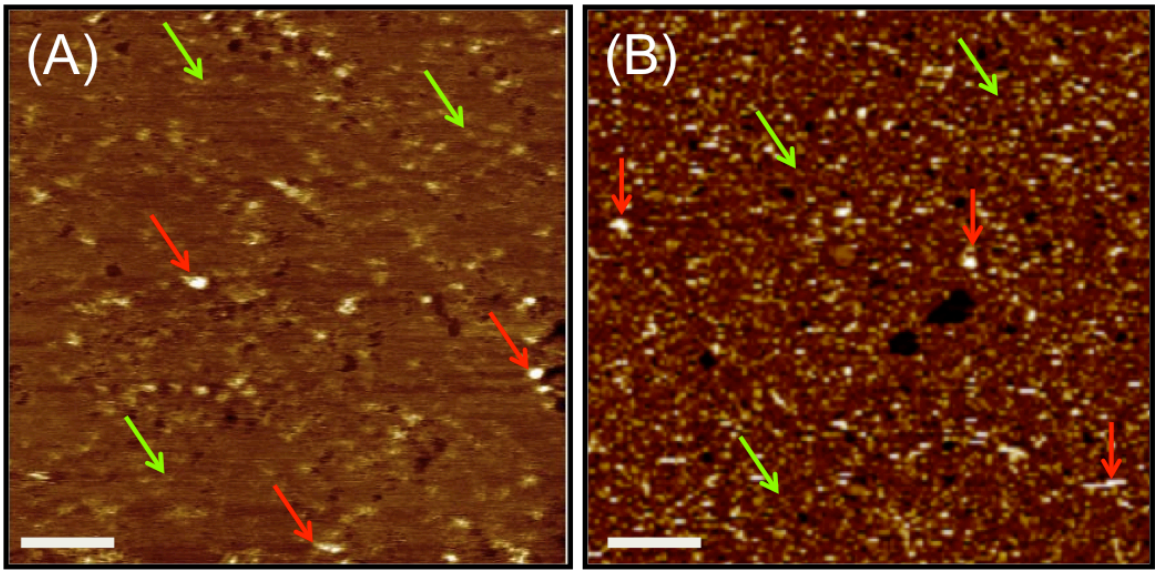

FIGURE 4.5 AFM height images show Aβ in lipid bilayers (A) with and (B) without the anle138b compound. Both bilayers (A) and (B) show indications of oligomeric Aβ embedded in the bilayers (red arrows). Smaller protrusions are observed in both bilayers indicating the possible presence of pore structures (green arrows). Higher resolution images of bilayers were not obtained for these samples due to instabilities. Scale bars 500 nm.

PART II: TECHNOLOGY DEVELOPMENT OF AN INTEGRATED ATOMIC FORCE MICROSCOPE AND ELECTRICAL RECORDING SYSTEM

CHAPTER 5

Fabrication and Characterization of Nanopore Support System for Membrane Studies

5.1 Abstract

Ion channels are membrane protein complexes essential to signaling and communication between cells of living systems. The dysfunction of ion channels has been widely studied and directly related to the pathology of neurodegenerative diseases such as Alzheimer's Disease and Parkinson's Disease, addiction, and some genetic disorders. Understanding the structure-activity relationship of these channels is crucial to understanding both normal and abnormal signaling mechanisms which can lead to therapeutic development, diagnosis, and/or prevention. However, direct correlation of the structure and activity of ion channels has yet to be accomplished. As a result, there is a disconnect in linking the data with respect to structure and activity of an ion channel, oftentimes with contradiction in these results. Solid-state substrates containing a single nanopore provide a unique environment for the study of proteins. Measuring electrical conductance in a nanopore system provides behavioral information specific to those

proteins localized in the area of the nanopore. Ion channels have been extensively studied using nanopore systems to characterize their activity by bilayer electrophysiology. Here we present the fabrication and characterization of a nanopore support system combining atomic force microscopy and electrophysiology into a single integrated system specific for the study of membranes and ion channels.

5.2 Introduction

Atomic force microscopy (AFM) has proven to be a useful tool for the 3D imaging of biological samples in physiological environments.[1]–[3] AFM can also provide dynamic structural information upon induced physical or chemical changes to the membrane environment.[4]–[9] By isolating membranes, individual protein structures such as ion channels have been resolved in AFM at nanometer resolution without staining or fixing.[1], [10]–[18] Ion channels are protein structures essential to signaling and maintaining homeostasis in living systems. Dysfunctional ion channels play a central role in many neurodegenerative diseases, addictions, and some genetic disorders.[10], [15], [19], [20] AFM provides more physiologically relevant structural data of membrane proteins over other techniques because ion channels may be observed in their natural conformations, in a supported lipid membrane, without isolation from the membrane or fixation treatments. However, an unresolved goal in the study of ion channels is direct characterization of the structure-activity relationship.[21] The combinatorial practice linking structure and activity data often leads to incomplete information, misleading data,

and apparent contradictory results.[21] A single method that examines the structure and activity of membranes or ion channels simultaneously would address these challenges and open the field of ion channel research to new and exciting data acquisition. More accurate information on the behavior of ion channels would improve diagnosis, therapeutic development, and prevention of ion channel disease and disorders.

Nanoporous samples have emerged as an exciting class of nanosensors that have gained attention for their sensitivity to conductance changes, especially in relation to the translocation of biomolecules.[22]–[32] Numerous nanoporous devices have been made from natural, artificial, and hybrid materials.[33] Graphene, for nanopore suspension, has been seen as a promising and reliable material due to its unique mechanical, electronic, thermal, and optical properties.[22], [28], [29], [34]–[36] Graphene is thin enough to be precisely drilled using a transmission electron microscopy and strong enough to be freely suspended over areas on the order of microns.[22], [29], [37]–[39]

Although much of the recent research on single nanopore conductance has been directed toward the application of DNA sequencing or biomolecule translocation, micro and nanopore devices have also been used to study the activity of ion channels.[20], [40] Current technologies for observing the electrical activity of ion channels utilize a free standing lipid bilayer membrane, droplet interface bilayer, or a supported lipid bilayer.[40] These electrical activity recording techniques are reproducible and widely accepted.

Presented is a fabrication technique and experimental setup for simultaneous high-resolution surface imaging by AFM and ionic conductance recording by planar lipid bilayer electrophysiology. Solid-state single nanopore substrates have been fabricated to

fit into the open interface of the multimode AFM. A single nanopore, drilled by TEM, is resolved by the AFM in the substrate and a stable open pore conductance measurement was recorded. This system is designed for suspended lipid bilayer experiments to obtain simultaneous functional and structural information.[23], [40]–[42] The correlation of conductance measurements to the specific structure of individual ion channels has not been previously possible. The device and setup we present here shows promise in such studies due to the imaging resolution, nanopore size, and conductance sensitivity shown on comparative scales with those of ion channels. The use of this technology would have major implications in, but not limited to, the study of neurological disorders, pathological studies, therapeutic screening, and drug addiction.

5.3 Materials

Silicon oxide membranes (SiO_2) were purchased from AppNano (Mountain View, Ca). Silicon oxide membranes are 200 nm thick on a 300 μm thick silicon substrate. The silicon substrate consists of a 20 μm x 20 μm window of suspended SiO_2 membrane that expands to 450 μm x 450 μm opening on the backside of the silicon (Fig. 1A, Fig. 3A). Single layer CVD graphene deposited on 20 μm thick Cu foil 2'' x 2'' was obtained from Graphene Supermarket (Calverton, NY). A Quanta™ 3D FEG focused ion beam (FIB) was used to drill through the SiO_2 suspended membrane (Calit2 Microscopy Center, UC Irvine). Either iron(III) chloride hexahydrate (FeCl3 • 6H2O) ≥ 98% solution (Sigma Aldrich) or Copper Etch APS-100 (Transene Co.) was used to dissolve the Cu substrate

of the graphene. Atomic layer deposition (ALD) of 5 nm of Al_2O_3 was performed using a GEMSTAR™ Benchtop Atomic Layer Deposition (ALD) Process System (Wanunu Nanoscale Biophysics lab, Northeastern University) or the Beneq TFS200 Atomic Layer Deposition (Nano3 Facility, UCSD). A transmission electron microscope (TEM) (JEOL 2010, Japan) from the Nanomaterials Instrumentation Facility at Northeastern University was used for drilling through graphene/Al_2O_3 membrane layer. AFM imaging was completed using a Bruker Multimode Nanoscope IV system with silicon nitride cantilevers (k = 0.08N/m) and AFM force volume imaging was done using silicon cantilevers (k = 3.0N/m). Conductance measurements were completed using an in-house designed (Brian Meckes, Lal Lab UCSD) double chamber cup system (Machine Shop UC San Diego) (Fig. 5.2B), liquid cell, Ag/AgCl wire electrodes, 1 M KCl solution, a Dakon Amplifier, and Nanoscope IV software. Ecoflex ® Supersoft 5 silicone cured rubber was used as an insulating sealant of the nanopore sample in the double chamber cup.

5.4 Results

5.4.1 Nanopore Fabrication Process

To fabricate a single nanopore support the Si/SiO_2 substrates were used as a base for the processing (Fig 5.1A, Fig 5.3A). A single hole with a diameter of 1 μm was drilled by FIB through the center of the SiO_2 20 μm x 20 μm suspended membrane area (Fig 5.1B, Fig 5.3B). FIB provides a fast and reproducible means for opening the 1 μm

gaping hole in the sample which allows for diffusion of electrolytes to the nanopore. The SiO_2 membranes were then cleaned in piranha solution to eliminate organic and inorganic contamination; in some cases this step was performed in a clean room to further minimize contamination. A sample of graphene on Cu was spin coated (graphene side up) with PMMA for 50 s and baked on a hot plate at 180 °C for 10 min. PMMA/graphene/Cu samples were floated (Cu side down) on a $FeCl_3 \bullet 6H_2O$ solution or copper etch APS-100 and left until the Cu foil had completely dissolved (~24 h). Graphene layers float on the surface of the chosen Cu etching solution and remain intact after dissolution of the Cu substrate. Using tweezers, the remaining PMMA/graphene sample was transferred several times to dishes of fresh DI H_2O as a rinsing procedure. Using tweezers, a PMMA/graphene flake was placed over the center of the cleaned SiO_2 membranes to ensure coverage of the entire 1 μm FIB hole area and allowed to dry (~24 h) (Fig. 5.1C). Graphene binds tightly to the SiO_2 upon drying, securing it as a suspended membrane over the FIB gaping hole. Dried samples were soaked in acetone to dissolve the top layer of PMMA (Fig. 5.1D). To provide electrical insulation and structural reinforcement 5 nm of Al_2O_3 was deposited on the sample by ALD (Fig 5.1E, Fig 5.3C). ALD provides a uniform coating of Al_2O_3 to all surfaces of each sample.[22], [38], [43] Finally, a nanopore was drilled through the center of the graphene/Al_2O_3 suspended membrane by TEM (Fig 5.1F, Fig 5.3D). The nanopore sample was then cleaned with acetone, isopropanol, and UV/ozone cleaner for 15 min before use in conductance measurements.

5.4.2 Experimental Setup for Imaging and Conductance

The Bruker multimode AFM's open interface allows for incorporation of custom made devices and additional property measurements while scanning a material's surface. We utilized this feature to incorporate ionic conductance recording through a nanopore while imaging simultaneously. A Teflon double chamber cup to hold the nanopore support was designed by the Lal lab (Brian Meckes, Lal Lab, UCSD) and fabricated at the UCSD machine shop (Fig 5.2B). This chamber is glued to a metal puck and holds the nanopore support on the scanner head of the AFM. The nanopore sample sits on the square inset of the top chamber piece (Fig. 5.2B). When filled with buffer, the only path electrically connecting the top and bottom chambers is through the nanopore. Therefore any electrical signal observed is a direct result of ionic transfer through this nanopore. The nanopore support was sealed into the top chamber using a continuous layer of fast curing Ecoflex® 5 silicone.

AFM imaging in liquid is completed as normal, by deflection feedback, on the nanopore sample in the double chamber cup. An Ag/AgCl electrode was placed through a port of the liquid cell and another similar electrode was embedded in the opposite chamber of the double chamber cup (Fig 5.2A, green lines). The entire AFM base was placed in a Faraday cage on in-house bungee cord suspended platform for noise isolation. A complete schematic of the experimental setup is shown in Fig. 5.2A.

5.4.3 AFM Analysis and Conductance Characterization of Nanopore

Images of the nanopore support were taken periodically throughout the fabrication process. The 20 μm x 20 μm suspended SiO_2 area was easily visible in SEM (Fig 5.3A and Fig 5.3B inset) and in AFM (Fig 5.4A) enabling for eventual centered drilling of the nanopore. The AFM height images show a large deformation pattern of the suspended SiO_2 square that is not seen in SEM (Fig 5.4A). This deformation is likely due to stress relief during the etching away of the Si layer from below. The center area of this square where the graphene membrane will reside appears to have very little deformation in comparison to the edges. The FIB drilled hole placed in the center of this square is also easily visible in SEM (Fig 5.3B), TEM (Fig 5.3C) and AFM even after deposition of the graphene/Al_2O_3 layer (Fig 5.4A, B). Complete coverage of the FIB hole with graphene was confirmed in TEM (Fig 5.3C) before drilling of the nanopore (Fig 5.3D). Complete coverage of the 1 μm hole by the graphene/Al_2O_3 membrane can also quickly be determined by confirming little to no conductance (<0.05nS). AFM imaging reveals the nanopore (Fig 5.4C), which is found by sequentially zooming in on the center of the FIB hole such as seen in Fig. 5.4. In high quality, clean samples with a very sharp AFM tip the nanopore size can be approximated in the AFM image and compared to the size observed in TEM as seen in Fig 5.3D and Fig 5.4C. The square shape of the nanopore shown in Fig 5.4C is likely due to effects of the geometry of the AFM tip (radius ~ 30nm). The small scan size and features of the solid state nanopore are on the same scale

as high resolution scans of membranes and ion channel structures, which are approximated around ~10 nm in diameter.

Ion conductance measurements are a good way to probe the pore geometry.[22], [31], [35], [38], [44] Neglecting access resistance for our large pores, pore conductance relates to geometry via the following equation:[31], [44]

$$G = \frac{\pi d_{pore}^2}{4L_{pore}}\left((\mu_K + \mu_{Cl})n_{KCl}e + \mu_K \frac{4\sigma}{d_{pore}}\right)$$

Where G is conductance, d_{pore} is the pore diameter, L_{pore} is the pore cylindrical length, n_{KCl} is the concentration of the buffer, e is elementary charge, σ is the surface charge density in the nanopore, μ_K and μ_{Cl} are the electrophoretic mobilities of the two solution ions potassium and chloride. A 1 M KCl buffer was used in the work reported here. The electrophoretic mobilities of potassium and chloride are $\mu_K = 7.616 \times 10^{-8}$ m^2/Vs and $\mu_{Cl} = 7.909 \times 10^{-8}$ m^2/Vs at room temperature.[31], [38]

To characterize the mechanical properties of the nanopore supports, three parameters were evaluated via AFM force mapping, before and after drilling the nanopore by TEM; (i) the sample deformation (δ), ii) the sample stiffness (dF/dδ) at F=100 nN load and iii) the adhesion force between the AFM tip and the sample. A silicon nitride cantilever with k = 3.0 N/m was used. A representative example of the results obtained for one of the nanopores is given in Fig. 5.6 A and B, while the summary of the mean values obtained for all nanopores (without a nanopore and with a nanopore) is given in Fig 5.6 C. The missing values (white spots) in some locations of the stiffness

map mean that the force curves took atypical shapes making it not possible to obtain the stiffness in those locations.

5.5 Discussion

Each step in the fabrication of the nanopore support was chosen with consideration of fabrication ease as well as function. Silicon oxide on silicon is an ideal material combination to use for the base structure of the nanopore support due to its ease of fabrication, well-characterized electrical properties, reproducibility, and commercial availability.[23], [37], [45] Silicon oxide provides an insulating coating to the large area of the substrate, an essential property to isolate the two compartments of the electrical recording setup. By using single graphene deposition, as opposed to the multilayer structure described by Bashir et al., the suspended membrane can be formed quickly (~5 s of TEM drilling) in one round of fabrication while still producing a functional device.[38] When the suspended graphene or graphene/Al_2O_3 deposition showed incomplete coverage or had been damaged during use it could be easily removed with two rounds of piranha cleaning. Therefore, with a single deposition round of graphene/Al_2O_3 the Si/SiO_2 substrates could be redeposited with a new layer of graphene/Al_2O_3 and reused until the SiO_2 membrane was compromised, extending the total lifetime of a sample set. The spin coated PMMA on the graphene enables the graphene to be handled from one solution to another for cleaning as well as positioned on samples with ease.[46] TEM

drilling provides a lateral resolution <1 nm in the controlled formation of nanopores through thin membranes.[37], [47]

Comparisons of AFM images between nanopore supports revealed that a large variation in the final surface structure of these samples was present. In some samples it was observed that, during TEM drilling of the nanopore, the pore would collapse on itself and need to be reopened with the electron beam. This behavior was observed to correlate with the presence of contamination growth (Fig. 5.7A-C).[39] Although pore closing and contamination growth have been established as independent mechanisms they can be linked in these samples by processing time.[29], [39] A nanopore that closes upon drilling requires longer drilling times. Extended beam exposure increases the amount of contamination growth.[39] Despite this observation, many samples were easily drilled by TEM in one attempt and as a result appeared to have smooth surfaces. In cases where the sample surface appeared smooth, the nanopore itself could often be resolved and measured in AFM images (Fig. 5.4, Fig 5.7D). We did not find these depositions to have a qualitative correlation to any trend in conductance values. Such depositions could play a part in the large variation seen in calculated surface charge values, but was not quantified. The presence of contamination should carefully be considered before utilizing any nanopore support for additional studies.

The predicted conductance from the given equation is dependent on pore morphology and surface charge density of the sample. High surface charge density for graphene/Al_2O_3 layers is considered 200 mC/m^2 and minimum surface charge is 0 mC/m^2.[31], [38] A range of solid-state nanopore sizes was fabricated, *with* d_{pore} values of 20-50 nm and $L_{pore}\approx$5 nm. The expected conductance values in this nanopore size

range for high and low surface charge density samples would be approximately 1100-6100 nS and 940-5900 nS respectively. Open conductance values of individual solid-state nanopores were measured by ramping at 0.4 mV/s over ± 10 mV. The conductance of the ~ 25 nm diameter nanopore sample (Fig. 5.5) was measured to be 2765 nS, which falls in the reasonable range of conductance values for 20-50 nm nanopores.

There appears to be a weak correlation between the topographical features in the samples and their mechanical properties (Fig. 5.6 A). The elevated topographical features observed in the AFM images, attributed to contamination, have somewhat distinguishable deformation and stiffness as compared to the flatter, cleaner, regions. This would suggest that the contamination is either softer or harder than the underlying graphene/Al_2O_3 layer. However, this correlation is lost when observed in detail. Regions of larger sample deformation (soft regions) should coincide with regions of decreased stiffness, but this is not observed in the force maps. The adhesion force map also shows non-uniform characteristics across the sample, but it is difficult to correlate them with the topographical features. All these non-uniform mechanical and topographical properties suggest the presence of impurities with similar mechanical properties as the underlying graphene/Al_2O_3 surface. We hypothesize that these impurities are capable of modifying the surface charge of the nanopore and are responsible for the lack of correlation between the nanopore conductivity and its diameter. Analysis of the mechanical properties evaluated before and after TEM drilling show that there is no statistically significant difference ($p>0.05$ level) (Fig. 5.6C), indicating that the cavity of the nanopore does not alter the mechanical properties of the supporting membrane.

Nanopore supports that showed a smooth surface in AFM also easily revealed the location and size of the nanopore itself (Fig 5.4C, Fig 5.7D). To our knowledge, such small nanopores in graphene/Al_2O_3 membranes have not been previously shown in AFM. Characterizing the local environment of a solid-state nanopore by AFM could potentially be used in single molecular studies by functionalizing the AFM tip. Additionally, the resolution and size of these pores, 20 nm nanopore in a 200 nm scan size in Fig. 5.4C and Fig 5.7D, by AFM are on the same scale as images of supported or suspended lipid bilayer over the solid state nanopore.[10]–[12], [15] Individual ion channels and hemichannels in supported membranes have often been resolved at larger scan sizes.[5], [10]–[12], [15], [21], [42], [48] These solid-state nanopores are therefore suitable for the intended application of ion channel studies. The deposition of a complete bilayer with incorporated ion channels opens the possibility of providing simultaneous structural and functional characterization for these channels.

5.6 Conclusions

We have successfully fabricated nanopore supports that have the potential to be utilized for simultaneous structure-activity studies of ion channels in suspended lipid bilayers. We have shown that single solid-state nanopores can be reproducibly fabricated in graphene reinforced with Al_2O_3. The conductance values of the open nanopore in a buffer solution indicate 5nm of Al_2O_3 deposition is sufficient for electrical insulation between the double chambers. The hierarchy of the sample structure allows for quick and

easy location of the single nanopore in AFM. Lipid bilayers with embedded ion channels suspended over this nanopore will therefore likely be easily located. The conductance values of open nanopores were measured in the expected nS range and are, therefore, suitable for ion channel studies. The use of a solid-state nanopore support in AFM allows for localized characterization in and around the nanopore. By combining both imaging and activity characterization techniques we have designed a system suitable for ion channel studies restricted to a small nanospace. Correlated structure and activity information on ion channels yielded from this system may have major implications to study of neurological diseases, drug addiction, biological pathways, and protein structures.

5.7 Acknowledgements

I would like to acknowledge my co-authors of this paper. Chapter 6, in part, is currently being prepared for submission for publication of the material, Connelly, L., Meckes, B., Larkin, J, Gillman, A., Arce, F. T., Wanunu, M., Lal, R. No authors have competing interests.

This research is supported by NIH grants R01 DA025296-01, R01 AG028709-01, and R01 DA024871-10A1. Thanks are given to the Microscopy Center in Calit2 at the University of California, Irvine for access to the FEI Quanta 3D FEG focused ion beam and Matthew Sullivan and Amirhossein Khalajhedayati at UCI for their assistance in operation. The Wanunu Lab of Nanoscale Biophysics at Northeastern University in

Boston, Ma is thanked for their aid and resources used in the preparation of the nanopore supports. The cleanroom in the Nano3 facility at UCSD is thanked for the use of space and equipment used during the fabrication of some nanopore supports. Dr. Paul Hansma, Brian Meckes, and the Machine Shop at UCSD and is thanked for their assistance in the design and fabrication the double chamber cup.

5.8 References

[1] D. Fotiadis, S. Scheuring, S. A. Müller, A. Engel, and D. J. Müller, "Imaging and manipulation of biological structures with the AFM," *Micron*, vol. 33, no. 4, pp. 385–397, Jan. 2002.

[2] R. Lal and S. A. John, "Biological applications of atomic force microscopy," *Am. J. Physiol. - Cell Physiol.*, vol. 266, no. 1, pp. C1–C21, Jan. 1994.

[3] J. K. H. Hörber and M. J. Miles, "Scanning Probe Evolution in Biology," *Science*, vol. 302, no. 5647, pp. 1002–1005, Nov. 2003.

[4] A. P. Quist, S. K. Rhee, H. Lin, and R. Lal, "Physiological Role of Gap-Junctional Hemichannels Extracellular Calcium-Dependent Isosmotic Volume Regulation," *J. Cell Biol.*, vol. 148, no. 5, pp. 1063–1074, Mar. 2000.

[5] F. Tokumasu, A. J. Jin, and J. A. Dvorak, "Lipid membrane phase behaviour elucidated in real time by controlled environment atomic force microscopy," *J. Electron Microsc. (Tokyo)*, vol. 51, no. 1, pp. 1–9, Mar. 2002.

[6] A. Parbhu, H. Lin, J. Thimm, and R. Lal, "Imaging real-time aggregation of amyloid beta protein (1-42) by atomic force microscopy," *Peptides*, vol. 23, no. 7, pp. 1265–1270, Jul. 2002.

[7] H. Lin, D. O. Clegg, and R. Lal, "Imaging Real-Time Proteolysis of Single Collagen I Molecules with an Atomic Force Microscope†," *Biochemistry (Mosc.)*, vol. 38, no. 31, pp. 9956–9963, Aug. 1999.

[8] R. Lal, B. Drake, D. Blumberg, D. R. Saner, P. K. Hansma, and S. C. Feinstein, "Imaging real-time neurite outgrowth and cytoskeletal reorganization with an atomic force microscope," *Am. J. Physiol. - Cell Physiol.*, vol. 269, no. 1, pp. C275–C285, Jul. 1995.

[9] M. B. Viani, L. I. Pietrasanta, J. B. Thompson, A. Chand, I. C. Gebeshuber, J. H. Kindt, M. Richter, H. G. Hansma, and P. K. Hansma, "Probing protein–protein interactions in real time," *Nat. Struct. Mol. Biol.*, vol. 7, no. 8, pp. 644–647, Aug. 2000.

[10] A. Quist, "Amyloid ion channels: A common structural link for protein-misfolding disease," *Proc. Natl. Acad. Sci.*, vol. 102, pp. 10427–10432, 2005.

[11] L. Connelly, H. Jang, F. T. Arce, R. Capone, S. A. Kotler, S. Ramachandran, B. L. Kagan, R. Nussinov, and R. Lal, "Atomic force microscopy and MD simulations reveal pore-like structures of all-D-enantiomer of Alzheimer's β-amyloid peptide: relevance to the ion channel mechanism of AD pathology," *J. Phys. Chem. B*, vol. 116, no. 5, pp. 1728–1735, Feb. 2012.

[12] L. Connelly, H. Jang, F. T. Arce, S. Ramachandran, B. L. Kagan, R. Nussinov, and R. Lal, "Effects of point substitutions on the structure of toxic Alzheimer's β-amyloid channels: atomic force microscopy and molecular dynamics simulations," *Biochemistry (Mosc.)*, vol. 51, no. 14, pp. 3031–3038, Apr. 2012.

[13] R. Lal, H. Kim, R. M. Garavito, and M. F. Arnsdorf, "Imaging of reconstituted biological channels at molecular resolution by atomic force microscopy," *Am. J. Physiol.*, vol. 265, no. 3 Pt 1, pp. C851–856, Sep. 1993.

[14] R. Lal, "Imaging molecular structure of channels and receptors with an atomic force microscope," *Scanning Microsc. Suppl.*, vol. 10, pp. 81–95; discussion 95–96, 1996.

[15] H. Lin, R. Bhatia, and R. Lal, "Amyloid beta protein forms ion channels: implications for Alzheimer's disease pathophysiology," *FASEB J*, vol. 15, pp. 2433–44, Nov. 2001.

[16] J. Yang, L. K. Tamm, T. W. Tillack, and Z. Shao, "New Approach for Atomic Force Microscopy of Membrane Proteins: The Imaging of Cholera Toxin," *J. Mol. Biol.*, vol. 229, no. 2, pp. 286–290, Jan. 1993.

[17] P. K. Hansma, V. B. Elings, O. Marti, and C. E. Bracker, "Scanning tunneling microscopy and atomic force microscopy: application to biology and technology," *Science*, vol. 242, no. 4876, pp. 209–216, Oct. 1988.

[18] R. Lal and M. F. Arnsdorf, "Multidimensional atomic force microscopy for drug discovery: a versatile tool for defining targets, designing therapeutics and monitoring their efficacy," *Life Sci*, vol. 86, pp. 545–62, Apr. 2010.

[19] C. M. Dobson, "Protein folding and misfolding," *Nature*, vol. 426, pp. 884–90, Dec. 2003.

[20] M. J. Ackerman and D. E. Clapham, "Ion Channels — Basic Science and Clinical Disease," *N. Engl. J. Med.*, vol. 336, no. 22, pp. 1575–1586, 1997.

[21] M. Yeager and A. L. Harris, "Gap junction channel structure in the early 21st century: facts and fantasies," *Curr. Opin. Cell Biol.*, vol. 19, no. 5, pp. 521–528, Oct. 2007.

[22] B. M. Venkatesan and R. Bashir, "Nanopore sensors for nucleic acid analysis," *Nat. Nanotechnol.*, vol. 6, no. 10, pp. 615–624, Oct. 2011.

[23] A. P. Quist, A. Chand, S. Ramachandran, C. Daraio, S. Jin, and R. Lal, "Atomic force microscopy imaging and electrical recording of lipid bilayers supported over microfabricated silicon chip nanopores: lab-on-a-chip system for lipid membranes and ion channels," *Langmuir*, vol. 23, pp. 1375–80, Jan. 2007.

[24] M. Wanunu, "Nanopores: A journey towards DNA sequencing," *Phys. Life Rev.*, vol. 9, no. 2, pp. 125–158, Jun. 2012.

[25] C. A. Merchant, K. Healy, M. Wanunu, V. Ray, N. Peterman, J. Bartel, M. D. Fischbein, K. Venta, Z. Luo, A. T. C. Johnson, and M. Drndić, "DNA translocation through graphene nanopores," *Nano Lett.*, vol. 10, no. 8, pp. 2915–2921, Aug. 2010.

[26] M. Wanunu and A. Meller, "Chemically Modified Solid-State Nanopores," *Nano Lett.*, vol. 7, no. 6, pp. 1580–1585, Jun. 2007.

[27] D. Branton, D. W. Deamer, A. Marziali, H. Bayley, S. A. Benner, T. Butler, M. Di Ventra, S. Garaj, A. Hibbs, X. Huang, S. B. Jovanovich, P. S. Krstic, S. Lindsay, X. S. Ling, C. H. Mastrangelo, A. Meller, J. S. Oliver, Y. V. Pershin, J. M. Ramsey, R. Riehn, G. V. Soni, V. Tabard-Cossa, M. Wanunu, M. Wiggin, and J. A. Schloss, "The potential and challenges of nanopore sequencing," *Nat. Biotechnol.*, vol. 26, no. 10, pp. 1146–1153, Oct. 2008.

[28] A. Bahrami, F. Doğan, D. Japrung, and T. Albrecht, "Solid-state nanopores for biosensing with submolecular resolution," *Biochem. Soc. Trans.*, vol. 40, no. 4, pp. 624–628, Aug. 2012.

[29] S. M. Iqbal and R. Bashir, "Nanoelectronic-Based Detection for Biology and Medicine," in *Springer Handbook of Automation*, Springer Berlin Heidelberg, 2009, pp. 1433–1449.

[30] C. Jiang, S. Markutsya, Y. Pikus, and V. V. Tsukruk, "Freely suspended nanocomposite membranes as highly sensitive sensors," *Nat. Mater.*, vol. 3, no. 10, pp. 721–728, Oct. 2004.

[31] R. M. M. Smeets, U. F. Keyser, D. Krapf, M.-Y. Wu, N. H. Dekker, and C. Dekker, "Salt dependence of ion transport and DNA translocation through solid-state nanopores," *Nano Lett.*, vol. 6, no. 1, pp. 89–95, Jan. 2006.

[32] M. Wanunu, J. Sutin, B. McNally, A. Chow, and A. Meller, "DNA Translocation Governed by Interactions with Solid-State Nanopores," *Biophys. J.*, vol. 95, no. 10, pp. 4716–4725, Nov. 2008.

[33] A. Oukhaled, L. Bacri, M. Pastoriza-Gallego, J.-M. Betton, and J. Pelta, "Sensing proteins through nanopores: fundamental to applications," *ACS Chem. Biol.*, vol. 7, no. 12, pp. 1935–1949, Dec. 2012.

[34] M. J. Allen, V. C. Tung, and R. B. Kaner, "Honeycomb carbon: a review of graphene," *Chem. Rev.*, vol. 110, no. 1, pp. 132–145, Jan. 2010.

[35] S. Banerjee, J. Shim, J. Rivera, X. Jin, D. Estrada, V. Solovyeva, X. You, J. Pak, E. Pop, N. Aluru, and R. Bashir, "Electrochemistry at the edge of a single graphene layer in a nanopore," *ACS Nano*, vol. 7, no. 1, pp. 834–843, Jan. 2013.

[36] D. B. Wells, M. Belkin, J. Comer, and A. Aksimentiev, "Assessing graphene nanopores for sequencing DNA," *Nano Lett.*, vol. 12, no. 8, pp. 4117–4123, Aug. 2012.

[37] A. J. Storm, J. H. Chen, X. S. Ling, H. W. Zandbergen, and C. Dekker, "Fabrication of solid-state nanopores with single-nanometre precision," *Nat. Mater.*, vol. 2, no. 8, pp. 537–540, Aug. 2003.

[38] B. M. Venkatesan, D. Estrada, S. Banerjee, X. Jin, V. E. Dorgan, M.-H. Bae, N. R. Aluru, E. Pop, and R. Bashir, "Stacked graphene-Al2O3 nanopore sensors for sensitive detection of DNA and DNA-protein complexes," *ACS Nano*, vol. 6, no. 1, pp. 441–450, Jan. 2012.

[39] A. E. Ennos, "The origin of specimen contamination in the electron microscope," *Br. J. Appl. Phys.*, vol. 4, no. 4, p. 101, Apr. 1953.

[40] P. Kongsuphol, K. B. Fang, and Z. Ding, "Lipid bilayer technologies in ion channel recordings and their potential in drug screening assay," *Sens. Actuators B Chem.*, vol. 185, pp. 530–542, Aug. 2013.

[41] X. Han, A. Studer, H. Sehr, I. Geissbühler, M. Di Berardino, F. K. Winkler, and L. X. Tiefenauer, "Nanopore Arrays for Stable and Functional Free-Standing Lipid Bilayers," *Adv. Mater.*, vol. 19, no. 24, pp. 4466–4470, 2007.

[42] C. Ambrosi, D. Boassa, J. Pranskevich, A. Smock, A. Oshima, J. Xu, B. J. Nicholson, and G. E. Sosinsky, "Analysis of four connexin26 mutant gap junctions and hemichannels reveals variations in hexamer stability," *Biophys. J.*, vol. 98, no. 9, pp. 1809–1819, May 2010.

[43] P. Chen, T. Mitsui, D. B. Farmer, J. Golovchenko, R. G. Gordon, and D. Branton, "Atomic Layer Deposition to Fine-Tune the Surface Properties and Diameters of Fabricated Nanopores," *Nano Lett.*, vol. 4, no. 7, pp. 1333–1337, Jul. 2004.

[44] M. J. Kim, M. Wanunu, D. C. Bell, and A. Meller, "Rapid Fabrication of Uniformly Sized Nanopores and Nanopore Arrays for Parallel DNA Analysis," *Adv. Mater.*, vol. 18, no. 23, pp. 3149–3153, 2006.

[45] A. J. Storm, J. H. Chen, X. S. Ling, H. W. Zandbergen, and C. Dekker, "Electron-beam-induced deformations of SiO2 nanostructures," *J. Appl. Phys.*, vol. 98, no. 1, pp. 014307–014307–8, 2005.

[46] L. G. De Arco, Y. Zhang, A. Kumar, and C. Zhou, "Synthesis, Transfer, and Devices of Single- and Few-Layer Graphene by Chemical Vapor Deposition," *IEEE Trans. Nanotechnol.*, vol. 8, no. 2, pp. 135–138, 2009.

[47] H. Chang, F. Kosari, G. Andreadakis, M. A. Alam, G. Vasmatzis, and R. Bashir, "DNA-Mediated Fluctuations in Ionic Current through Silicon Oxide Nanopore Channels," *Nano Lett.*, vol. 4, no. 8, pp. 1551–1556, Aug. 2004.

[48] A. Studer, X. Han, F. K. Winkler, and L. X. Tiefenauer, "Formation of individual protein channels in lipid bilayers suspended in nanopores," *Colloids Surf. B Biointerfaces*, vol. 73, no. 2, pp. 325–331, Oct. 2009.

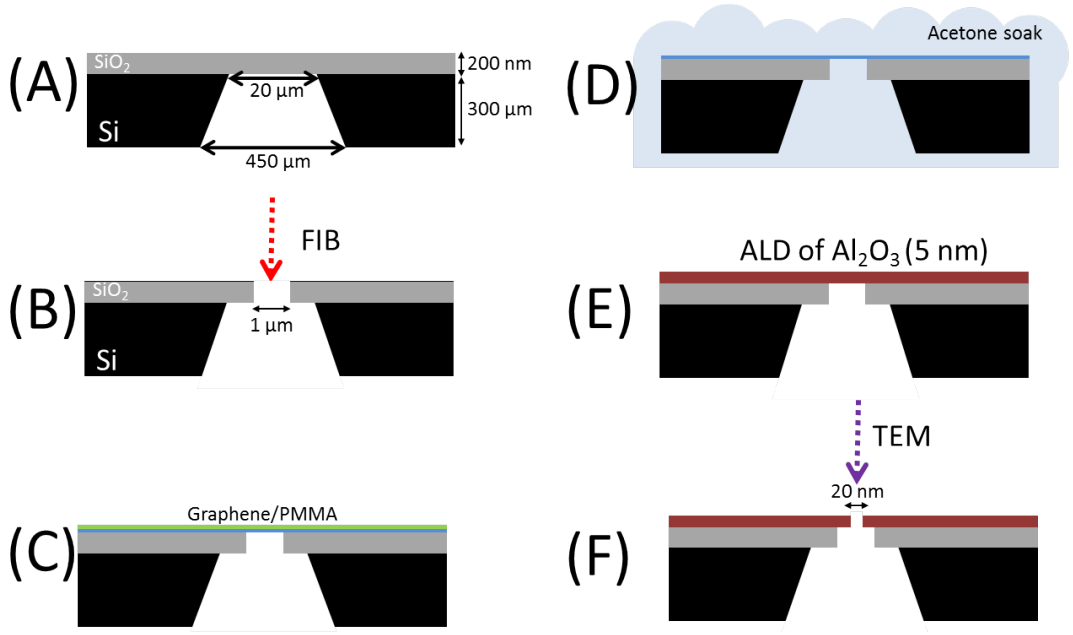

FIGURE 5.1 A cross- sectional schematic sequencing of the processing of a solid-state substrate containing a single nanopore. (A) The starting substrate is a 6 mm x 6 mm x 300 µm silicon substrate (black) with a 200 nm SiO_2 layer (gray). The silicon has been etched to form a pyramidal window spanning from 450 µm x 450 µm to a 20 µm x 20 µm window at the SiO_2 surface. This results in a 20 µm x 20 µm window of suspended SiO_2 in the center of the substrate. (B) A focused ion beam (red) is used to find the center of the 20 µm x 20 µm SiO_2 window and drill a 1 µm hole. (C) A graphene flake (blue) coated with PMMA (green) floating on the surface of H_2O is placed over the 1 µm FIB hole and allowed to dry. (D) The dried sample is soaked in acetone for 24 hrs to dissolve the PMMA leaving a graphene sheet suspended over the 1 µm hole. (E) 5 nm of Al_2O_3 (red) is deposited by atomic layer deposition (ALD) on the sample to completely coat the graphene for electrical insulation and structural reinforcement. (F) A transmission electron microscope (purple) is used to drill a single nanopore, 20 nm, in the center of the 1 µm hole.

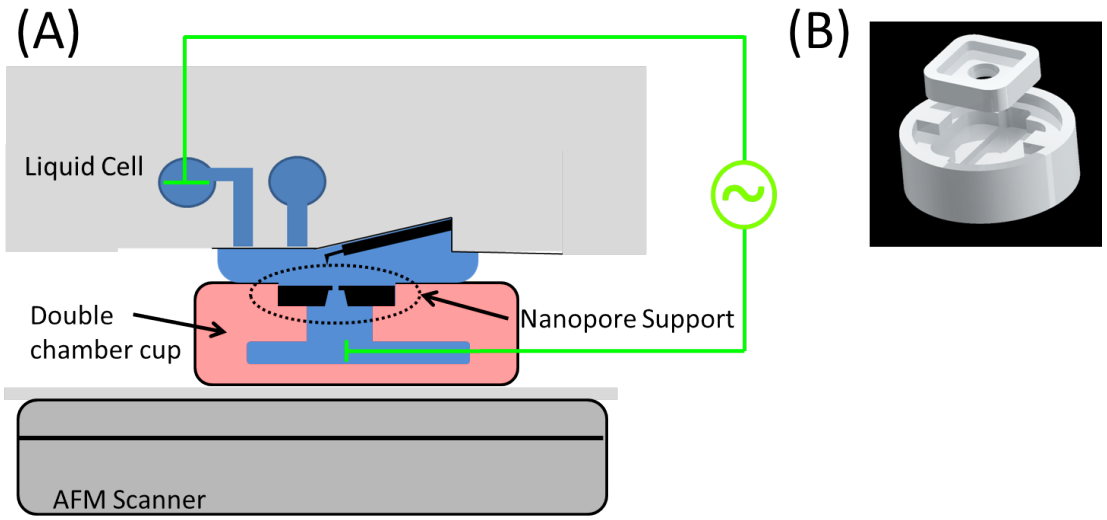

FIGURE 5.2 Schematic of the integrated AFM system for imaging and conductance measurements. (A) The nanopore support is glued into the top chamber of the double chamber cup such that the only liquid path connecting the chambers is through the nanopore. The double chamber cup (pink) is placed on the scanner head and the liquid cell with mounted cantilever is placed on top of the sample to allow for AFM imaging. Electrodes are connected to the bottom chamber though the double chamber cup and to the top solution through an open port in the liquid cell for measuring conductance activity. The electrodes can are fed to an amplifier and computer for analysis. (B) Schematic image of the double chamber cup design. The nanopore support fits into the top removable piece and set into the bottom piece. The bottom piece is filled with liquid creating an isolated chamber, accessible only through a nanopore. A liquid droplet is suspended between the nanopore support and the AFM liquid cell creating the other chamber.

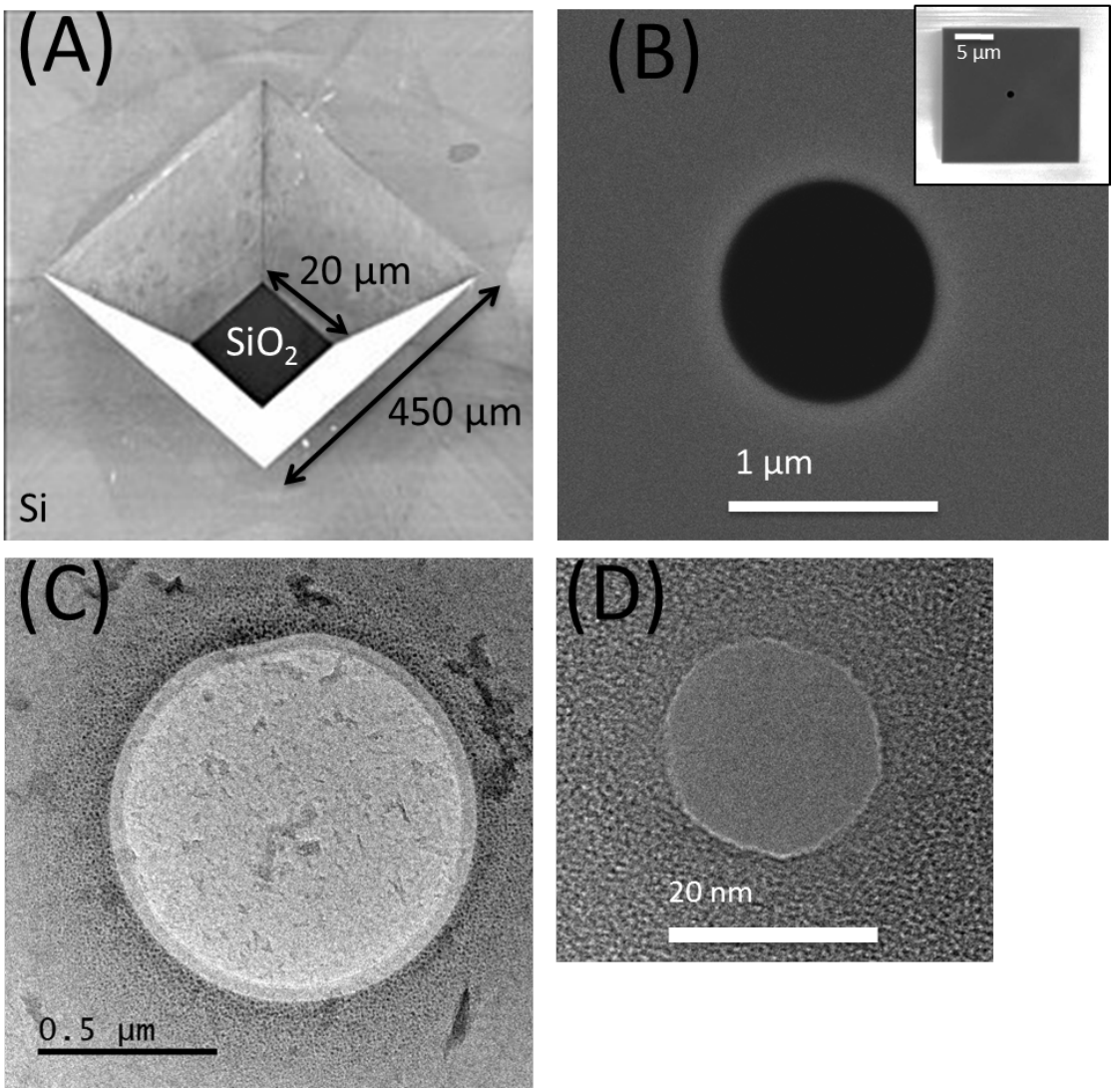

FIGURE 5.3 (A) SEM image of the backside of the starting substrate of Si and SiO_2 membrane (image adapted from AppNano). This image corresponds to the schematic in Fig. 5.1 A. (B) Top view SEM image of the drilled FIB 1 µm hole. Inset is a zoomed out SEM of the same hole. The 20 µm x 20 µm SiO_2 area is clearly visible in SEM due to the 200 nm thickness. This image corresponds to the schematic in Fig. 5.1 B. (C) Top view TEM image of the drilled FIB 1 µm hole covered with a layer of graphene. The graphene completely covers the 1 µm area and no pin holes or gaps are observed. In TEM thicker regions appear as darker spots. The darker spot seen here are likely areas of multilayer graphene. This image corresponds to the schematic in Fig. 5.1 D. (D) Top view TEM image of a single drilled 20 nm pore in the graphene/Al_2O_3 membrane. This image corresponds to the schematic in Fig. 5.1 F.

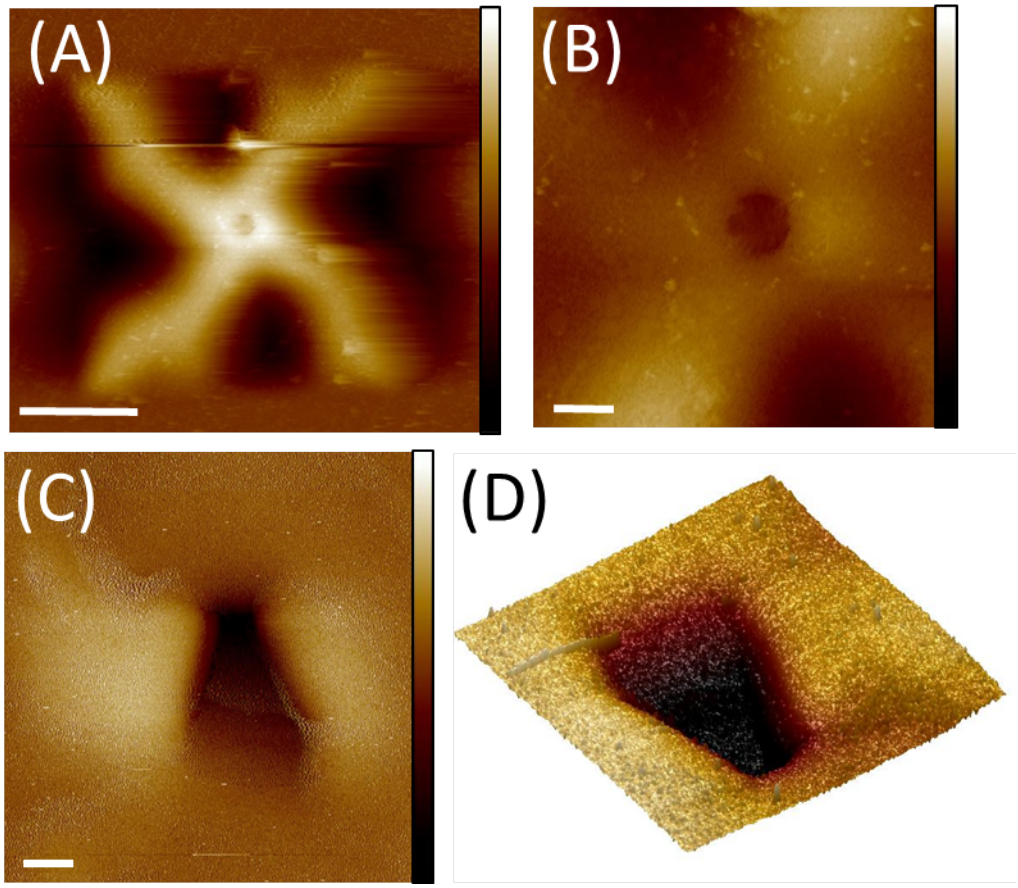

FIGURE 5.4 Progressive AFM height images in tapping mode of a complete nanopore support. (A) AFM image showing the complete 20 µm x 20 µm SiO_2 area. The large height variance of this area aids in located the area of the FIB hole which can be seen as the depressed circle in the center of the square. scale bar = 5 µm, height color scale = 294 nm (B) AFM image of the FIB hole. The image shows uniform coverage by the graphene/Al_2O_3.scale bar = 1 µm, height color scale = 208 nm (C) AFM image of a single nanopore drilled in the graphene/Al_2O_3. The rectangular shape of the nanopore is an effect of the shape of the tip and imaging into the pore area. scale bar 20 nm, height color scale = 17.8 nm. (D) 3D view of the nanopore shown in (C). Image size is 125 nm x 122 nm

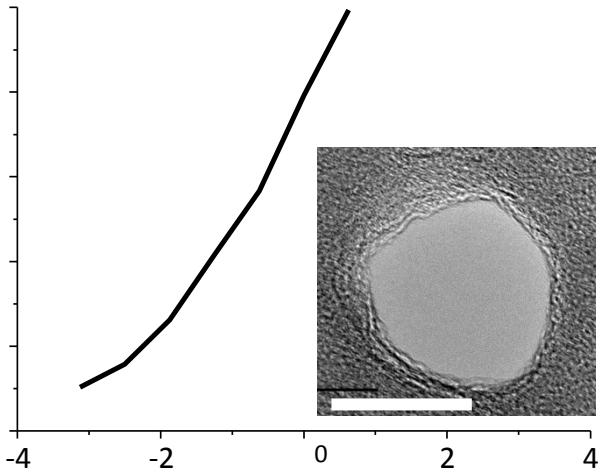

FIGURE 5.5 I-V curve of an open nanopore shown in inset TEM image measuring ~25 nm and conductance of 2765 nS. Scale bar = 20 nm.

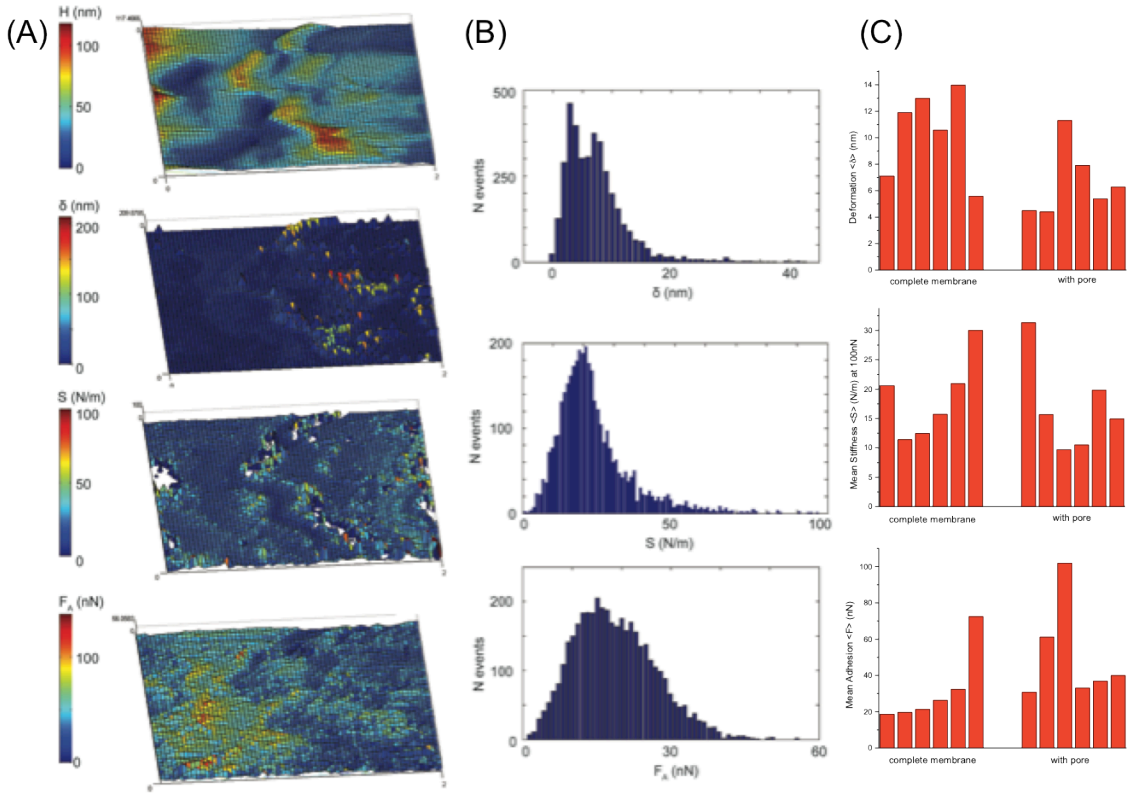

FIGURE 5.6 Results from AFM force mapping of nanopore samples. (A) Contour map of the height and mechanical properties of 2 μm area surrounding the nanopore of a single sample. Top to bottom are (i) the sample deformation (δ), ii) the sample stiffness (dF/dδ) at F=100 nN load and iii) the adhesion force between the AFM tip and the sample. (B) Histograms of the value distribution for the property maps in (A). (C) The mean value for samples without (n=5) and with (n=5) nanopores for each property. There is a weak correlation between the topographical features in the samples and their mechanical properties. The elevated topographical features observed in the AFM images, attributed to contamination, have somewhat distinguishable deformation and stiffness as compared to the flatter cleaner regions. This would suggest that the contamination is either softer or harder than the underlying graphene/Al_2O_3 layer. However, this correlation is lost when observed at it in detail. Regions of larger sample deformation (soft regions) do not coincide with regions of decreased stiffness. The adhesion force map shows non-uniform characteristics across the sample, does not correlate with the topographical features. All these non-uniform mechanical and topographical properties suggest the presence of impurities with similar mechanical properties as the underlying graphene/Al_2O_3 surface. Analysis of the mechanical properties evaluated before and after TEM drilling show that there is no statistically significant difference at the 0.05 level (C), thus indicating that the cavity of the nanopore does not alter the mechanical properties of the supporting membrane.

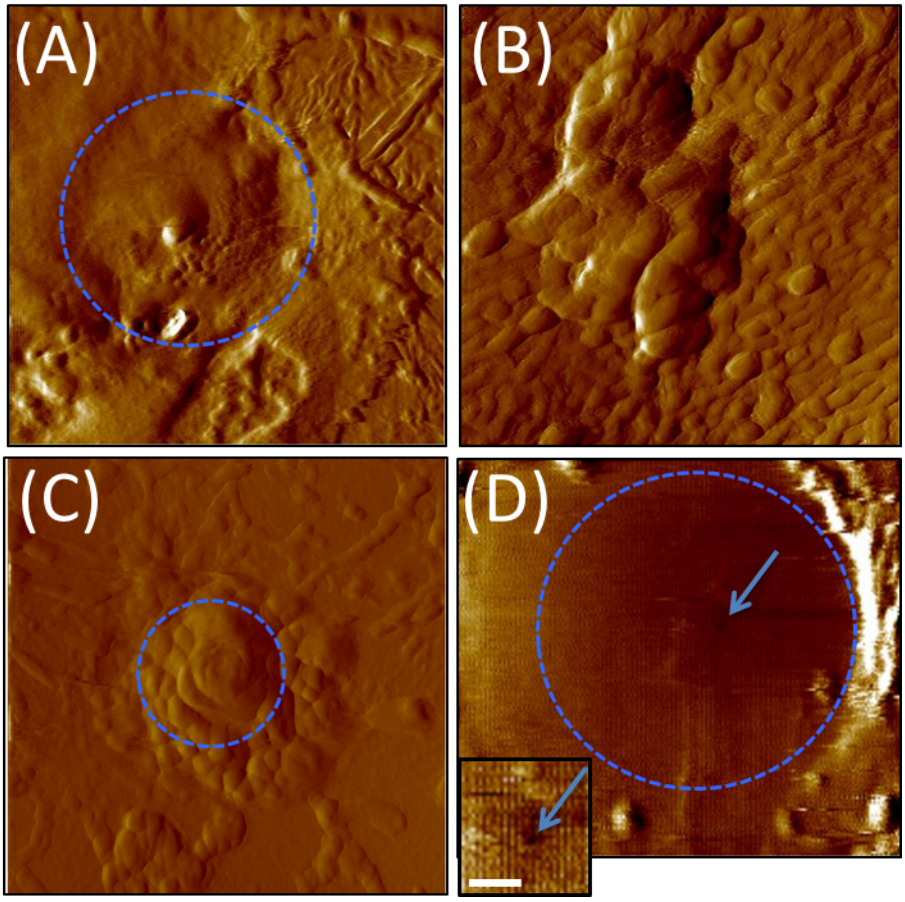

FIGURE 5.7 AFM deflection images in contact mode of the 1 μm area (blue circles) containing the drilled nanopore. (A-C) shows examples of the contamination depositions seen in some samples after the TEM drilling of the nanopore. Image sizes 1.7 μm, 3.2 μm, and 3.5 μm respectively. (D) AFM image, 3.5 μm image size, of a nanopore support free from deposition. In samples, free from depositions the 1 μm area is easily identifiable and the drilled nanopore can be located. Blue arrows show the nanopore. Inset is zoomed in image of the nanopore, scale bar of inset = 50 nm.

CHAPTER 6

Integrated Atomic Force Microscope and Electrical Recording System: Simultaneous 3D Imaging and Electrical Conductance Measurement of Membrane Ion Channels

6.1 Abstract

Atomic Force Microscopy is an effective technique for structural studies of membrane proteins in biologically relevant fluidic environments. AFM has been used to resolve the three-dimensional (3D) surface structure of ion channels, the key structures that control the activity of all living systems. The activity of ion channels are studied by various techniques, including patch clamp, free standing lipid bilayers, droplet interface bilayers, and supported lipid bilayers. In spite of several Nobel prizes in the study of the 3D structure and the activity of ion channels, direct linkage of the 3D molecular structure, in real time to the activity of these channels has remained elusive. Presented is a design and proof of principle for an integrated atomic force microscope for simultaneous imaging and channel conductance measurements. The membrane used in this study was derived from Sf9 cells expressing a high level of Cx26 hemichannels. Membrane plaques were deposited over a nanopore substrate in a custom-designed double chamber with a defined pore. Data presented here shows the conductance of an ensemble of hemichannels when the membrane is on the supported system and a loss of channel

conductance only after membrane removal by force-dissection. The system demonstrates capability for simultaneous data collection of AFM images on an active Sf9 membrane and corresponding conductance changes.

6.2 Introduction

Atomic Force Microscopy (AFM)[1] has been widely used in biomedicine and life sciences to study the structure of biological entities ranging from whole cells to single proteins.[2]–[8] Based on the physical interaction of a nano-sized tip on a cantilever and the sample surface, AFM is uniquely capable of both <1 nm lateral resolution and imaging in air or liquid without the fixing of biological material.[9]–[11] This is particularly beneficial to the study of cell membranes and membrane proteins,[3], [8], [12]–[19] which when studied at the molecular level by other methods require treatments (freezing, isolation, dehydration, or staining) that may induce conformational changes. AFM has been extensively used to resolve the structure of many pathologically significant ion channels in supported membranes. Ion channels have further been examined using AFM to observe conformational changes in real time, in the presence of analytes, and between selected mutants.[17], [18], [20]–[24]

While the structure of ion channels has been resolved by AFM, the electrophysiology of these channels has typically been studied separately by black lipid membranes (BLM) or patch clamp.[25]–[35] Using separate techniques presents complications in correlating structure and activity results due to differences in sample

preparation, environmental conditions, and experimental timing.[36] Studying the simultaneous and dynamic structure and activity of ion channels would have major implications in understanding biological function and pathophysiology.[11] Ion channels are essential to the control of basic functions in all living systems. Defects in ion channels, therefore, lead to a vast array of illnesses, diseases, and disorders. For example, ion channels have been linked to the pathology of neurodegeneration, deafness, heart failure, and substance abuse. A system that correlates the structural change of ion channels to its dysfunction would have a major impact on understanding and addressing these issues.

The discourse in linking structural data to activity data has been especially present in the field of hemichannels and gap junctions. Two hemichannels from opposing cells pair to facilitate cell-cell communication through the formation of gap junctions. The intercellular gap formed allows for the exchange of ions and small metabolites. Hemichannels are known to cluster together in the membrane, forming high density areas called plaques.[36] For gap junctions and hemichannels, discrepancies between structure and activity investigations have been attributed to methodological differences in investigative techniques–the conformational flexibility of species in electrophysiology studies is unavailable in fixed systems such as EM–and innate differences between isolated hemichannels, unpaired hemichannels, and docked hemichannels.[36] A technique that maintains a single methodology and degrees of freedom for a single channel type would address these challenges.

Recently, solid state nanopore samples have emerged as a prominent substrate for the study of ion channel conductance, protein translocation events, and DNA sequencing

readings.[37]–[44] Nanopores made in graphene membranes have been utilized due to their unique mechanical, thermal, and electrical properties.[37], [42], [43] Graphene nanopores are easily and efficiently drilled using transmission electron microscopy.[43], [45]–[48] Atomic layering of Al_2O_3 on a suspended layer of graphene provides electrical insulation while minimally increasing the thickness in a controlled fashion.[46], [47] Lipid bilayers have been shown to form a complete suspended layer across pores of various sizes, sealing the opening to prevent ionic flow through the pore.[38], [49], [50]

Here we present an integrated AFM system for simultaneous structural imaging and electrophysiological recording. High-resolution 3D conformational images are obtained, via AFM, while electrophysiological measurements (ionic conductance) are recorded, by BLM, under conditions most similar to the physiological environment. The model system used in this study consisted of purified Sf9 insect cell membrane plaques containing connexin26 (Cx26) hemichannels. Upon membrane deposition, a drop in pore ionic conductance was observed and structural images showed complete coverage of the 1 μm pore. The drop in conductance was attributed to the plaque sealing the large pore; any subsequent conductance originated solely from the hemichannels. The conductance values reported were under applied voltages of ± 50 mV. Hemichannel activity was manipulated by real time addition of Zn^{2+} ions, a known channel blocker. Conductance activity changes were recorded while simultaneously obtaining AFM structural images of the Sf9 plaques. Only after the Sf9 plaque was force dissected by AFM, to clear the solid state pore, was the ensemble conductance value lost. Significant progress is presented towards obtaining high resolution images of membranes and membrane proteins correlated with activity readings in this proof of principle study.

6.3 Experimental Methods

Silicon dioxide membranes (SiO_2) were purchased from AppNano. Silicon dioxide membranes were 200 nm thick on a 300 μm thick silicon substrate. The silicon substrate was etched by AppNano to create a 20 μm x 20 μm window of suspended SiO_2 membrane that expanded to 450 μm x 450 μm opening on the backside of the silicon (Fig 6.1 A). Single layer CVD graphene deposited on 20 μm thick Cu foil 2'' x 2'' was obtained from Graphene Supermarket. A Quanta™ 3D FEG focused ion beam (FIB) was used to drill through the SiO_2 suspended membrane (Calit2 Microscopy Center, UC Irvine). Either iron(III) chloride hexahydrate (FeCl3 • 6H2O) ≥ 98% solution (Sigma Aldrich) or Copper Etch APS-100 (Transene Co.) was used to dissolve the Cu substrate of the graphene. Atomic layer deposition (ALD) of 5 nm of Al_2O_3 was performed using a GEMSTAR™ Benchtop Atomic Layer Deposition (ALD) Process System (Wanunu Nanoscale Biophysics lab, Northeastern University) or the Beneq TFS200 Atomic Layer Deposition (Nano3 Facility, UCSD). A transmission electron microscope (JEOL 2010, Japan) from the Nanomaterials Instrumentation Facility at Northeastern University was used for drilling through graphene/Al_2O_3 membrane layer. AFM imaging was completed using a Bruker Multimode Nanoscope IV system with silicon nitride cantilevers (k = 0.08N/m) and silicon cantilevers (k = 3.0N/m). Conductance measurements were completed using an in-house designed (Brian Meckes, Lal Lab, UCSD) and fabricated (Machine Shop UC San Diego) double chamber cup system (Fig 6.1 B), AFM liquid cell,

Ag/AgCl wire electrodes, 1 M KCl as the electrolyte solution, a Dagon 3900A patchclamp amplifier (Dagon Corporation Minneapolis, MN), and Nanoscope IV software. Ecoflex® Supersoft 5 silicone cured rubber was used as an insulating sealant of the nanopore sample in the double chamber cup. Membranes containing Cx26-V5-His_6 hemichannels were purified from baculovirus infected Sf9 insect cells as described by Ambrosi et al.[51] A 0.1 M $Zn(NO_3)_2$ solution was used for blocking of the SF9 channels. 1,2-diphytanoyl-sn-glycero-3-phosphocholine lipids were purchased from Avanti Polar Lipids (Alabaster, AL).

The fabrication process of the nanopore support system is described in detail in Chapter 5 (see Fig. 5.1). Briefly, a layer of graphene is deposited over a 1 μm hole in a 200 nm thick membrane of silicon dioxide. 5 nm of Al_2O_3 is deposited on the graphene by atomic layer deposition. A nanopore (~20 nm) is drilled through the graphene/Al_2O_3 by transmission electron microscopy (Fig. 6.1A). This nanopore sample is set into the double chamber cup (Fig. 6.1B), sealed with Ecoflex® Supersoft 5 silicone cured rubber, and filled with buffer solution. Purified Sf9 membrane preparations were deposited in a HEPES buffer (pH 7.4, 10 mM) with serine protease inhibitors (PMSF 1mM) directly on the solid state membrane surface.[51]

Sf9 plaques were deposited on the nanopore surface mounted in the double chamber cup and allowed to settle for 45 min to 1 h. For Sf9 membrane deposition, 30 μL of pretreatment solution was first deposited followed by 10 μL of the plaque containing solution. The droplet of solution was rinsed by gentle solution replacement with the 1M KCl buffer. The double chamber cup was set on the scanner head of the AFM. The area

containing the nanopore, a 20 μm x 20 μm area of 200 nm thick SiO_2 (see Chap. 4 Fig 4.4 A), was aligned under the cantilever tip in an optical system.

Conductance levels of the hemichannels were recorded using a National Instruments DAC with a custom LabView 8.0 program and the Dagon amplifier under applied voltages of ± 50 mV. 4 μL of 0.1 M $Zn(NO_3)_2$ was added during live conductance recording to block the channel activity. When blockage was achieved, the AFM was engaged and, in contact mode, the area of the 1 μm hole covered with plaques was imaged. Force dissection of the plaques was performed while simultaneous conductance recordings were taken.

6.4 Results

6.4.1 Suspended Sf9 Plaque Shows Conductance and Zn^{2+} Sensitivity Over a Solid State Pore

Sf9 plaques containing Cx26 channels were deposited on a substrate containing a 1 μm pore (Fig. 6.2 A). The current across the pore, free of plaque, in 1 M KCl saturated when ramped over ±100 mV (Fig 6.2 B). The exact conductance could not be determined because the recording system immediately reached its maximum measurable current. Conductance of the pore after Sf9 with Cx26 deposition was measured at 300 pA and −800 pA under applied voltage of 50 mV and -50 mV respectively (Fig 6.3 A, B). With

no applied voltage, zero current was observed (data not shown). The conductance value of the ensemble of Cx26 channels in the plaque over the pore was dependent on voltage bias. The conductance of the plaque was measured at 6 nS and 16 nS under applied voltage biases of +50 mV and -50 mV respectively. These values were stable over several minutes.

4 μL of 0.1 M $Zn(NO_3)_2$ was added through an open port in the liquid cell during live recording to test the inhibition of active Cx26 channels. After several minutes, the current jumped to 0 pA and remained stable across ± 50 mV bias potential for the duration of the experiment (Fig. 6.3 C).

6.4.2 Simultaneous AFM Imaging and Sf9 Plaque Activity

The activity of the suspended Sf9 plaques containing Cx26 in the presence of Zn^{2+} remained stable at 0 pA while engaging the AFM and throughout imaging in normal contact mode. The interaction force of the AFM can be minimized such that it does not interfere with the activity or structure of membrane proteins. The AFM images in Fig. 6.4, of the suspended plaque over the 1 μm pore show complete coverage. Fig. 6.4 C shows the surface of the plaque at higher resolution and displays no indication of gaps in the plaque suggesting activity readings are likely due to Cx26 hemichannels, not defects in the coverage of the pore. Individual Cx26 channels were not resolved in this image.

To remove the Zn^{2+} from the Cx26 channels, buffer solution was exchanged several times through an open port on the AFM liquid cell. Several minutes after the

solution exchange the current value jumped to -2000 pA (Fig. 6.5 A). Possible reasons for this jump in current may include: the exchange of solution "reopened" the Cx26 channels to conducting ions, cleared stacked plaques, partially damaged the plaque coverage of the pore, or a combination of these. AFM images shown in Fig 6.5 B and C, obtained after the solution exchange show no observable change in the pore coverage of the plaque from Fig 6.4, suggesting no significant damage occurred.

6.4.3 A Solid State Pore Can be Cleared by Force Dissection of Sf9 Plaque

Large contact forces were applied via AFM imaging while continuing to simultaneously record the ionic activity of the hemichannel ensemble (Fig. 6.5 A, C)). The plaques were completely removed from the pore area by force dissection (Fig 6.5 A, C), during which time the current value recorded increased from -2000 pA to saturation at -9000 pA under a voltage bias of -50mV (Fig 6.5 A). This jump indicates a loss in channel conductance activity, returning instead to the open pore saturation observed before membrane deposition. After force dissection, the removal of the plaques is clearly visible as a smooth, cleaned square area around the pore as shown in in Fig 6.5 C. This clearing of the plaque and current saturation is an indication of destruction of the plaque covering the pore. The deposited plaque had a height of 6.3 nm, measured at the edge of the dissected area, as shown in Fig. 6.6 A. This height is comparable to a single Sf9

plaque with Cx26 hemichannels imaged on mica, shown in a sectioned height profile in Fig. 6.6 B.

6.5 Discussion

We have developed an integrated AFM system to simultaneously image membranes and membrane proteins while measuring their activity, through electrical recording. The functionality and design of the system is described elsewhere (see Chapter 5). The practicality and benefit of this system was demonstrated using Sf9 plaques containing Cx26 as model membranes over a defined pore substrate.

Mutations of Cx26, encoded by the GJB2 gene, is linked to hearing impairment, deafness, and for some mutations hyperkerototic skin disorders.[52], [53] Understanding the activity and function of the Cx26 hemichannel and gap junction is essential to the treatment of these disorders. The conductance of Cx26 has been widely reported from patch clamp studies of devitellinized oocytes.[54]–[57] One study of Cx26 conductance has also been reported in a Sf9 system suspended over pores of several microns.[58, p. 34] Despite the extensive studies of Cx26, and related hemichannels, the activity and validity of many of these studies is debated.[36], [59]–[62] We choose the Sf9 with Cx26 system as a model membrane in our integrated AFM due to the structural integrity of the Sf9 membranes and the importance of relating Cx26 structure to activity.

The reported electrical activity, observed in patch clamp techniques and BLM-like setups, is inherently devoid of all pertinent information since these are structurally

blind techniques. Only in analysis are these results linked to conformational data gathered separately via AFM, EM, X-ray crystallography, or NMR. By pairing the imaging capabilities of AFM to find the structure of individual hemichannels or other membrane proteins and recording their conductance, a more accurate single channel conductance value may be obtained. The current values observed in this study are a collective value of the activity of many Cx26 active channels across the pore area. We showed that Sf9 plaques can be imaged by an AFM tip across the pore without disruption to the observed activity or plaque coverage (Fig. 6.3 and Fig. 6.4). Additionally, we confirmed the presence of suspended plaques across the electrical recording path. The small scan sizes (300 nm) and repeated imaging of the suspended plaques (Fig 6.4 C) suggest high resolution imaging of individual channels is possible. The images of complete plaques across the pore area imply current values are a result of hemichannels not leakage through incomplete plaque coverage.

Zinc is utilized in many ion channel studies to test the presence and functioning of Ca^{2+} sensitive ion channels.[63] Ca^{2+} is known to alter the structure and behavior of Cx43 and Cx26.[15], [33], [52], [64] Therefore, to induce a measurable activity or structural change Zn^{2+} was added to the conducting hemichannel system. The conductance changes of the Sf9 plaques in response to addition and removal of Zn^{2+} ions was consistent with the expected behavior of ion channels sensitive to Zn^{2+} blocking. In the Sf9 system used here, ion channels other than Cx26 may also be present and contributing to this behavior. The system does not distinguish between conductance due to Cx26 and conductance due to other channels. Regardless, the drop of current to zero upon addition of Zn^{2+} and the reoccurrence of conductance activity after the solution exchange, removing Zn^{2+} ions,

supports the conclusion that functional channel measurements are obtained in our integrated system. The removal of the plaque by force dissection and subsequent loss of activity further suggests the plaque had sealed the pore.

The differences of conductance values of the Cx26 channels as reported here under positive and negative biases is likely the result of a preferential orientation of the hemichannels.[54] The hemichannels within a single plaque have one orientation, however plaque orientation upon deposition likely varies. The Cx26 is more sensitive to negative voltage bias. The conductance of a single Cx26 hemichannel, although debated, has been reported in the range of 370 pS.[54] Assuming this value for a single open hemichannel (half a gap junction), we deduce an average 59 open and functioning channels in the pore area at -50 mV. Hemichannels have been reported to occupy <1% of the cell surface of hepatocytes.[65] Therefore, the maximum number of hemichannels in the pore area is 4000, assuming the hemichannels are in an ordered lattice with d=90 Å and the plaque is perfectly stretched flat across the pore.[64]–[66] However, in this system, plaques were deposited in a large concentration and left to settle for 45 mins, likely allowing multiple layers of plaque to build up across the pore. Only the areas with a single layer of plaque bilayer across the pore are likely to contain functional measureable channels. The AFM image in Fig. 6.5 A shows that the plaque is not stretched flat across the pore, but rather sags into the pore area as much as 250 nm deep. This sagging of the plaque likely has a narrowing effect on the area of plaque available for conducting Cx26 channels. The plaque fragments likely build up along the sides of the pore, further limiting the number of functional channels. The 59 functional Cx26 with a 90 Å lattice constant[65] under -50 mV applied voltage indicates 0.6% of the pore

area contains channels contributing to the measured conductance. Future investigations will aim to use the nanopore substrates to minimize sagging of the plaque and use lower concentrations of plaque fragments to prevent stacking. The aim of this effort will be to resolve individual channels in the suspended plaque and achieve correlation to channel distribution and a single open and closed channel conductance value.

6.6 Conclusions

Currently structure and activity of membrane proteins are investigated separately under varying conditions, risking incomplete or inaccurate corollary results. The system presented here incorporates a single pore substrate into the AFM interface to localize the imaging and activity measurement of a model ion channel containing membrane. To date, the structure of ion channels has not been directly correlated to their activity. Our system has simultaneously produced AFM images of Sf9 plaques containing Cx26 hemichannels with real time channel activity across the membrane. This system can further be applied to study membrane proteins by depositing lipid bilayers across small nanopores. The precise structure-activity correlation of membrane conducting proteins is essential to understanding normal biological signaling. Additionally, linking the dysfunctional activity of toxic channels to their exact structure change will open new research paths for the understanding of neurodegenerative disorders, addictions, and therapeutic development and evaluation.

6.7 Acknowledgements

I would like to acknowledge my co-authors of this paper. Chapter 6, in part, is currently being prepared for submission for publication of the material, Connelly, L., Meckes, B., Larkin, J., Gilman, A., Wanunu, M.,, Lal, R. No authors have competing interests.

This research is supported by NIH grants R01 DA025296-01, R01 AG028709-01, and R01 DA024871-10A1. The Wanunu Lab of Nanoscale Biophysics at Northeastern University in Boston, Ma is thanked for their aid and resources used in the preparation of the nanopore supports. Dr. Paul Hansma, Brian Meckes, and the Machine Shop at UCSD and is thanked for their assistance in the design and fabrication the double chamber cup. Cinzia Ambrosi and Gina Sosinsky, UCSD, are thanked for providing the Sf9 membrane plaques used in this study.

6.8 References

[1] G. Binnig, C. F. Quate, and C. Gerber, “Atomic Force Microscope,” *Phys. Rev. Lett.*, vol. 56, no. 9, pp. 930–933, Mar. 1986.

[2] D. P. Allison, P. Hinterdorfer, and W. Han, “Biomolecular force measurements and the atomic force microscope,” *Curr. Opin. Biotechnol.*, vol. 13, no. 1, pp. 47–51, Feb. 2002.

[3] R. B. Best and J. Clarke, “What can atomic force microscopy tell us about protein folding?,” *Chem. Commun. Camb. Engl.*, no. 3, pp. 183–192, Feb. 2002.

[4] A. Engel and D. J. Müller, "Observing single biomolecules at work with the atomic force microscope," *Nat. Struct. Biol.*, vol. 7, no. 9, pp. 715–718, Sep. 2000.

[5] J. K. H. Hörber and M. J. Miles, "Scanning Probe Evolution in Biology," *Science*, vol. 302, no. 5647, pp. 1002–1005, Nov. 2003.

[6] M. Plomp, M. K. Rice, E. K. Wagner, A. McPherson, and A. J. Malkin, "Rapid visualization at high resolution of pathogens by atomic force microscopy: structural studies of herpes simplex virus-1," *Am. J. Pathol.*, vol. 160, no. 6, pp. 1959–1966, Jun. 2002.

[7] Z. Shao, J. Yang, and A. P. Somlyo, "Biological atomic force microscopy: from microns to nanometers and beyond," *Annu. Rev. Cell Dev. Biol.*, vol. 11, pp. 241–265, 1995.

[8] R. Lal and S. A. John, "Biological applications of atomic force microscopy," *Am. J. Physiol. - Cell Physiol.*, vol. 266, no. 1, pp. C1–C21, Jan. 1994.

[9] D. Fotiadis, S. Scheuring, S. A. Müller, A. Engel, and D. J. Müller, "Imaging and manipulation of biological structures with the AFM," *Micron*, vol. 33, no. 4, pp. 385–397, Jan. 2002.

[10] P. K. Hansma, V. B. Elings, O. Marti, and C. E. Bracker, "Scanning tunneling microscopy and atomic force microscopy: application to biology and technology," *Science*, vol. 242, no. 4876, pp. 209–216, Oct. 1988.

[11] R. Lal and M. F. Arnsdorf, "Multidimensional atomic force microscopy for drug discovery: a versatile tool for defining targets, designing therapeutics and monitoring their efficacy," *Life Sci*, vol. 86, pp. 545–62, Apr. 2010.

[12] A. F. Oberhauser, P. K. Hansma, M. Carrion-Vazquez, and J. M. Fernandez, "Stepwise unfolding of titin under force-clamp atomic force microscopy," *Proc. Natl. Acad. Sci. U. S. A.*, vol. 98, no. 2, pp. 468–472, Jan. 2001.

[13] M. L. Bennink, D. N. Nikova, K. O. van der Werf, and J. Greve, "Dynamic imaging of single DNA–protein interactions using atomic force microscopy," *Anal. Chim. Acta*, vol. 479, no. 1, pp. 3–15, Mar. 2003.

[14] N. Almqvist, R. Bhatia, G. Primbs, N. Desai, S. Banerjee, and R. Lal, "Elasticity and adhesion force mapping reveals real-time clustering of growth factor receptors and associated changes in local cellular rheological properties," *Biophys. J.*, vol. 86, no. 3, pp. 1753–1762, Mar. 2004.

[15] J. Thimm, A. Mechler, H. Lin, S. Rhee, and R. Lal, "Calcium-dependent Open/Closed Conformations and Interfacial Energy Maps of Reconstituted Hemichannels," *J. Biol. Chem.*, vol. 280, no. 11, pp. 10646–10654, Mar. 2005.

[16] J. H. Hoh, G. E. Sosinsky, J. P. Revel, and P. K. Hansma, "Structure of the extracellular surface of the gap junction by atomic force microscopy," *Biophys. J.*, vol. 65, no. 1, pp. 149–163, Jul. 1993.

[17] J. H. Hoh, R. Lal, S. A. John, J. P. Revel, and M. F. Arnsdorf, "Atomic force microscopy and dissection of gap junctions," *Science*, vol. 253, no. 5026, pp. 1405–1408, Sep. 1991.

[18] R. Lal, "Imaging molecular structure of channels and receptors with an atomic force microscope," *Scanning Microsc. Suppl.*, vol. 10, pp. 81–95; discussion 95–96, 1996.

[19] R. Lal, H. Kim, R. M. Garavito, and M. F. Arnsdorf, "Imaging of reconstituted biological channels at molecular resolution by atomic force microscopy," *Am. J. Physiol.*, vol. 265, no. 3 Pt 1, pp. C851–856, Sep. 1993.

[20] L. Connelly, H. Jang, F. T. Arce, R. Capone, S. A. Kotler, S. Ramachandran, B. L. Kagan, R. Nussinov, and R. Lal, "Atomic force microscopy and MD simulations reveal pore-like structures of all-D-enantiomer of Alzheimer's β-amyloid peptide: relevance to the ion channel mechanism of AD pathology," *J. Phys. Chem. B*, vol. 116, no. 5, pp. 1728–1735, Feb. 2012.

[21] L. Connelly, H. Jang, F. T. Arce, S. Ramachandran, B. L. Kagan, R. Nussinov, and R. Lal, "Effects of point substitutions on the structure of toxic Alzheimer's β-amyloid channels: atomic force microscopy and molecular dynamics simulations," *Biochemistry (Mosc.)*, vol. 51, no. 14, pp. 3031–3038, Apr. 2012.

[22] H. Lin, R. Bhatia, and R. Lal, "Amyloid beta protein forms ion channels: implications for Alzheimer's disease pathophysiology," *FASEB J*, vol. 15, pp. 2433–44, Nov. 2001.

[23] A. Quist, "Amyloid ion channels: A common structural link for protein-misfolding disease," *Proc. Natl. Acad. Sci.*, vol. 102, pp. 10427–10432, 2005.

[24] H. Lin, Y. J. Zhu, and R. Lal, "Amyloid beta protein (1-40) forms calcium-permeable, Zn2+-sensitive channel in reconstituted lipid vesicles," *Biochemistry (Mosc.)*, vol. 38, no. 34, pp. 11189–11196, Aug. 1999.

[25] R. Capone, H. Jang, S. A. Kotler, L. Connelly, F. Teran Arce, S. Ramachandran, B. L. Kagan, R. Nussinov, and R. Lal, "All-d-Enantiomer of beta-Amyloid Peptide Forms Ion Channels in Lipid Bilayers," *J Chem Theory Comput*, vol. 8, pp. 1143–1152, Mar. 2012.

[26] R. Capone, M. Mustata, H. Jang, F. T. Arce, R. Nussinov, and R. Lal, "Antimicrobial protegrin-1 forms ion channels: molecular dynamic simulation, atomic force microscopy, and electrical conductance studies," *Biophys J*, vol. 98, pp. 2644–52, Jun. 2010.

[27] R. Capone, H. Jang, S. A. Kotler, B. L. Kagan, R. Nussinov, and R. Lal, "Probing structural features of Alzheimer's amyloid-β pores in bilayers using site-specific amino acid substitutions," *Biochemistry (Mosc.)*, vol. 51, no. 3, pp. 776–785, Jan. 2012.

[28] B. L. Kagan, R. Azimov, and R. Azimova, "Amyloid Peptide Channels," *J. Membr. Biol.*, vol. 202, pp. 1–10, 2004.

[29] N. Arispe, H. B. Pollard, and E. Rojas, "Calcium-independent K(+)-selective channel from chromaffin granule membranes," *J Membr Biol*, vol. 130, pp. 191–202, Nov. 1992.

[30] N. Arispe, H. B. Pollard, and E. Rojas, "Giant multilevel cation channels formed by Alzheimer disease amyloid beta-protein [A beta P-(1-40)] in bilayer membranes," *Proc Natl Acad Sci U A*, vol. 90, pp. 10573–7, Nov. 1993.

[31] N. Arispe, E. Rojas, and H. B. Pollard, "Alzheimer disease amyloid beta protein forms calcium channels in bilayer membranes: blockade by tromethamine and aluminum," *Proc Natl Acad Sci U A*, vol. 90, pp. 567–71, Jan. 1993.

[32] J. Kronengold, E. B. Trexler, F. F. Bukauskas, T. A. Bargiello, and V. K. Verselis, "Single-channel SCAM identifies pore-lining residues in the first extracellular loop and first transmembrane domains of Cx46 hemichannels," *J. Gen. Physiol.*, vol. 122, no. 4, pp. 389–405, Oct. 2003.

[33] R. L. Chappell, J. Zakevicius, and H. Ripps, "Zinc Modulation of Hemichannel Currents in Xenopus Oocytes," *Biol. Bull.*, vol. 205, no. 2, pp. 209–211, Oct. 2003.

[34] K. A. Schalper, N. Palacios-Prado, J. A. Orellana, and J. C. Sáez, "Currently used methods for identification and characterization of hemichannels," *Cell Commun. Adhes.*, vol. 15, no. 1, pp. 207–218, May 2008.

[35] F. Lehmann-Horn and K. Jurkat-Rott, "Voltage-Gated Ion Channels and Hereditary Disease," *Physiol. Rev.*, vol. 79, no. 4, pp. 1317–1372, Jan. 1999.

[36] M. Yeager and A. L. Harris, "Gap junction channel structure in the early 21st century: facts and fantasies," *Curr. Opin. Cell Biol.*, vol. 19, no. 5, pp. 521–528, Oct. 2007.

[37] B. M. Venkatesan and R. Bashir, "Nanopore sensors for nucleic acid analysis," *Nat. Nanotechnol.*, vol. 6, no. 10, pp. 615–624, Oct. 2011.

[38] A. P. Quist, A. Chand, S. Ramachandran, C. Daraio, S. Jin, and R. Lal, "Atomic force microscopy imaging and electrical recording of lipid bilayers supported over microfabricated silicon chip nanopores: lab-on-a-chip system for lipid membranes and ion channels," *Langmuir*, vol. 23, pp. 1375–80, Jan. 2007.

[39] M. Wanunu, J. Sutin, B. McNally, A. Chow, and A. Meller, "DNA Translocation Governed by Interactions with Solid-State Nanopores," *Biophys. J.*, vol. 95, no. 10, pp. 4716–4725, Nov. 2008.

[40] M. Wanunu and A. Meller, "Chemically Modified Solid-State Nanopores," *Nano Lett.*, vol. 7, no. 6, pp. 1580–1585, Jun. 2007.

[41] D. Branton, D. W. Deamer, A. Marziali, H. Bayley, S. A. Benner, T. Butler, M. Di Ventra, S. Garaj, A. Hibbs, X. Huang, S. B. Jovanovich, P. S. Krstic, S. Lindsay, X. S. Ling, C. H. Mastrangelo, A. Meller, J. S. Oliver, Y. V. Pershin, J. M. Ramsey, R. Riehn, G. V. Soni, V. Tabard-Cossa, M. Wanunu, M. Wiggin, and J. A. Schloss, "The potential and challenges of nanopore sequencing," *Nat. Biotechnol.*, vol. 26, no. 10, pp. 1146–1153, Oct. 2008.

[42] A. Bahrami, F. Doğan, D. Japrung, and T. Albrecht, "Solid-state nanopores for biosensing with submolecular resolution," *Biochem. Soc. Trans.*, vol. 40, no. 4, pp. 624–628, Aug. 2012.

[43] S. M. Iqbal and R. Bashir, "Nanoelectronic-Based Detection for Biology and Medicine," in *Springer Handbook of Automation*, Springer Berlin Heidelberg, 2009, pp. 1433–1449.

[44] A. Oukhaled, L. Bacri, M. Pastoriza-Gallego, J.-M. Betton, and J. Pelta, "Sensing proteins through nanopores: fundamental to applications," *ACS Chem. Biol.*, vol. 7, no. 12, pp. 1935–1949, Dec. 2012.

[45] A. J. Storm, J. H. Chen, X. S. Ling, H. W. Zandbergen, and C. Dekker, "Fabrication of solid-state nanopores with single-nanometre precision," *Nat. Mater.*, vol. 2, no. 8, pp. 537–540, Aug. 2003.

[46] B. M. Venkatesan, J. Polans, J. Comer, S. Sridhar, D. Wendell, A. Aksimentiev, and R. Bashir, "Lipid bilayer coated Al2O3 nanopore sensors: towards a hybrid biological solid-state nanopore," *Biomed. Microdevices*, vol. 13, no. 4, pp. 671–682, Aug. 2011.

[47] B. M. Venkatesan, D. Estrada, S. Banerjee, X. Jin, V. E. Dorgan, M.-H. Bae, N. R. Aluru, E. Pop, and R. Bashir, "Stacked graphene-Al2O3 nanopore sensors for sensitive detection of DNA and DNA-protein complexes," *ACS Nano*, vol. 6, no. 1, pp. 441–450, Jan. 2012.

[48] S. Banerjee, J. Shim, J. Rivera, X. Jin, D. Estrada, V. Solovyeva, X. You, J. Pak, E. Pop, N. Aluru, and R. Bashir, "Electrochemistry at the edge of a single graphene layer in a nanopore," *ACS Nano*, vol. 7, no. 1, pp. 834–843, Jan. 2013.

[49] P. Kongsuphol, K. B. Fang, and Z. Ding, "Lipid bilayer technologies in ion channel recordings and their potential in drug screening assay," *Sens. Actuators B Chem.*, vol. 185, pp. 530–542, Aug. 2013.

[50] X. Han, A. Studer, H. Sehr, I. Geissbühler, M. Di Berardino, F. K. Winkler, and L. X. Tiefenauer, "Nanopore Arrays for Stable and Functional Free-Standing Lipid Bilayers," *Adv. Mater.*, vol. 19, no. 24, pp. 4466–4470, 2007.

[51] C. Ambrosi, D. Boassa, J. Pranskevich, A. Smock, A. Oshima, J. Xu, B. J. Nicholson, and G. E. Sosinsky, "Analysis of four connexin26 mutant gap junctions and hemichannels reveals variations in hexamer stability," *Biophys. J.*, vol. 98, no. 9, pp. 1809–1819, May 2010.

[52] H. A. Sánchez, G. Meşe, M. Srinivas, T. W. White, and V. K. Verselis, "Differentially altered Ca2+ regulation and Ca2+ permeability in Cx26 hemichannels formed by the A40V and G45E mutations that cause keratitis ichthyosis deafness syndrome," *J. Gen. Physiol.*, vol. 136, no. 1, pp. 47–62, Jul. 2010.

[53] A. Murgia, E. Orzan, R. Polli, M. Martella, C. Vinanzi, E. Leonardi, E. Arslan, and F. Zacchello, "Cx26 deafness: mutation analysis and clinical variability," *J. Med. Genet.*, vol. 36, no. 11, pp. 829–832, Nov. 1999.

[54] T. M. Suchyna, J. M. Nitsche, M. Chilton, A. L. Harris, R. D. Veenstra, and B. J. Nicholson, "Different ionic selectivities for connexins 26 and 32 produce rectifying gap junction channels," *Biophys. J.*, vol. 77, no. 6, pp. 2968–2987, Dec. 1999.

[55] B. Nicholson, R. Dermietzel, D. Teplow, O. Traub, K. Willecke, and J. P. Revel, "Two homologous protein components of hepatic gap junctions," *Nature*, vol. 329, no. 6141, pp. 732–734, Oct. 1987.

[56] O. Traub, J. Look, R. Dermietzel, F. Brümmer, D. Hülser, and K. Willecke, "Comparative characterization of the 21-kD and 26-kD gap junction proteins in murine liver and cultured hepatocytes," *J. Cell Biol.*, vol. 108, no. 3, pp. 1039–1051, Mar. 1989.

[57] J. T. Zhang and B. J. Nicholson, "The topological structure of connexin 26 and its distribution compared to connexin 32 in hepatic gap junctions," *J. Membr. Biol.*, vol. 139, no. 1, pp. 15–29, Apr. 1994.

[58] O. Gassmann, M. Kreir, C. Ambrosi, J. Pranskevich, A. Oshima, C. Röling, G. Sosinsky, N. Fertig, and C. Steinem, "The M34A mutant of Connexin26 reveals active conductance states in pore-suspending membranes," *J. Struct. Biol.*, vol. 168, no. 1, pp. 168–176, Oct. 2009.

[59] A. L. Harris, "Emerging issues of connexin channels: biophysics fills the gap," *Q. Rev. Biophys.*, vol. 34, no. 03, pp. 325–472, 2001.

[60] M. M. Falk, L. K. Buehler, N. M. Kumar, and N. B. Gilula, "Cell-free synthesis and assembly of connexins into functional gap junction membrane channels," *EMBO J.*, vol. 16, no. 10, pp. 2703–2716, May 1997.

[61] L. K. Buehler, K. A. Stauffer, N. B. Gilula, and N. M. Kumar, "Single channel behavior of recombinant beta 2 gap junction connexons reconstituted into planar lipid bilayers," *Biophys. J.*, vol. 68, no. 5, pp. 1767–1775, May 1995.

[62] D. González, J. M. Gómez-Hernández, and L. C. Barrio, "Species specificity of mammalian connexin-26 to form open voltage-gated hemichannels," *FASEB J. Off. Publ. Fed. Am. Soc. Exp. Biol.*, vol. 20, no. 13, pp. 2329–2338, Nov. 2006.

[63] B. D. Winegar and J. B. Lansman, "Voltage-dependent block by zinc of single calcium channels in mouse myotubes.," *J. Physiol.*, vol. 425, no. 1, pp. 563–578, Jun. 1990.

[64] D. J. Müller, G. M. Hand, A. Engel, and G. E. Sosinsky, "Conformational changes in surface structures of isolated connexin 26 gap junctions," *EMBO J.*, vol. 21, no. 14, pp. 3598–3607, Jul. 2002.

[65] G. E. Sosinsky and B. J. Nicholson, "Structural organization of gap junction channels," *Biochim. Biophys. Acta BBA - Biomembr.*, vol. 1711, no. 2, pp. 99–125, Jun. 2005.

[66] N. Hirokawa and J. Heuser, "The inside and outside of gap-junction membranes visualized by deep etching," *Cell*, vol. 30, no. 2, pp. 395–406, Sep. 1982.

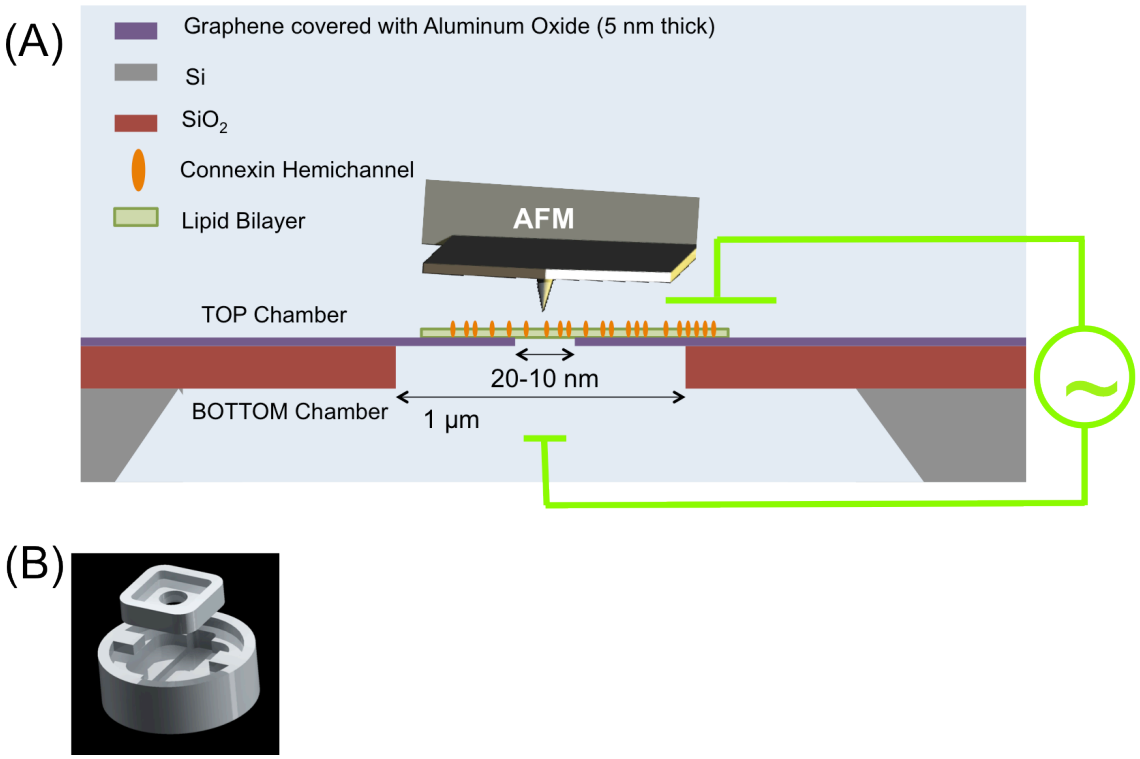

FIGURE 6.1 (A) Schematic of the design for the double chamber AFM setup for simultaneous AFM imaging and electrophysiology. The support substrate sample, is designed to have a ~20 nm nanopore in grapheme coated by in Al_2O_3 by ALD. The large pore in the SiO_2 membrane portion (red) is formed by FIB and base of the sample is Si. A lipid bilayer with connexin hemichannels or other ion channels is deposited over the pore area electrically isolating the two chambers. Open channels provide the only path for ionic conductance across the open pore area. Electrodes in both chambers record this activity during simultaneous imaging by an AFM tip. The entire sample is emerged in a buffer of choice. (B) Schematic of the double chamber cup placed on the scanner head of the AFM. The Si/SiO_2/graphene/Al_2O_3 sample is to be placed in the top chamber and glued into place, sealing off the liquid above and below the sample.

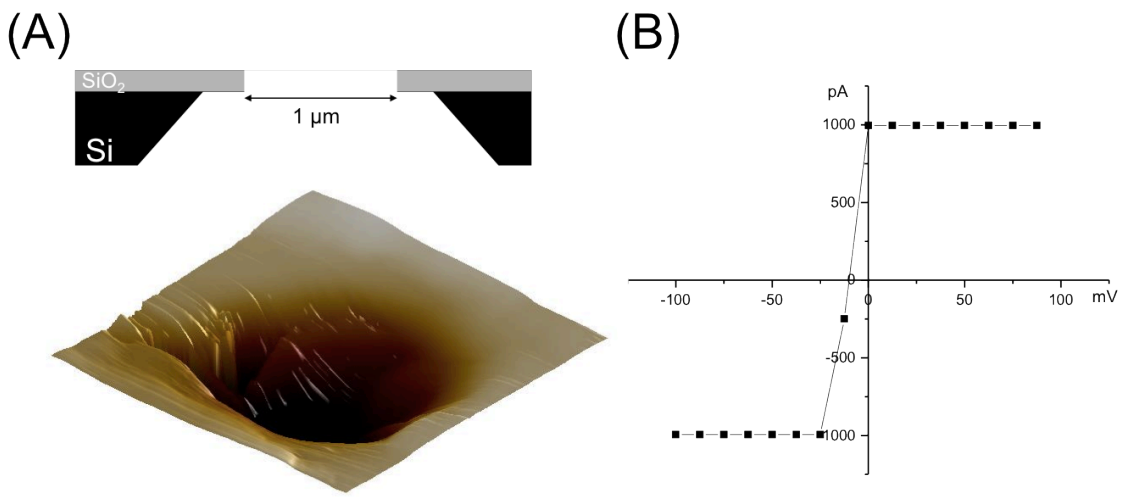

FIGURE 6.2 (A) Side view schematic and 3D AFM height image in contact mode in air of clear open 1 µm pore area. This is the pore prior to plaque deposition. This pore does not have the graphene/Al_2O_3 membrane present. The pore is clear of contamination or blockage prior to membrane deposition. Image size = 1.4 µm; Height color scale = 324 nm (B) IV curve of the open pore shown in (A). The current is immediately saturated as expected for a 1 µm pore. The conductance is at least 14890 nS. The exact conductance could not be determined because the recording system immediately reached its maximum measurable current.

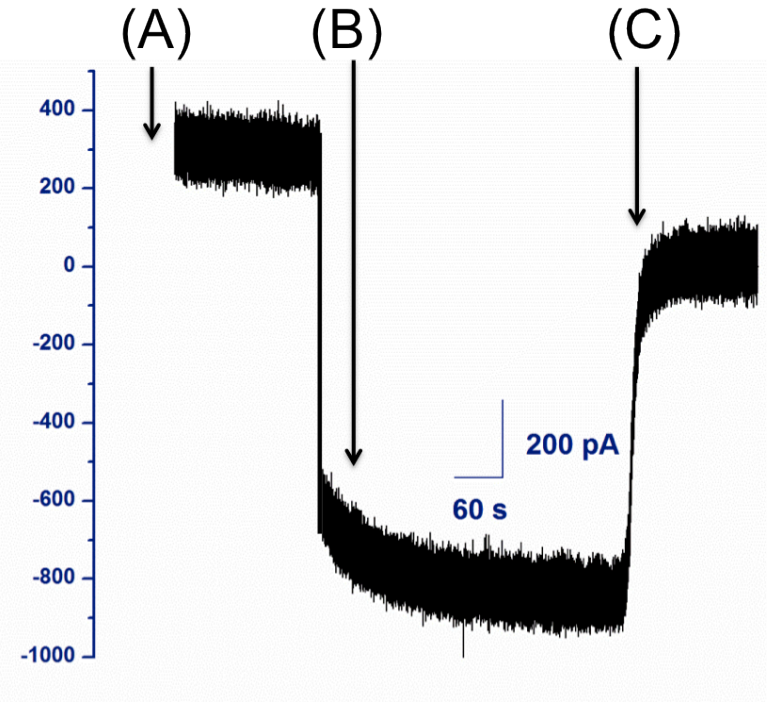

FIGURE 6.3 Electrophysiology recording of the Sf9 membrane with Cx26 deposited over a 1 μm pore. (A) A current of 300 pA was observed under a voltage bias of +50 mV and (B) a current of -800 pA was observed under a voltage bias of -50 mV. (C) Zn^{2+} was added live through an open port in the AFM liquid cell. After several minutes the current jumped to 0 pA (indicated here) and remained stable across ± 50 mV bias potential for several minutes. This inhibition is likely due to Zn^{2+} ions blocking ion channels in the Sf9 membrane, inhibiting conductance activity.

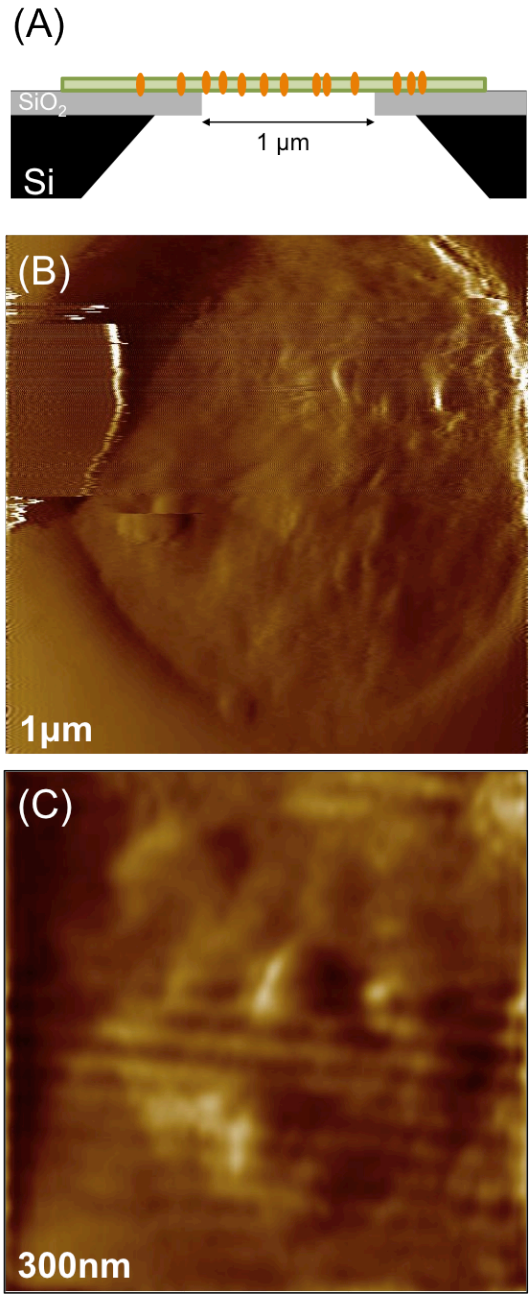

FIGURE 6.4 (A) Side view schematic of channel containing plaque deposited over a pore. This is a representation of the AFM images shown in (B and C). (B) AFM top view image of 1 µm and (C) 300 nm deflection image in contact mode in Tris buffer of Sf9 plaques covering a 1 µm solid state pore. No gaps or holes are observed in either image and plaque was stable enough to continually image for several minutes. Instability observed in top left side of (A) was not observed in the corresponding height image, and is therefore likely due to AFM tip features. Individual Cx26 channels are not resolved.

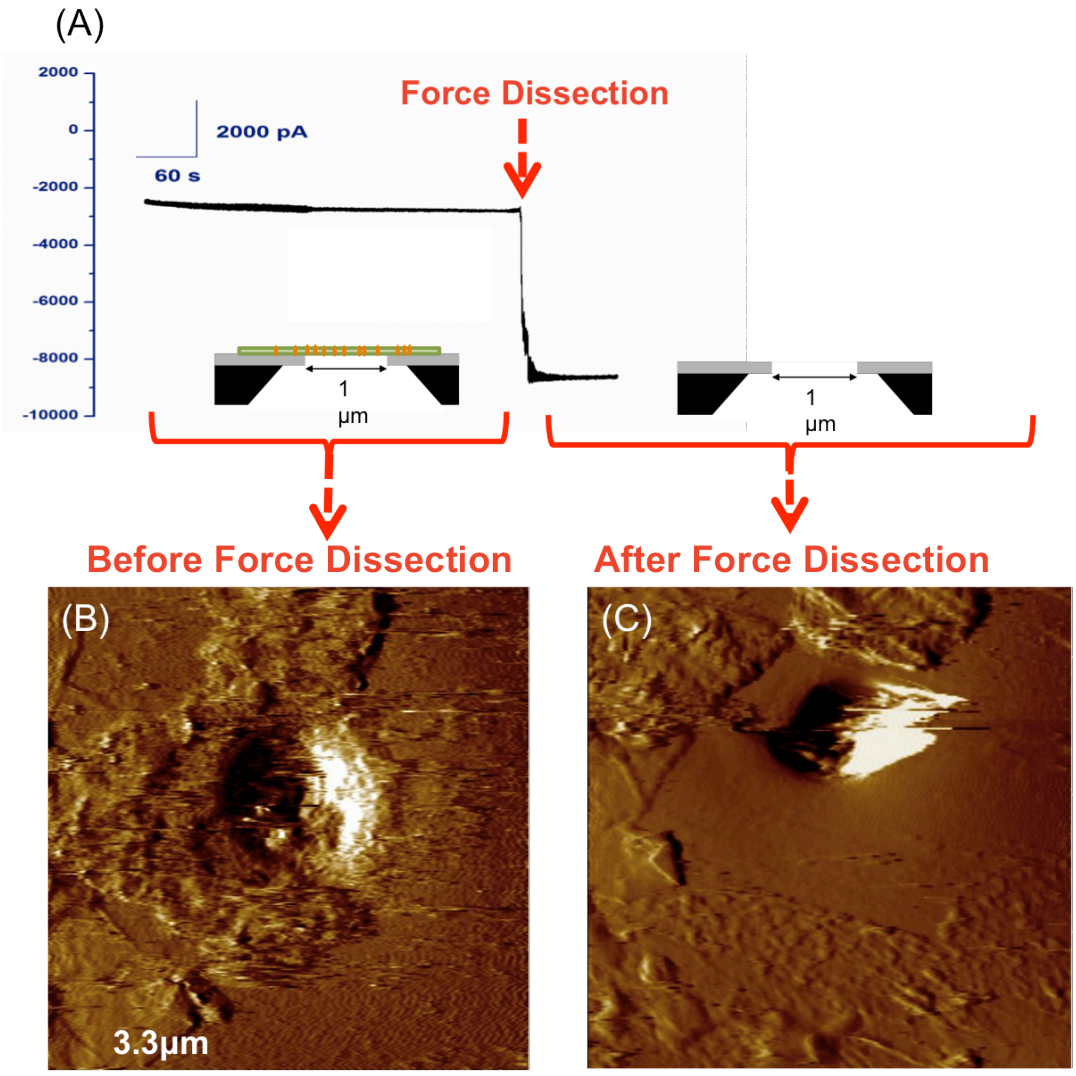

FIGURE 6.5 Electrophysiology real time reading with corresponding AFM deflection images of the pore area before and after the force dissection removal of plaque. (A) Real time current recording under -50 mV voltage bias before force dissection measured -2000 pA. A schematic of the pore covered by a suspended plaque containing hemichannels is shown. An AFM image corresponding to this schematic and section of the current record is shown in (B). In real time, force dissection was then applied to the pore area. During this force dissection the recorded current dropped to -9000 pA. After the force dissection and current drop the AFM image of the pore area in (C) was taken. Image (C) shows the pore area has been cleared of the plaque, as shown in the side view schematic in the drop in current.

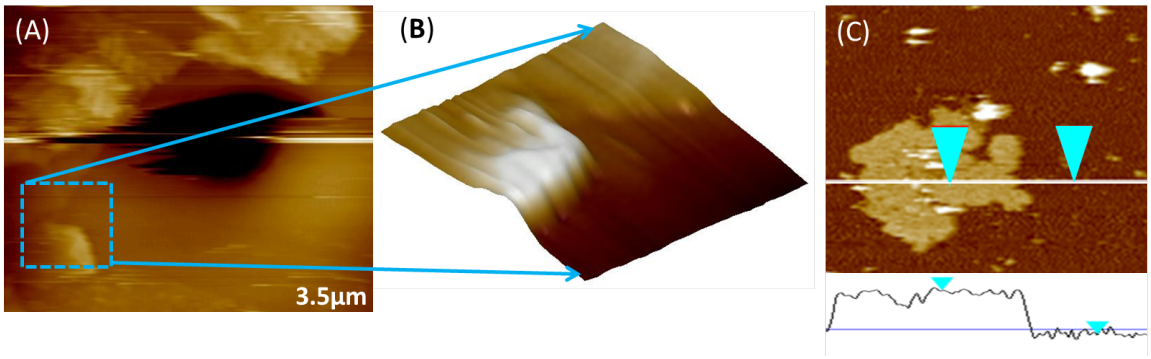

FIGURE 6.6 (A) AFM height image of the pore area after force dissection of the pore area has cleared the pore. The blue box highlights an edge of the plaque that has been cleared. (B) AFM 3D height profile of the blue box highlighted in (A). The height of the single layer edge is 6.3 nm which is comparative to the height of a single Sf9 plaque. Image size is 800 nm x 733 nm. (C) Representative AFM height image of a Sf9 plaque on mica sectioned at the white line and height profile shown below. The height between the two blue arrows, measuring the height difference from the mica surface to the plaque is 6.5 nm. The heights in (B) and (C) are comparative further confirming the cleared away mass was Sf9 plaques.

APPENDIX A

Supplementary material from Chapter 2

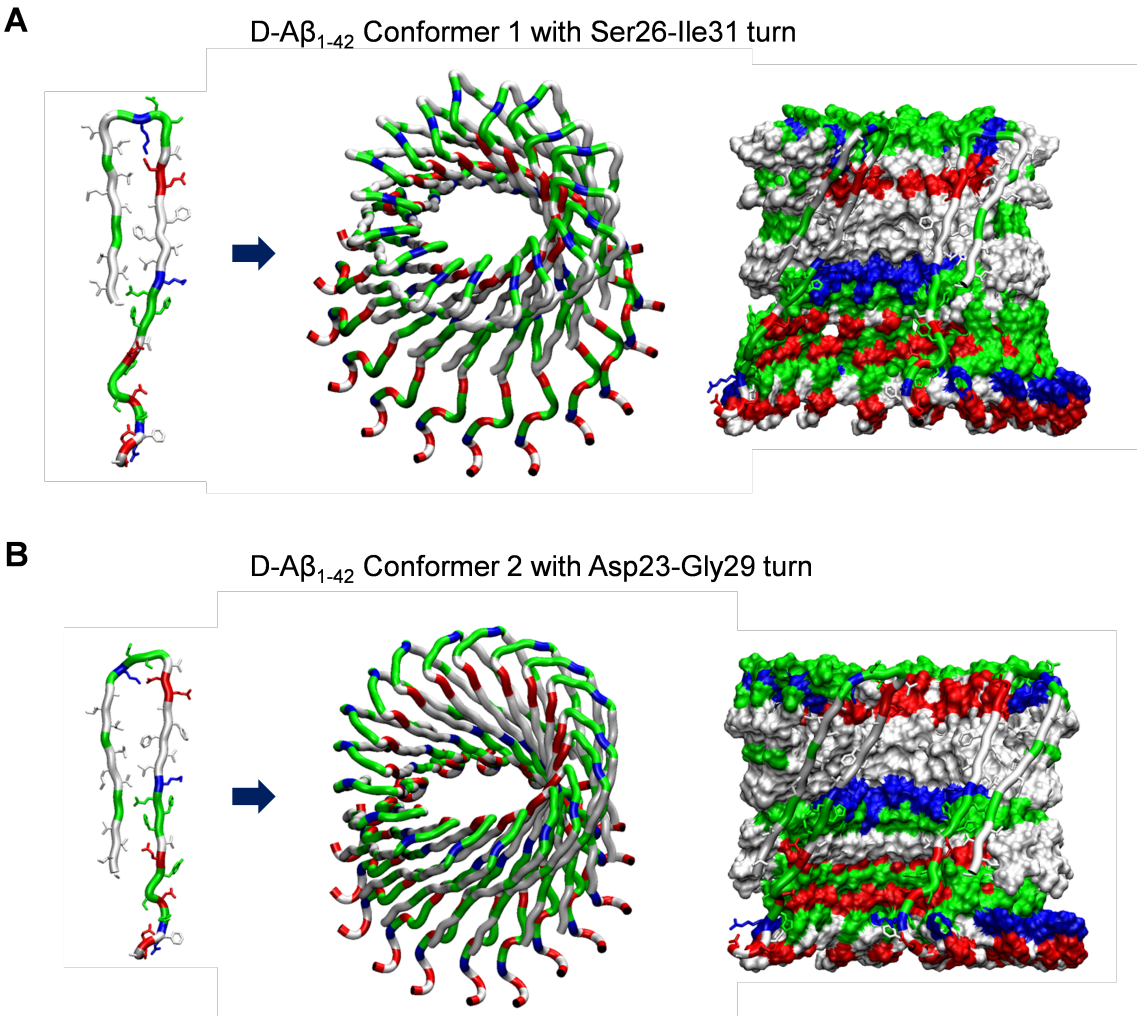

Supplementary Figure A.1 Monomer conformations (left) and the initial barrel structures of MD simulations in ribbon (middle) and surface (right) representations of all D-amino acids Aβ1-42 peptides with different turn at (A) Ser26-Ile31 (conformer 1) and (B) at Asp23-Gly 29 (conformer 2). In the peptide ribbon, hydrophobic residues are shown in white, polar and Gly residues are shown in green, positively charged residues are shown in blue, and negatively charged residues are shown in red. In the surface representation for the barrels, the front part of the barrels in the lateral view has been removed to allow a view of the pore, and the peptide ribbons are embedded on the cross-section.

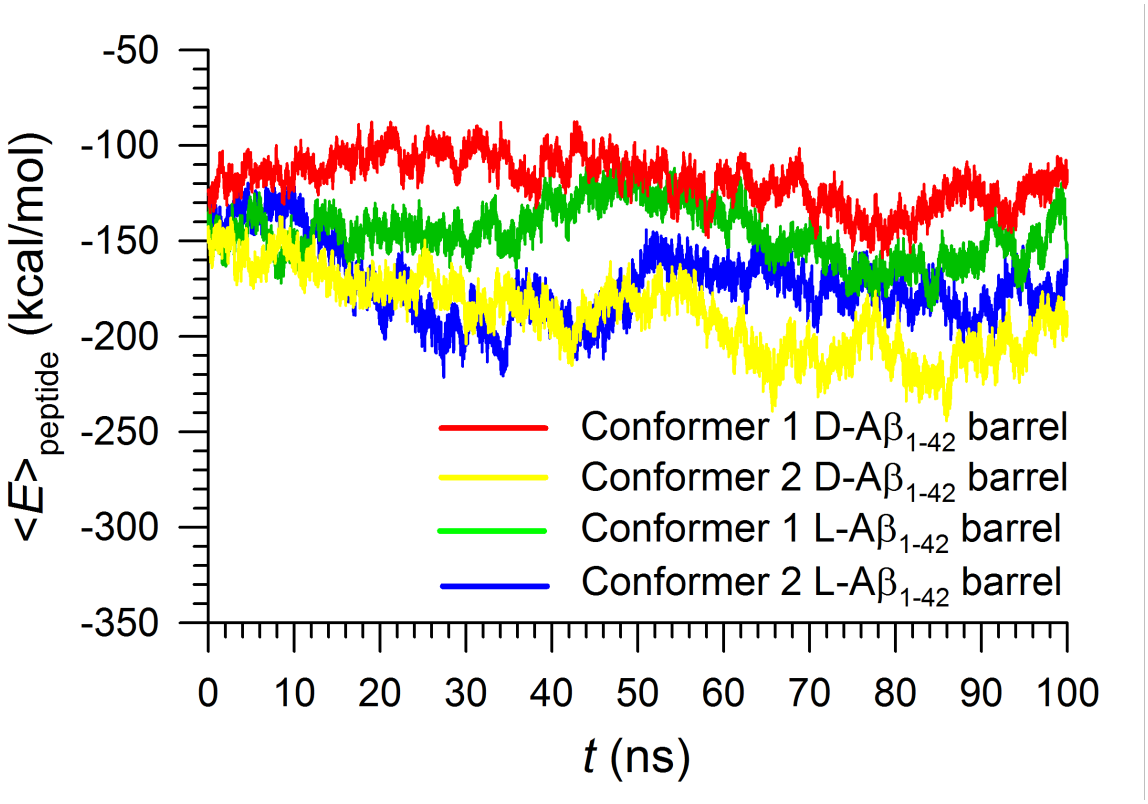

Supplementary Figure A.2 Time series of averaged peptide interaction energy with DOPS and POPE lipids for the conformer 1 (red line) and 2 (yellow line) D-Aβ1-42 barrels, and the conformer 1 (green line) and 2 (blue line) L-Aβ1-42 barrels.

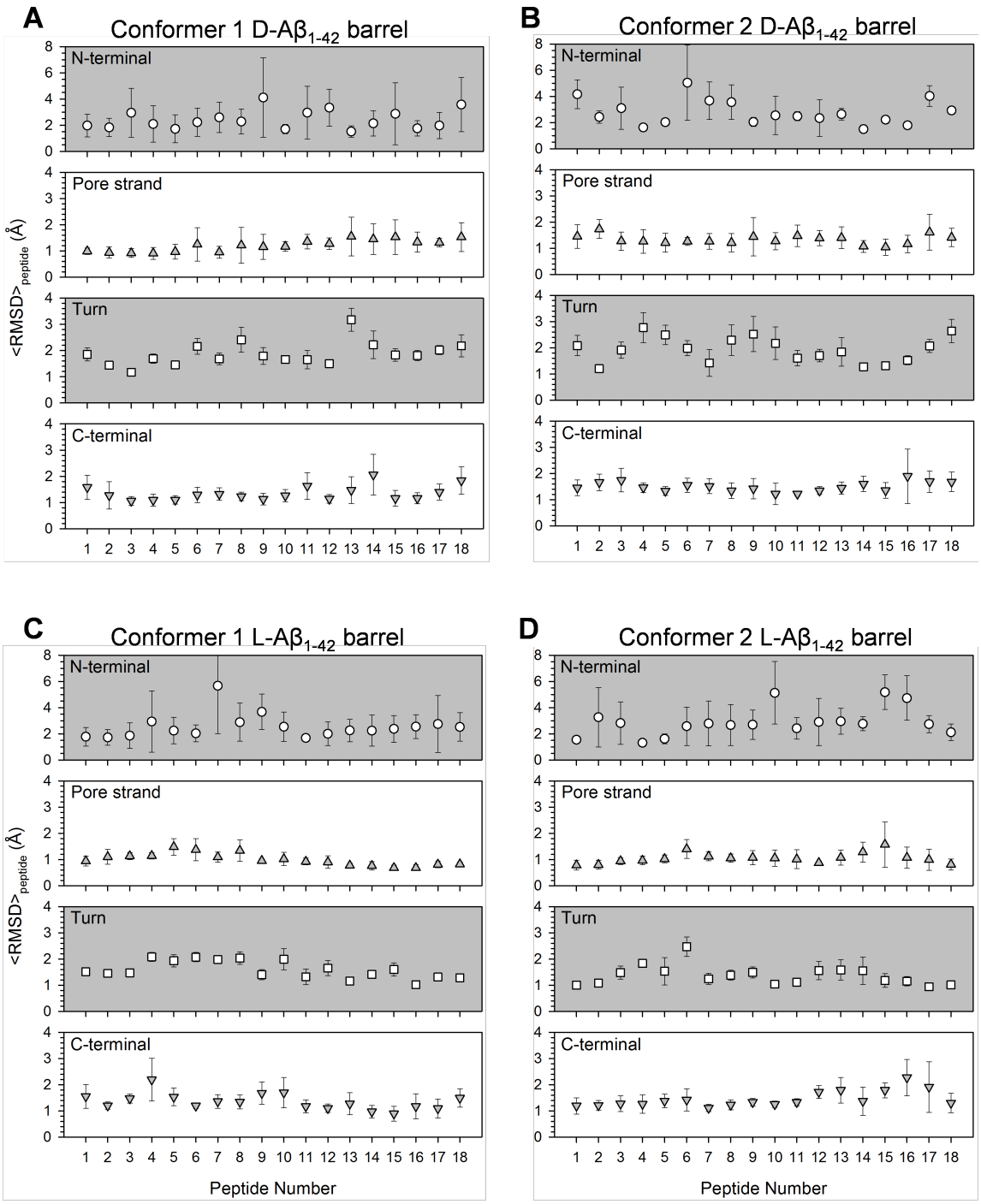

Supplementary Figure A.3 Peptide averaged root-mean-squared deviation, <RMSD>peptide, from the starting point for Cα atoms of the peptides for the (A) conformer 1 and (B) 2 D-Aβ1-42 barrels, and the (C) conformer 1 and (D) 2 L-Aβ1-42 barrels. The RMSD was calculated separately for the peptide by dividing into four domains; the N-terminal, pore stand, turn, and C-terminal portions.

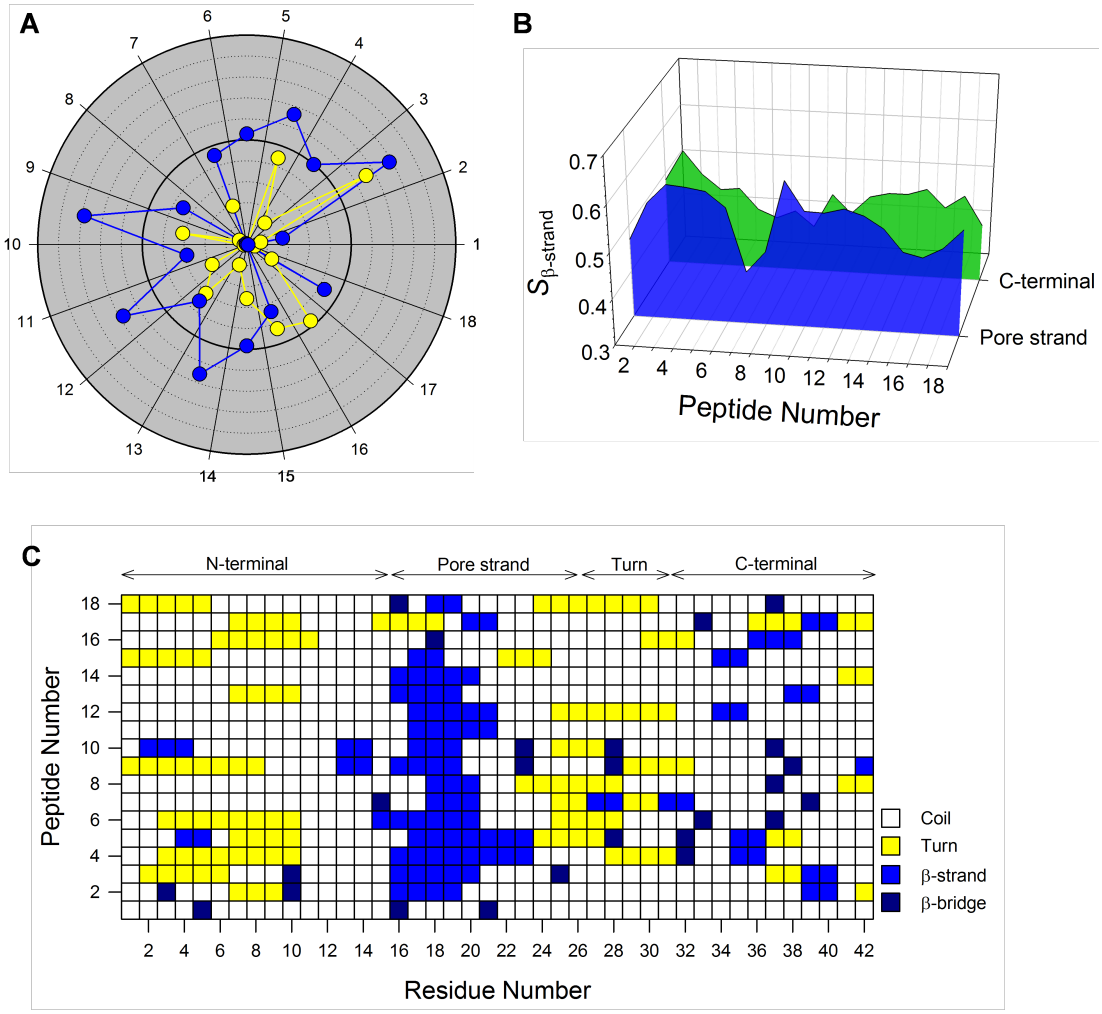

Supplementary Figure A.4 Examples of parameters to define the subunits for the conformer 1 D-A$\beta_{1\text{-}42}$ barrel: (A) Percent of β-sheet content based on the intermolecular backbone hydrogen bonds (H-bonds), (B) the β-strand order parameter using $S_\beta = \frac{1}{N}\sum_{k=1}^{N}\left(\frac{3\cos^2\theta_\alpha - 1}{2}\right)$, where θ_α is the angle between the positional vectors connecting two C_α atoms and N is the total number of vector pairs, and (C) the description of secondary structure by STRIDE (Frishman, D. and Argos, P. 1995. *Proteins* 23:566). The β-sheet content and the β-strand order parameter are calculated for the pore (blue circles & area) and C-terminal (yellow circles & and green area) strands separately as a function of the peptide number. The secondary structure by STRIDE was calculated for the averaged structure.

APPENDIX B

Supplementary material from Chapter 3

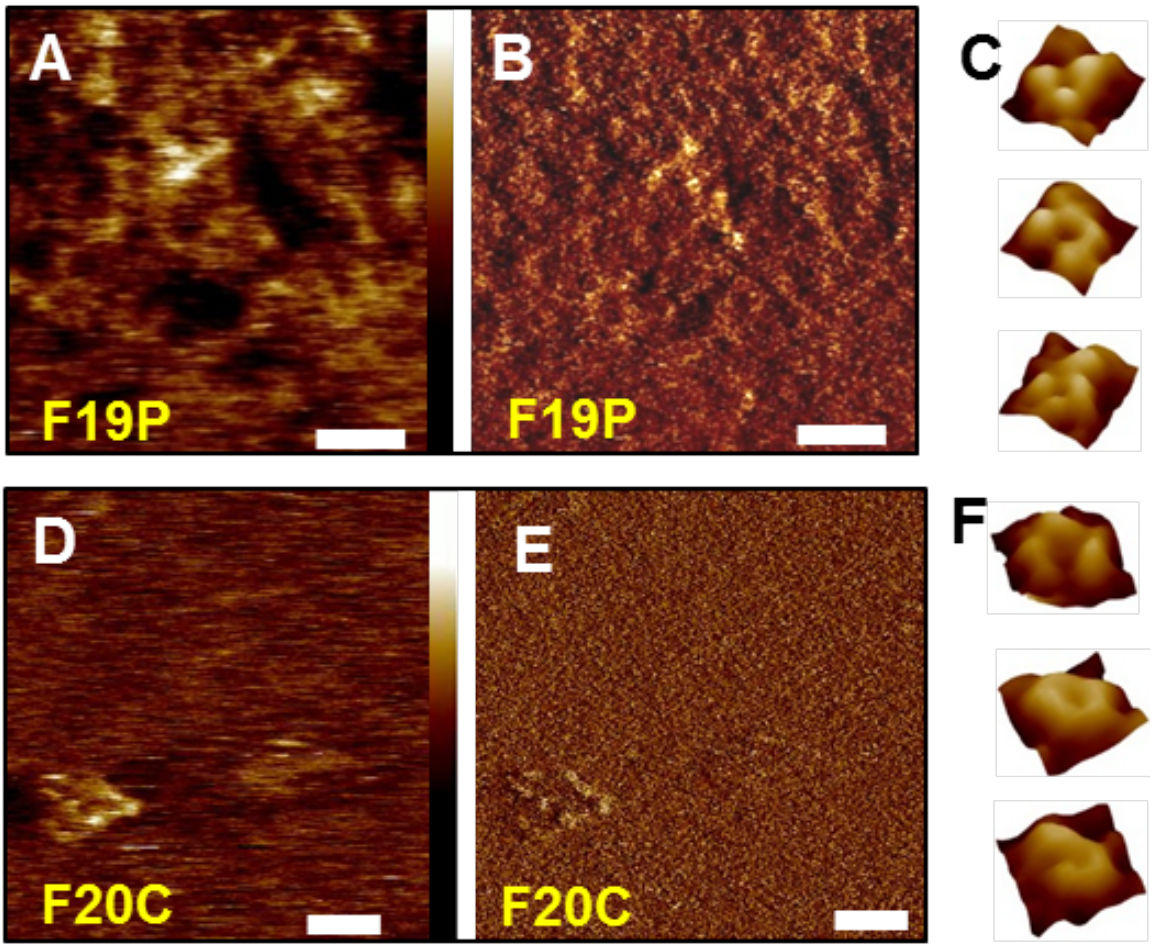

Supplementary Figure B.1 AFM unprocessed (A) height and (B) amplitude images for F19P, and (D) height and (E) amplitude images for F20C mutants incorporated in DOPC bilayers on mica. Height and amplitude images were acquired simultaneously and optimized for the amplitude signal, causing streaking in the height images. (C) F19P and (F) F20C show isolated individual pores from amplitude images for comparison. To only (C) and (F) images, a Gaussian low pass of 4 nm once in the x-direction and once in the y-direction was applied for noise removal. F20C pore structures were seen more clearly after minimal noise filtering of the amplitude image (Fig. 2). The scale bar for is 50 nm for (A), (B), (D), (E) images. The color scale bar for (A) is 7 nm and for (D) is 5 nm. Image sizes in (C) are: 17.46, 13.15, and 14.54 nm. Image sizes in (F) are: 14.00, 11.02, 12.5 nm.

Supplementary Table B.1 The table displays the distribution of multimeric pores measured for wildtype Aβ1-42, F19P-Aβ1-42, and F20C-Aβ1-42. There was not a very large variation in distribution for the F19P mutant or the F20C mutant from the wildtype. The most common pores seen for all peptides were tetramers and pentamers for this sample size. The least common pores seen in this sample set were trimers and hexamers (n=16 for each peptide type).

		Number of Subunits			
		Trimer	Tetramer	Pentamer	Hexamer
Peptide Type	Wildtype Aβ	1	5	6	4
	F19P- Aβ	3	6	5	2
	F20C- Aβ	3	6	6	1

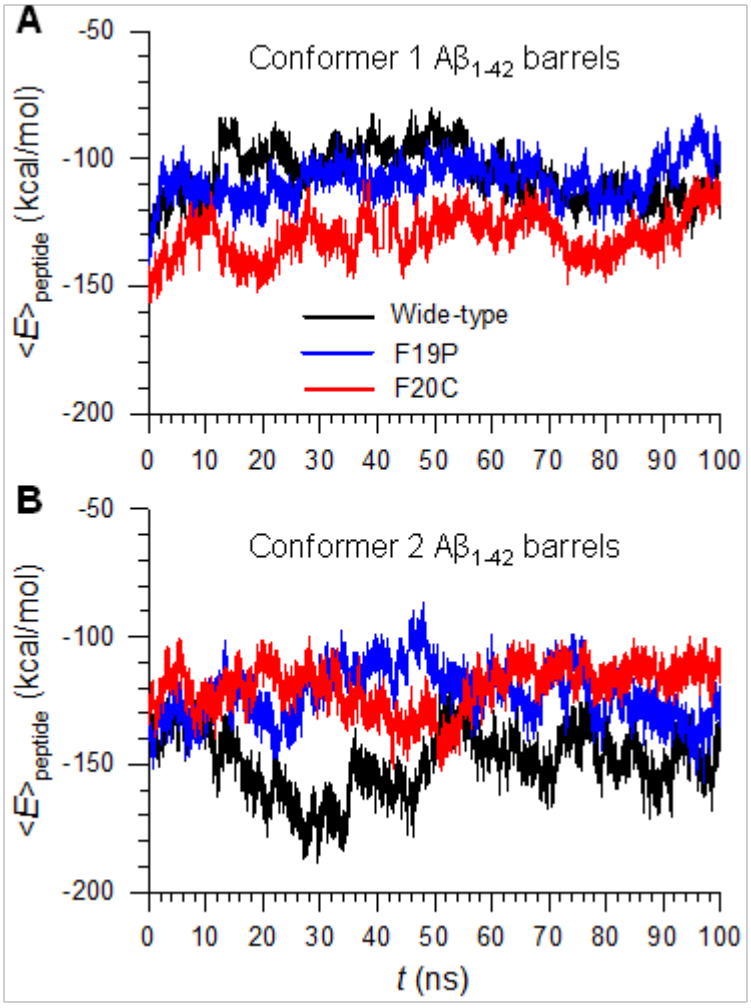

Supplementary Figure B.2 Time series of averaged interaction energy of the U-shaped portion of the peptide with DOPS and POPE lipids for the (A) conformer 1 and (B) 2 Aβ1-42 barrels.